The University of Oklahoma
Graduate College

R-Matrix Theory and Device Modeling

A Dissertation
Submitted to the Graduate Faculty
in partial fullfillment of the requirements for the
degree of
Doctor of Philosophy

By
Thushari Jayasekera
Norman, Oklahoma
2005

Downloaded from SHAREOK. Persistent Handle URL: https://hdl.handle.net/11244/924

UMI Number: 3203284

UMI®

UMI Microform 3203284

Copyright 2006 by ProQuest Information and Learning Company.
All rights reserved. This microform edition is protected against
unauthorized copying under Title 17, United States Code.

ProQuest Information and Learning Company
300 North Zeeb Road
P.O. Box 1346
Ann Arbor, MI 48106-1346

R-Matrix Theory and Device Modeling

A Dissertation Approved for the
Department of Physics and Astronomy

by

Kieran Mullen (Chair)

Michael A. Morrison (Co-chair)

Bruce A. Mason

Matthew B. Johnson

Roger Frech

© Copyright Thushari Jayasekera, 2005
All Rights Reserved.

To My Parents:

Mr. K.G. Jayasekera and Mrs. Wimala Jayasekera

Acknowledgments

Time to cheerfully thank and honor everyone who made me a determined person to come this far!!

First of all I express my sincere gratitude to my thesis advisor, Prof. Kieran Mullen for guiding me throughout this work. His valuable comments, suggestions and insights helped me speed up the work. From his 2000 Spring Graduate Statistical Mechanics class to advanced research problems, I have enjoyed his problem solving skills. I surely benefited from them. I am also grateful to him for giving me the opportunity to present my work at many conferences both inside and outside the US. He made me a very confident person. I certainly respect his patience in all the ups and downs of the research. He has been a very close professor to me during my stay at OU even helping with non-physics issues.

Prof. Michael A. Morrison, my co-advisor has been a great source to us in bringing the aspects of atomic and molecular physics into device physics. I learned lot of analyzing techniques from him which has been a great help in wrapping up this thesis and also in the future research. I will really try to follow his punctuality and organizing skills. He also provided me with great writing tips. Not every student has the opportunity to learn writing from a professional author. I was very lucky.

Dr. Mullen and Dr. Morrison, I really enjoyed working with both of you. Without your long hours reading and correcting my thesis, and mainly guiding through, I surely wouldn't have been able to finish writing the thesis in such a short time.

I wish to thank Prof. Bruce Mason, Prof. M. B. Johnson and Prof. Roger Frech for their comments and suggestions. I acknowledge Prof. M.B. Santos and my colleague,

Niti Goel for allowing me to use their experimental data in this thesis. I thank Prof. Santos for long drives to conferences. I really enjoyed the great excursions. I would like to thank all the professors and my fellow graduate students in the solid state group as well as all the professors and the staff in the department of physics and the international student services (ISS) for helping me in numerous ways. Thanks to my friends Larry Maddox and Darrin Casebeer for giving me the LATEX template and to Madhavie Edirisooriya for proofreading my thesis.

I acknowledge the financial support given to me through out this work by CSPIN, center for semiconductor physics in nanostructures, NSF funded project at the university of Oklahoma.

Many other people have to be honored and thanked who contributed one way or the other. It is hard to mention them all, but I will mention some of them.

I wish to acknowledge all my previous academic institutions, Batepola Maha Vidyalaya (1977-1981), Gothami Primary School (1982), Devi Balika Vidyalaya (1983-1991), Sri Lanka. I especially thank my professors at University of Peradeniya, who recognized my abilities and directed me to higher studies.

It is always hard to be away from home. I fortunately had a big family of friends who helped me make a home here. Many thanks to all my classmates and friends who are too numerous to mention.

Even though I was away from home for a long time, the love and moral support from family was always important. I gratefully acknowledge, my cousin sisters and sister-in-laws, Manori, Nimalka, Disna, Nidukani and my uncle who were all always happy at my success. Especially my brothers Thisara and Chamila who always believed in my abilities and encouraged me to improve them. Lastly, I am very thankful to my parents for their continuous love. Dedicating this thesis to them made me really happy. I know they miss me a lot.

Many Thanks to you All !!

Contents

Acknowledgments **v**

Abstract **xxvi**

Introduction **xxviii**

1 Transport Properties from Scattering Theory **1**

1.1 Landauer Formula for a Two-Terminal Device 2

1.1.1 Temperature Dependence of the Conductance 5

1.1.2 Important Comments on Landauer formula 5

1.2 Landauer-Bütikker Formula 7

1.3 Bend Resistance from the Landauer Bütikker Formula 10

1.4 Conclusion 12

2 Basics of the Variational R-Matrix Theory **13**

2.1 Introduction 13

2.2 R-Matrix Formula 17

2.3 Application of the R-Matrix Theory to Electron Transmission through a Closed Tube 23

2.3.1 Calculation of the R-Matrix Elements 23

2.3.2 Calculation of the Transmission Coefficients 30

2.4 Application of the R-Matrix Theory to Electron Transmission Through an Open Tube 33

2.4.1 Calculation of the R-matrix Elements 34
2.4.2 Calculation of the Transmission Coefficients 37
2.5 Convergence Studies of the Variational R-Matrix Theory 39
2.6 Conclusion 44

3 2-Dimensional R Matrix Formula 45
3.1 Introduction 45
3.2 R-Matrix Formula for a T-Junction Device 47
3.2.1 Lead Solution 48
3.2.2 R-Matrix Formula and the Interior Region Problem 51
3.2.3 Implementation of the Device R-Matrix Formula for a T Junction Device 55
3.3 Results of the Scattering of Electrons in the T-junction Device 60
3.4 R-Matrix Formula for a Plus-Junction 64
3.5 Conclusion 66

4 R-Matrix Connection Formula 68
4.1 Introduction 68
4.2 One-Dimensional R-Matrix Connection Formula 70
4.3 2-Dimensional R-Matrix Connection Formula: Application to the Electron Scattering by a Diamond-Shaped Device 73
4.4 Scattering of Electrons in a 4-Terminal Wedge Geometry 81
4.5 Summary 85
4.6 Conclusions 85

5 Evaporative Cooling in Semiconductor Devices 87
5.1 Introduction 87
5.2 Theory: Ideal Model 89
5.3 Applications to Real Devices 97
5.3.1 T-junction as a Cooling Device 98

5.3.2 Plus Junction as a Cooling Device 104
5.4 Considerations for experiment 106
5.5 Conclusions 107

6 Magneto-Transport Properties in Semiconductor Devices 108
6.1 Magneto-Transport Properties of Electrons in Two-Dimensional Devices 111
6.2 Two-Dimensional R-Matrix Formula with an Applied Perpendicular Magnetic Field 114
6.2.1 Lead Eigenfunctions 116
6.2.2 Interior Region Solution 120
6.2.3 R-Matrix Formulation 123
6.3 Applications: 4-Terminal Square Junction. 126
6.3.1 Transmission Coefficients 126
6.3.2 Calculating the Magneto-Transport Properties 130
6.4 Applications: 4-Terminal Wedge Junction Device 132
6.5 Temperature Dependence of the Bend Resistance 135
6.6 Conclusion 136

7 Conclusion 138

A Background of R-Matrix Theory 141
A.1 R-Matrix Theory in Device Physics 141
A.2 R-Matrix Theory in Atomic and Molecular Physics 142
A.3 R-Matrix Theory in Device Physics 143
A.4 Choice of Basis for Variational R-Matrix Calculations 145

B Dimensionless Units to Physical Quantities 147
B.1 Lengths and Energies 147
B.2 Strength of the Magnetic Field 150

C Bloch Eigenfunctions in a Wedge Geometry 152

D R-Matrix Connection Formula for a 4-Terminal Wedge Junction Device **156**

Bibliography **161**

List of Figures

1.1 Two reservoirs are connected by a conducting wire (left figure) which is represented by a scatterer for the electron's path (right figure). The edges of the conductance band in left and right sides are denoted by U_L and U_R. The chemical potentials of both sides are equal because the applied voltage, $V = 0$. The net current flow through the reservoirs is zero. 2

1.2 A positive bias voltage is applied across the one dimensional scatterer. There is a gap created between the chemical potentials of both sides such that $\mu_L - \mu_R = eV$. 3

1.3 A schematic diagram of a 4-terminal device used in the bend resistance experiment. A current I_{14} is injected from the lead 4 to 1 and the voltage created between the leads 2 and 3, V_{23}, is measured. There is a magnetic field perpendicular to the device. The bend resistance, $R_B = V_{23}/I_{14}$ is measured as a function of the strength of the magnetic field [10]. 10

2.1 A schematic diagram of a two-dimensional device for the scattering calculation. The surfaces $S_1, S_2, \cdots, S_N$ separate the interior region A from the leads. We seek the transmission coefficients of outgoing electrons in the leads when one incoming subband is occupied. 14

2.2 A schematic diagram of a closed tube for the R-matrix theory calculation. We artificially divide the system into two parts defining the interior region as A. Electrons are injected from $x > L$. Supposing that electrons undergo scattering in region A, we seek the transmission coefficient in the region, $x > 0$. 24

2.3 The exact R-matrix for the closed tube problem, $R^{\text{exact}}(E, L, L) = \frac{|\Psi_E(L)\rangle}{\frac{d}{dx}|\Psi_E(L)\rangle}$ as a function of the scattering energy. The R-matrix diverges at R-matrix poles. R-matrix poles are the scattering energies which equal to one of the Bloch eigenenergies of the interior region A. 27

2.4 A diagram of exact WE basis functions (upper) and the variational basis functions (lower) in the interior region of the closed tube. Note that the WE wave functions have a particular boundary conditions while the variational basis functions have different values and different derivatives on the soft boundary. 28

2.5 Graph of the R matrix as a function of the number of basis functions used in the calculation of electron scattering in a closed tube. We have only one soft boundary so there is only one R matrix element. In this problem R- matrix element relates to the scattering wave function as, $R(E, L, L) = \frac{\Psi}{\frac{d}{dx}\Psi}$. The value is evaluated at energy $E = 100 \times \frac{\hbar^2}{m^* a^2}$. Solid dots are the result obtained by variational basis functions and the open dots are the result obtained by using the Wigner-Eisenbud (logarithmic derivative) basis functions. The straight line is the exact result. This typical case shows that the variational basis functions achieves faster convergence when compared to the Wigner-Eisenbud basis functions. 31

2.6 Graph of the reflection amplitude of the electron as a function of the number of basis functions used in the calculation of scattering in a closed tube as evaluated at energy $E = 100 \times \frac{\hbar^2}{m^* a^2}$. Solid dots are the result obtained by variational basis and open dots are the result obtained by using the Wigner-Eisenbud basis. The straight line is the exact result (reflection amplitude = -1). This result shows that the variational basis functions achieves faster convergence when compared to the Wigner-Eisenbud basis functions confirming the conclusion made in section (2.3.1). 32

2.7 A schematic diagram of an open tube for the R-matrix theory calculation. We artificially divide the tube into three regions, regions I, II, and III. Electrons are injected from region I. Supposing that electrons undergo scattering in region II, we seek the transmission coefficient in regions I and III. The answer is known for this problem: The transmission coefficient is 0 in region I and the transmission coefficient is 1 in region III. We look at the convergence of this result as a function of number of basis functions used in calculating the R-matrix elements, in order to study the convergence. 34

2.8 Graph of the R-matrix, $R_E(+,+)$ at energy, $E = 100 \times \frac{\hbar^2}{m^* a^2}$ as a function of the number of basis functions used in the calculation. Solid dots are the result obtained by variational basis functions, open dots are the result obtained by using the logarithmic derivative boundary conditions. This graph shows that the variational basis functions give a faster convergence in the R-matrix calculation as we concluded in the section (2.3). 36

2.9 A graph of transmission amplitude of the electron as a function of the number of basis functions used in the calculation in the open tube problem as evaluated at the energy $E = 100 \times \frac{\hbar^2}{m^* a^2}$. Solid dots are the result obtained by variational basis functions and the open dots are the result obtained by WE basis functions. The straight line is the exact result. 38

2.10 The value of the R matrix, $R_E(+,+)$ as a function of the number of eigenfunctions used in the summations. The straight line is the exact result. Solid dots are the result obtained using the variational basis functions and the open dots are the result obtained using the WE functions. In this calculation, the Hilbert space consists of only 12 basis functions and the electron scattering energy is 100 in dimensionless units. 40

2.11 The value of the R matrix, $R_E(+,+)$ as a function of the number of basis functions used in the summations. The straight line is the exact result. Solid dots are the result obtained using the variational basis functions and the open dots are the result obtained using the WE functions. In this calculation, the Hilbert space consists of only **10** basis functions and the electron scattering energy is 100 in dimensionless units. The features are the same as the features we observed in the graph (fig.2.10) confirming that this feature is independent of the number of basis functions. 42

2.12 Variation of the relative error of $R_E(+,+)$ as a function of scattering energy for both the variational and the Wigner-Eisenbud calculation. Solid dots are for the variational calculation and the open dots are for the WE calculation. The dotted straight lines are the Bloch eigen energies. 43

3.1 A schematic diagram of a T-junction device for the two-dimensional R-matrix formula calculation. Electrons are injected from the lead 1. We seek the transmission amplitudes in lead 1 (reflection), lead 2 and the lead 3. . 47

3.2 Transmission coefficients of electrons traveling in the T junction device. The electrons are injected from the lead 1. The plotted quantities are the lead to lead transmission coefficient. The dotted lines are the threshold energies of the input lead. For this device $w_1 = w_2 = w_3 = 1$. 60

3.3 A plot of the probability density of electrons traveling in a T-junction device. The energy of the scattering electron, $E = 26$ in the dimensionless units. . 61

3.4 Graph of the lead to lead transmission coefficient T_{31}, that is the transmission coefficient of electron to the lead 3 when the electrons are injected from the lead 1. The upper plot is the result obtained using the Wigner-Eisenbud (WE) basis functions and the lower plot is the result obtained using the variational basis functions. In the WE calculation the results are not converged even with 100 (10×10) basis functions. In this variational calculation, there is no graphical difference between the 36 (6×6) calculation and 100 (10×10) calculation which means that the result is converged with 36 (6×6) basis functions. The dotted lines are the threshold energies for the incoming lead. 62

3.5 The forward lead transmission coefficient calculated using the Wigner Eisenbud (open dots) and the variational (solid dots) basis functions. In both the calculations, we used 100 (10×10) basis functions. 63

3.6 A schematic diagram for the plus junction device geometry. We calculate the transmission coefficients of electrons traveling in this device. 64

3.7 Lead to lead transmission coefficients of electrons traveling in the plus junction device (fig.3.6). Electrons are injected from the lead 1. For this device $w_1 = w_2 = w_3 = w_4 = 1.0$. 65

3.8 State to state transmission coefficient of electrons traveling in the T-junction device. Electrons are injected from $n_1 = 1$ and transmit to $n_3 = 1$. The solid straight lines are the Bloch eigenenergies and the dotted lines are the threshold energies of the lead 1. The Wigner-Eisenbud result does not converge at every Bloch eigenenergy as in the one-dimensional case. . . . 66

4.1 A schematic diagram of an open tube with two interior regions. Electrons are injected from the region L, undergo scattering in the regions I and II. We seek the transmission amplitude in the region R which we solve using the R-matrix connection formula. 70

4.2 A schematic diagram of a device with a diamond geometry. We consider this device in 4 regions, L, I, II, and R, which are separated by the soft boundaries at $x = x_A$, $x = x_D$, and $x = x_C$. Electrons are injected from the left lead, undergo scattering in the regions I and II, and scatter into the regions L and R. We recognize the diamond shaped interior region as a combination of two wedges as shown in the inset. We calculate the transmission coefficients in the two outgoing leads L and R using the R-matrix connection formula by connecting the Bloch eigenfunctions of a wedge, but not using the eigenfunctions of a diamond shaped geometry. 74

4.3 Transmission and reflection coefficients of the electrons injected to a double-wedge geometry shown in the figure (4.2). The upper plot is the transmission coefficients (to the lead R) and the lower plot is the reflection coefficients (to the lead L) as a function of the energy of the electron. In this calculation the wedge is defined by $w_A = 1$ (all the lengths of the system is measured in terms of the width w_A), $w_D = 2.5$. The opening angle of the wedge (inset of the figure 4.2), $2\theta_0 = \pi/3$. The electron is injected in the first subband and the transmission coefficients are summed over all the output subbands, so that this is the state to lead transmission coefficients. We have marked the anti-resonance ($\epsilon = 6$) and the resonance state ($\epsilon = 6.45$). The probability densities at the resonance and the anti-resonance are shown in the figure (4.4). 79

4.4 The probability density of an electron traveling in a device with a diamond shaped geometry at resonances and anti-resonances. The upper figure is the $|\Psi|^2$ at energy, $E = 6$ (anti-resonance: electron has a minimum amplitude inside the scattering region.) and the lower figure is the $|\Psi|^2$ at $E = 6.45$ (resonance: electron has a maximum amplitude inside the scattering region). 80

4.5 A schematic diagram of a 4-terminal wedge junction device. Electrons are injected from the lead 1 and scatter in the interior region and scatter out in to leads 1, 2, 3, and 4. We seek for the transmission coefficients of the electrons to those 4 leads. We calculate the transmission coefficients using the R-matrix connection formula since the interior scattering region has a complicated structure. 82

4.6 Transmission coefficients of the electrons in a 4-terminal wedge junction. The stars are the transmission coefficient to the forward lead, open dots are to the left lead and the solid dots are to the right going lead. The device used here is symmetric. The specifics of each wedge are such that $\theta_0 = \pi/4$, $w_{A1} = 1.0$, and $w_{D1} = 1.05$, in which the 4-terminal wedge device is turned onto a 4-terminal square junction device. This results recovers the result we obtained in the section 3.4. 83

4.7 Transmission coefficients of electrons traveling in a 4-terminal wedge junction device. We use a symmetric wedge that all the four sides are similar. The opening angle of the wedge is kept constant that $2\theta_0 = 43^0$ and $w_{A1} = 1.0$. The transmission coefficients are plotted for devices with different values of w_{D1} as shown in the inset of each plot. 84

5.1 A schematic diagram of a T shaped assemble used in the Hilsch vortex tube. High pressure air is injected from the side arm and separated into cold and hot parts using the vortex operated in the middle of the T assembly. . . . 88

5.2 A schematic diagram of a T-shaped assemble of a quantum wire configuration. Electrons are injected from the source and they scatter into all the output leads. Since the equilibrium electron distribution is disturbed by scattering, they re-thermalize in the output leads. In the text, we show how to calculate the new equilibrium temperature for some systems with particular geometries and show that we can find some geometries and initial chemical potentials for which the final temperature is less than the initial temperature which means the cooling of the system. 90

5.3 A quantum wire T junction device is divided into regions to explain the electron cooling behavior. Electrons are injected from the input region, and undergo scattering in the scattering region. In the ballistic region, electrons are not in equilibrium, and the electron population is determined by the product of incoming-electron distribution and the transmission coefficient. Electrons re-thermalize and come to an equilibrium in the adiabatic region; however, there is no relaxation with the phonons. In the text we show how to calculate this new equilibrium temperature and the new chemical potential. 91

5.4 Upper plot is a graph of cooling parameter, $\eta = T_f/T_i$ as a function of the chemical potential μ_i. The initial temperature $T_i = 0.25$ for this calculation. This variation of η shows that, for some chemical potentials, $\eta \leq 1$, which means we get cooling. Also there is a significant minimum in the cooling parameter when $\mu_i = 3$; the reason for this behavior is explained in the text. The lower plot is the variation of the cooling parameter a function of the initial temperature, $T_i = k\tilde{T}_i/\mathcal{E}_0^i$. The initial chemical potential is kept at the edge of the second subband, which is the optimum value from the upper plot . This shows a maximum of 30% cooling. 95

5.5 The upper plot is the transmission coefficients of electrons to the output lead in a T-junction device with $w_i = w_s = w_o = 1$. The different curves are for different subband index of the incoming electron. The x axis is the energy of the incoming electron which is measured in terms of $\mathcal{E}_0^i = \hbar^2\pi^2/2m^*w_i^2$ and is measured from $\mathcal{E}_0^i$. We calculate the cooling parameter using these transmission coefficients. Since there are some higher subband electrons lost from the input distribution, we expect $\eta < 1$. This graph shows that the cooling parameter $\eta > 1$ which means $T_o > T_i$. Even though we lose higher subband electrons from the system, it does not achieve cooling. 99

5.6 The cooling parameter η as a function of the initial temperature T_i when the initial chemical potential $\mu_i = 0$ for different w_i values. This graph shows that the cooling parameter η is always larger than 1 for some w_s values and $\eta < 1$ for some w_s values. This says that by changing the transmission coefficients we can change the cooling parameter. 100

5.7 The state to state transmission coefficients of electrons to the output lead in a T-junction device with $w_i = w_o = 1.0$ and $w_s = 0.4$. The data in table (5.1) shows that this transmission coefficients gives 0.05% of cooling. . . 102

5.8 The cooling parameter as a function of the initial temperature for the T-junction device with $w_i = w_o = 1.0$ and $w_s = 0.4$. We calculate the cooling parameter using the transmission coefficients shown in the figure (5.7) at different initial chemical potentials, $\mu_i = 0.0, 3.0, 6.0$. The results show that we achieve the best cooling when $\mu_i = 0$. 103

5.9 Upper plot is the transmission coefficients of electrons to the output lead in a plus-junction device with $w_2 = 0.4$. The different curves are for different subband index of the incoming electron. The x axis is the energy of the incoming electron which is measured in terms of $\mathcal{E}_0^1 = \hbar^2\pi^2/2m^*w_1^2$ and is measured from $\mathcal{E}_0^1$. We calculate the cooling parameter using these transmission coefficients and the result is shown in the lower plot. It shows $\eta \sim 0.85$ which means more than 15% of cooling. 104

5.10 This graph shows a summary of the cooling calculations we have done in this chapter. The solid line is the cooling parameter for the T-junction device with $w_i = w_s = w_o = 1.0$, open dots are the cooling parameter for the T-junction device with $w_i = w_o = 1.0$ and $w_s = 0.4$. The solid dots are for the plus junction device with $w_1 = w_3 = 1.0$ and $w_2 = w_4 = 0.4$. All the calculations are done when the initial chemical potential $\mu_i = 0$. 105

6.1 The unit of quantum confinement energy, $\hbar^2\pi^2/2m^*w^2$ as a function of the well width, w. The solid dots are for InSb and the empty dots are for GaAs. The straight line is the room temperature thermal energy. 109

6.2 An image of a typical 4-terminal device [32]. The interior region of this device is square-shaped and all the outgoing leads are rectangular. A sketch of this figure with the coordinates used for the calculation is shown in the figure (3.6). In the text we explain how to calculate the transmission coefficients of electrons in such a device. 112

6.3 An image of the 4-terminal device designed on InSb quantum well used for the bend resistance experiment [10]. In the bend resistance experiment, a current I_{14} is injected from lead 4 to lead 1 and the voltage created between the leads 2 and 3, V_{23} is measured. The bend resistance, $R_B = V_{23}/I_{14}$ is measured. The experiment is done in the presence of a perpendicular magnetic field. Goel et. al has reported a negative bend resistance as shown in the figure (6.7). This is a signature of the ballistic transport. In the text we explain how to calculate the bend resistance of such a device. 113

6.4 The real part of the transverse eigenfunction in a lead in the presence of a perpendicular magnetic field $\mathcal{B} = 15$. The width of the lead $w_p = 1$. . . . 118

6.5 Transmission Coefficients for the electron injected to the 4-terminal square junction device shown in the (6.2). Electrons are injected from the lead 1. We have calculated the transmission coefficients for 4 different cases, $\mathcal{B} = 0$, $\mathcal{B} = 6$, $\mathcal{B} = -6$ and $\mathcal{B} = 12$. When there is no magnetic field, since the device is symmetric both T_{21} and T_{41} are equal and T_{31} is always larger than the sidearm transmissions. This zero field result correctly recovers the result we obtained with zero-field RMT. This figure also shows that when you increase the magnetic field, the transmission coefficient to the lead 2 increases and at some energies it is even higher than the forward transmission. Also the two plots relevant to $\mathcal{B} = 6$ and $\mathcal{B} = -6$ show that by changing the direction of the magnetic field, the transmission coefficients to the left and right leads interchange as one would expect. 128

6.6 The probability density of a positively charged particle injected to the 4-terminal junction. The left figure shows the probability density of the particle when there is no magnetic field and the figure to the right is the probability density when the applied perpendicular magnetic field $\mathcal{B} = w_0^2/l_B^2 = 20$. Both the probabilities are calculated when the scattering energy, $E = 25$ in the dimensionless units as described in the text. Note that the sidearms have similar probabilities for the left figure, but not for the right figure. . 129

6.7 The upper plot is the bend resistance, R_B of a 4-terminal square junction device as calculated using the magnetic-field RMT and the LB formula. The lower plot is the experimental observation for R_B as a function of the magnetic field for a device with a geometry shown in the figure (6.3). Note that two geometries are different. In the theory, we have calculated R_B at different Fermi energies, which means that we have calculated the R_B at different sizes of the devices (see appendix B). The results have a qualitative agreement to conclude that the InSb device has a coherent electron behavior. 131

6.8 Transmission Coefficients for the electrons injected to the 4-terminal wedge junction device shown in the figure (6.3). The device is specified by $w_A = 1.0$, $w_D = 1.5$, and $2\theta_0 = 43^0$ according to the figure (4.5). Electrons are injected from the lead 1. We have calculated the transmission coefficients for 4 different cases, $\mathcal{B} = 0$, $\mathcal{B} = 6$, $\mathcal{B} = -6$ and $\mathcal{B} = 8$. Since the device is symmetric both T_{21} and T_{41} are equal and T_{31} is always larger than the sidearm transmissions when there is no magnetic field. This zero field result correctly recovers the result we obtained with zero-field RMT. This figure also shows that when you increase the magnetic field, the transmission coefficient to the right lead increases and at some energies it is even higher that the forward transmission. Also the two plots relevant to $\mathcal{B} = 6$ and $\mathcal{B} = -6$ show that by changing the direction of the magnetic field, the transmission coefficients to the left and right leads interchange as one would expect. 134

6.9 Bend resistance of a four-terminal wedge junction device (fig.4.5) as a function of the magnetic field, B. We have calculated the bend resistance at different values of Fermi energies which is for different values of device sizes (w_A). For a conversion of the Fermi energies to the device sizes at a given carrier concentration, see appendix (B). 135

6.10 Bend resistance, R_B as a function of the magnetic field for the four terminal square junction device when the dimensionless Fermi energy equlas to 40. The different curves are for different temperature as shown in the inset. This graph shows that the bend resistance decreases as you decrease the temperature. However, that behavior breaks down after $T = 100K$. We discuss this in the text (see section 6.6). 136

C.1 A schematic diagram of a wedge geometry. In this appendix, we discuss how to calculate the Bloch eigenfunctions in the wedge geometry which is used in the chapters (4) and (6). The mesh in the figure shows a new coordinate system $(x, t = y/x)$. In the text we explain how to use both the (x, y) and (x, t) coordinate systems to calculate the Bloch eigenfunctions in this geometry. 152

List of Tables

2.1 The eigen-energies E_j of the interior scattering region for different quantum number j for the open tube problem. 41

5.1 The cooling parameter of the T-junction with different width of the sidearm. We have also tabulated the input chemical potential, output chemical potential and output temperature at the maximum cooling parameter. . . . 101

B.1 The dimensionless Fermi energy is converted into the size of the device. In fact, the values at different points in the x axis of the transmission coefficients graphs (fig.6.5 and fig. 6.8) is converted into the relevant device size. We considered a sample with a electron concentration $n = 1.90 \times 10^{11}\text{cm}^{-2}$. 150

Abstract

Novel experimental techniques allow us to fabricate very small semiconductor devices such that the electron mean free path is larger than the size of the device. The macroscopic properties of these quantum mechanical devices can be calculated using the Landauer formula, which requires as input the transmission coefficients of electrons in the device. We mainly focus on InSb-based devices in which the effective mass is very small ($m^* = 0.0139\, m_0$, where m_0 is the free electron mass). Since the gaps between electron subband levels in such devices are large that these devices are more likely to behave in a fully quantum mechanical fashion. Thus it is important to calculate the transmission coefficients of electrons in such a device quantum mechanically.

To calculate the transmission coefficients, we use R-matrix theory (RMT), a technique that was first introduced in nuclear physics, and later applied in atomic and molecular physics, and that has recently been shown to be a useful tool for calculating the transport properties of solid-state devices. We have improved upon the existing implementations of RMT in device physics by introducing a procedure that dramatically speeds the convergence. This approach is called variational R-matrix theory. Moreover, we have extended the R-matrix formalism to scattering systems with very complicated device geometries. The new formalism, which we call "the R matrix connection formula" can be used to calculate the transport properties of practical solid-state devices. Our variational device R-matrix theory is a very accurate, efficient way to calculate transmission coefficients of electrons in such a device. We discuss the applications of RMT to modeling of new experimental devices and explain existing experimental observations.

To illustrate the usefulness of this theory, we propose a new device that uses the evaporative emission of electrons to cool an electron-gas system. Our model is based on filtering electron subbands in a quantum-wire device. When electrons in higher subbands scatter out of the initial electron distribution, the system comes to equilibrium at a different chemical potential and a different temperature than the initial system. To study cooling in this system, we apply the Landauer formula. To calculate the transmission coefficients we use RMT. Our calculation shows that we can find device geometries for which this new equilibrium temperature is about 15% less than the initial temperature. We present experimental parameters for such a cooling device with InSb and GaAs.

As our second application, we use RMT to model an experimental observation of negative bend resistance (NBR) in 4-terminal InSb devices by Goel et al. at the University of Oklahoma. To model this experiment, we have used the RMT to calculate the transmission coefficients of electrons in the presence of a magnetic field. We calculate the magneto-transport properties in a four-terminal device and compare our results to the experimental observations.

Introduction

As the size of the semiconductor devices gets smaller they cross over from classical physics to quantum physics. These devices are sometimes called "mesoscopic" devices. The prefix "meso" means "in between" in Greek. With that meaning, mesoscopic physics is the physics of systems which are in the region between classical and quantum physics. The dimension of these systems can range from a few microns to few nanometers. These systems are different from the individual atomic systems and are too tiny to obey the laws of the macroscopic world.

The properties of these small devices are interestingly different from those of traditional classical devices. For instance, classical electrical conductors obey Ohm's law whereas quantum conductors do not. The latter can display ballistic propagation or conductance fluctuations depending upon the elastic mean free path.

There are different techniques to make these devices. Techniques like Molecular Beam Epitaxy (MBE) or Metal Organic Chemical Vapor Deposition allows us to grow thin layers of material that have precise composition and are nearly defect-free. In particular we can grow a thin layer of a low-band-gap material inside a sandwich of large-band-gap materials. In this thin layer, an electron at room temperature does not have enough energy to occupy the higher states in the growth direction, so electrons live in a two-dimensional world. This is called the "two-dimensional electron gas" (2DEG). These ultra-thin structures can show quantized properties. For instance, the quantized Hall Effect was observed [1] in these systems, introducing a whole field of new physics. Furthermore it is possible to design different devices on these two-dimensional structures by lithographical techniques that confine the transport in the

lateral direction. These devices can also be grown by changing the growth conditions that the system spontaneously forms the desired structures (self-assembly).

We can achieve different transport properties by changing the geometry of the two-dimensional device. We are mainly interested in their macroscopic properties, which can be measured in the laboratory. These macroscopic properties depend on microscopic properties of the system, because as you change the size and the shape of the system, the internal energy structure will be changed. This feature is similar to different atoms having different characteristics because they have different energy-level structures. Technologically it is very interesting that by changing the size and shape, we can change the internal electronic energy structure of a device and therefore change the observed properties.

Since it is possible to control the microscopic properties of bulk systems by different techniques, it is very important to understand what these macroscopic measurements, which are made using voltmeters or ammeters, mean for a quantum mechanical system. The theoretical understanding will help to design new devices based on existing experimental observations.

One way to understand of mesoscopic devices is the Landauer formalism, which was later extended by M.Bütikker to multi-terminal devices. The Landauer-Bütikker formula basically states that the results of macroscopic voltmeter/ammeter measurements are related to the transmission coefficients of electrons. In this theory, incident electrons see the specimen as a target and scatter into different leads. The transmission coefficients can be calculated classically (semi-classical model) or quantum mechanically.

The ultimate goal of this thesis is to explain existing observations and model new devices, based on InSb, in which the effective mass is small compared to other III-V semiconductors. Due to the small effective mass the electron confinement energies are large, so these devices are more likely to behave in a quantum mechanical fashion. We model these devices using quantum mechanical transmission coefficients in the

Landauer-Bütikker formula. While calculating the transmission coefficients requires only solving the Schrodinger equation inside the system, this task becomes hard when the system geometry is complicated. We need a powerful technique to calculate the transmission coefficients of electrons in a two-dimensional device quickly and accurately.

There are two main ways to handle this task. In one of these methods, the system is solved for one energy and the procedure is repeated for different energies to obtain the transport properties. The recursive Green's function technique [2, 3, 4] is an example of this kind. In the second type, the time-consuming energy independent part of the problem is separated from the rest of the problem, which makes the method computationally very efficient. The main theory in this thesis, R-Matrix Theory (RMT), is of this kind.

RMT allows to calculate the transmission coefficients of electrons at various energies without having to solve the Schrodinger equation repeatedly. RMT was originally developed in nuclear physics in 1947 (Wigner & Eisenbud) [5]. Later it was widely used in the atomic and molecular physics community. Recently, device physicists became interested in this technique [6, 7, 8]. We give a detailed background of the RMT and its applications in device physics in appendix (A) which is an excempt for our forthcoming paper [9]. In this thesis we improve and extend the RMT for solid-state devices. This thesis is structured as follows.

- **Chapter 1: Transport Properties from Scattering Theory**

  This chapter includes the basics of the Landauer formula and important results of this theory. We also explain the extension of the Landauer formula for multi-lead devices as done by M. Bütikker. We discuss this Landauer-Bütikker formalism for calculating the transport properties at finite temperature where we only consider the Fermi distribution broadening.

- **Chapter 2: Basics of the Variational R-matrix Theory**

In this chapter we discuss the R-matrix approach using variational basis functions, which is called variational R-matrix theory. We develop the necessary equations to solve for the transmission coefficients and apply the theory to one-dimensional systems: electrons traveling in a closed tube, and electrons traveling in an open tube. We discuss the convergence of the variational approach in detail.

- **Chapter 3: Two-Dimensional R-matrix Formula**

  We apply the RMT to a two-dimensional device with an arbitrary number of leads. We explain the technique using a T-junction device, although the final formula is general so we can use it for a device with any number of leads. We show results for the transmission coefficients of electrons traveling in a T-junction device and in a plus-junction device. We discuss convergence of the variational approach for two-dimensional RMT.

- **Chapter 4: Two-Dimensional R-Matrix Connection Formula**

  Sometimes the geometry of experimental devices is so complicated that it is hard to apply the R-matrix formula we discuss in the previous chapter to such devices. We present a new method for calculating the transmission coefficients of such a device. This new formula is called the "R-matrix connection formula". We explain the theory with an application: calculation of transmission coefficients for electrons traveling in a diamond geometry. Then we use the connection formula to calculate the transmission coefficients of electrons in a device with 4-terminal wedge geometry. This 4-terminal device is similar to the device made by Goel et.al [10] for experiments on the bend resistance in InSb devices.

- **Chapter 5: Evaporative Cooling of Electron in Semiconductor Devices**

  In this chapter, we propose a new device which uses the evaporative emission of electrons to cool an electron-gas system. This device is based on the selective

subband filtering. When the higher-subband electrons scatter out of the system, the rest of the system comes to a new equilibrium. Our calculation is based on Landauer-Bütikker theory. We calculate the transmission coefficients of electron using our variational RMT. Our calculation shows that we can find some device geometries such that the new equilibrium temperature is less than the initial temperature of the system. This is the desired cooling effect. We explain the theory with an ideal model, and then calculate the cooling parameter for several realistic devices. Finally, we calculate device parameters for such a cooling device with InSb and GaAs.

- **Chapter 6: Magneto-Transport Properties of Semiconductor Devices**

  In this chapter we model the experimental observations of negative bend resistance (NBR) in InSb devices by Goel et. al [11] at the University of Oklahoma. In order to model this experiment we extend our RMT to include the presence of an external perpendicular magnetic field. Since the device we are interested has a complicated geometry, we need to apply the R-matrix connection formula along with the magnetic-field RMT. We show how to solve for the transmission coefficients and calculate the magneto-transport properties in 4-terminal square junction device and in a 4-terminal wedge junction device.

- **Chapter 7: Conclusions**

Chapter 1

Transport Properties from Scattering Theory

In this chapter, we discuss the macroscopic transport properties of a quantum mechanical system, that is, the bridge between classical and quantum physics. This approach was founded by R. Landauer [12] for explaining the conductance of a two-terminal quantum mechanical device. The Landauer formula states that the conductance of a quantum mechanical system is proportional to the transmission coefficient of electrons through the device. Later this formula was extended by M. Bütikker [13] for multi-lead devices and the new formula is known as the Landauer-Bütikker formula.

This chapter is organized as follows. First, we discuss the origin of the quantum resistance through a two-terminal system (sec.1.1). There we explain how to apply the Landauer formula to a device operated at zero temperature. We then discuss how to calculate the finite-temperature conductance of a quantum mechanical system, and the important consequences of the Landauer formula.

In section (1.2), we discuss the extension of the Landauer formula to a multi-lead device. Then in section (1.3), we obtain an expression for a bend resistance, R_B of a four-terminal device which we will use in modeling the bend resistance of a InSb 4-terminal device in the chapter (6).

1.1 Landauer Formula for a Two-Terminal Device

We will discuss the current through a one-dimensional scatterer. The two reservoirs are internally connected by an ideal quantum wire and externally connected by a voltage source. We consider this conducting wire as a scatterer for the electrons through which they are transmitted with a probability T and reflected with a probability R [14].

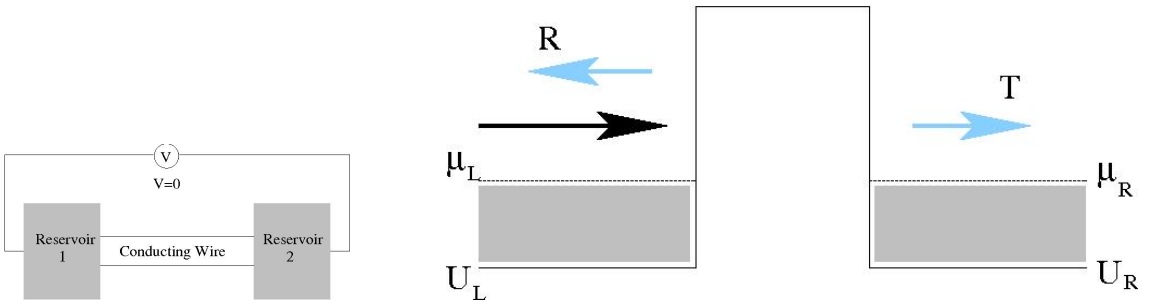

Figure 1.1: Two reservoirs are connected by a conducting wire (left figure) which is represented by a scatterer for the electron's path (right figure). The edges of the conductance band in left and right sides are denoted by U_L and U_R. The chemical potentials of both sides are equal because the applied voltage, $V = 0$. The net current flow through the reservoirs is zero.

We assume that the contacts between the conductor and the reservoirs are reflectionless so that electrons can enter the reservoirs without any difficulty. When there is no external voltage applied to the system, the chemical potentials of the two reservoirs are equal (fig.1.1). There is no net current flow between the reservoirs.

Now we apply a positive bias to the system such that the chemical potential of both sides differ by eV. That is,

$$eV = \mu_L - \mu_R. \tag{1.1}$$

We are interested in calculating the transport properties through the scatterer. We need to take two currents into account: the current due to the electrons emerging

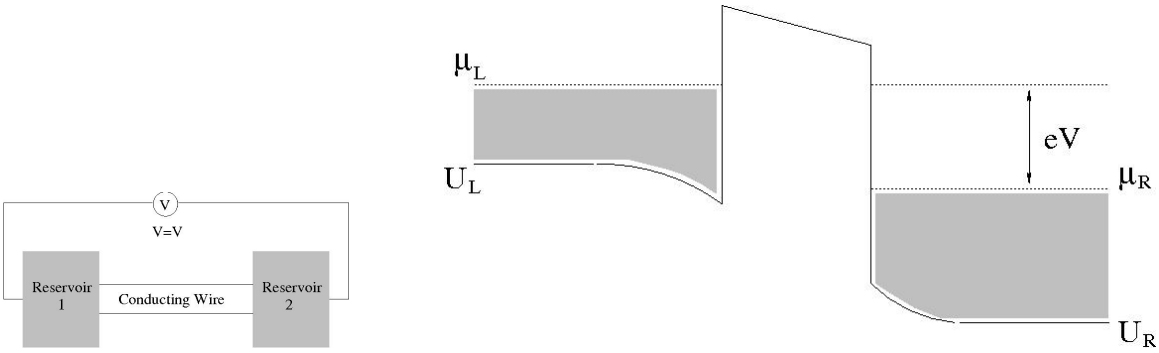

Figure 1.2: A positive bias voltage is applied across the one dimensional scatterer. There is a gap created between the chemical potentials of both sides such that $\mu_L - \mu_R = eV$.

from the left reservoir, I_L, and the current due to the electrons emerging from the right reservoir, I_R.

A particular current $I_{L,R}$ depends on:

- the density of states, $D(E)$,
- the Fermi function, $f(E, \mu_{L,R})$, the probability that an electron state at energy E is occupied or not,
- the velocity of the electron, $v(E)$,

and,

- the transmission coefficient, $T(E)$, the probability that an electron is transmitted through the device.

So the currents I_L and I_R are given by

$$I_L = 2e \int_{U_L}^{\infty} f(E, \mu_L)\ v(E)\ T(E)\ D(E)\ dE, \tag{1.2}$$

and

$$I_R = 2e \int_{U_R}^{\infty} f(E, \mu_R)\ v(E)\ T(E)\ D(E)\ dE, \tag{1.3}$$

where U_L and U_R are the edges of the conduction bands in left and right sides respectively. The factor 2 is for the double occupancy due to the spin degeneracy. Using the two currents, I_L and I_R, we can calculate the total current as,

$$\begin{aligned} I &= I_R - I_L \\ I &= 2e \int_{U_L}^{\infty} [f(E,\mu_L) - f(E,\mu_R)]\ T(E)\ D(E)\ v(E)\ dE. \end{aligned} \tag{1.4}$$

We consider the one-dimensional devices in which the density of states $D(E)$ is inversely proportional to the velocity of the particle [15] that,

$$D(E) = \frac{2}{\pi\hbar v(E)}. \tag{1.5}$$

Therefore the velocity cancels out from the above current equation leaving,

$$I = \frac{2e}{h} \int_{U_L}^{\infty} [f(E,\mu_L) - f(E,\mu_R)]\ T(E)\ dE. \tag{1.6}$$

Equation (1.6) gives a general expression for the current through a one-dimensional device. We consider that the applied bias is such that,

$$\mu_L = \mu + \frac{1}{2}eV, \tag{1.7}$$

and,

$$\mu_R = \mu - \frac{1}{2}eV, \tag{1.8}$$

where μ is the equilibrium chemical potential when there is no applied bias.
When we expand the Fermi function in a Taylor series and keep only the 1st order terms, this gives,

$$f(E,\mu_L) - f(E,\mu_R) = -eV\frac{d}{dE}\, f(E,\mu). \tag{1.9}$$

By plugging the equation (1.9) in the equation (1.6), we get an equation for the total current through the scatterer,

$$I = \frac{2e^2V}{h} \int_{U_L}^{\infty} \left[-\frac{d}{dE} f(E,\mu)\right] T(E) dE. \tag{1.10}$$

1.1.1 Temperature Dependence of the Conductance

The equation (1.10) is true for the current at any temperature. At zero temperature, the Fermi function is a step function that $-\frac{d}{dE}f(E,\mu) = \delta(E-\mu)$. So the integration will be reduced to,

$$I = \frac{2e^2V}{h}T(\mu), \tag{1.11}$$

which gives an expression for the zero temperature conductance G of a two-terminal device as,

$$G = \frac{2e^2}{h}T(\mu). \tag{1.12}$$

This is the well-known two-terminal Landauer formula [14].

At a finite temperature, we use the equation (1.10) to calculate the current through the device. The Fermi distribution function is no longer a step function, but broadened. It shows that, in order to get the total average transmission coefficient of electrons we need to integrate it over the broadened Fermi distribution as,

$$T = \int_{U_L}^{\infty} \left[-\frac{d}{dE}f(E,\mu)\right] T(E)dE. \tag{1.13}$$

In the following subsection, we will discuss some important consequences of the Landauer formula.

1.1.2 Important Comments on Landauer formula

The two-terminal Landauer formula (eq.1.12) leads to several physical insights such as, quantum unit of resistance, contact resistance, phase relaxation of electrons at the reservoirs and the non-locality of quantum resistance as we will describe below.

The Landauer formula states that the conductance is directly proportional to the transmission coefficient T of the electrons, and the proportionality constant does not depend on the device parameters but on fundamental constants. With this proportionality constant, the fundamental unit of quantum resistance was recognized as $\frac{e^2}{h} = 25.8\text{k}\Omega$, which is now known as the Klitzing constant [16].

The Landauer formula also states that as the transmission through the scatterer increases, the conductance of the system will be increased. If we assume that the conducting wire is a perfect transmitter ($T = 1$), then our physical insight is that the conductance will be infinity. However when we substitute $T = 1$ in eq. (1.12), we get a finite conductance which is puzzling. The reason for this puzzle is that the Landauer formula can be presented in two forms. In the form we presented here (eq.1.12), we have not subtracted the resistance due to the contacts between the leads and the reservoirs [17]. In fact the resistance is measured further away from the scatterer, the resistance is not solely due to the scatterer. Since the resistance is additive, we explain more about this in terms of the resistance not in terms of the conductance. When we have $T = 1$, the finite conductance is due to the contacts that the contact resistance is given by,

$$R^{\text{contact}} = \frac{h}{2e^2}. \tag{1.14}$$

If we measure the resistance across the scatterer, we get the resistance due to the scatterer, $R^{\text{scatterer}}$. However, when me measure the resistance further away from the scatterer, we get the resistance due to the scatterer and the contacts as well, which can be mathematically written as,

$$\begin{aligned} R &= R^{\text{scatterer}} + R^{\text{contact}} \\ \frac{h}{2e^2}\frac{1}{T} &= R^{\text{scatterer}} + \frac{h}{2e^2} \\ R^{\text{scatterer}} &= \frac{h}{2e^2}\left[\frac{1-T}{T}\right]. \end{aligned} \tag{1.15}$$

Therefore the Landauer formula is sometimes written in the form,

$$G = \frac{2e^2}{h}\frac{T}{1-T}. \tag{1.16}$$

For a perfect scatterer, the equation (1.16) correctly shows infinite conductance. One should be aware of these two forms of the Landauer equation. In our calculation, we use the earlier form in which the resistance is measured away from the scatterer.

Another important consequence of the Landauer formula is that it shows the phase relaxation of the electrons. As we proved the Landauer formula, we considered

the perfect elastic collisions that there is no energy dissipation through these events. However, the final result is the resistance which is a dissipative quantity. The question is, if the electron collisions are elastic, where does this dissipation come from? If the resistance is defined just across the scatterer, there is no energy dissipation. So we cannot define the resistance of the scatterer as a local quantity. In order to explain the dissipation, we need to consider the motion of the electrons out side the scatterer. The Landauer model assumes that all the electrons enter into a reservoir from the conductor never reflects back to the conductor. That is, there is no phase relation between the incoming and outgoing electrons in a particular reservoir. When electrons enter into a reservoir, they relax at a equilibrium temperature and a chemical potential. All the dissipation occurs due to this phase relaxation of electrons in the reservoirs. This highlights two important concepts, the phase relaxation of electrons and the non locality of the quantum resistance. The resistance cannot be defined for the scatterer itself, but for the system.

1.2 Landauer-Bütikker Formula

The Landauer formula was originally developed for a two-terminal device [14]. This formula was extended to a multichannel and multi-lead device by M. Bütikker [13] and it is called the Landauer-Bütikker formula. In this section we discuss this extension in detail and apply it to a 4-terminal device to obtain an expression for the bend resistance, R_B [15], which we will discuss in detail in the thesis (ch.6).

In a multi-lead device some leads are used to inject currents (current probes) and some leads are used to measure the voltages (voltage probes). We assume that the voltage probes draw zero net current as they have infinite resistance. A finite current is passed only through the current probes.

We shall consider an arbitrary device (fig.2.1) which has N leads. Each of these leads has a number of transverse channels (subbands) which we will discuss in detail in the chapter (3). These leads are connected to electron reservoirs. Each of these

reservoirs injects electrons into the system. According to Landauer formula, the current is proportional to the transmission coefficient from one lead to another. The current in lead q due to the electrons injected from the lead p,

$$I_{q,p} = -\frac{e^2}{\pi\hbar}\, V_p \sum_{n_q}^{N_q} \sum_{n_p}^{N_P} \mathcal{T}^{q,p}_{n_q,n_p}, \tag{1.17}$$

where we have use the equation (1.12). Here $\mathcal{T}^{qp}_{n_q,n_p}$ is the transmission coefficient of electrons from the n_p^{th} subband of the pth lead to the n_q^{th} subband of the qth lead and V_p is the applied voltage. There are N_q number of open subbands in each qth lead. The negative sign in the current expression is due to our convention that, the incident current in each lead is positive.

The equation (1.17) has the current in the qth lead due to the lead p. The qth lead injects current to the system in N_q subbands. A fraction of this injected current reflects back to the qth lead. The current in the lead q due to the electrons emerging from the lead q,

$$I_{qq} \;=\; \frac{e^2}{\pi\hbar}\, V_q \left[N_q - \sum_{n_q}^{N_q} \sum_{n_q'}^{N_q} \mathcal{T}^{qq}_{n_q,n_q'} \right], \tag{1.18}$$

where $\mathcal{T}^{qq}_{n_q,n_q'}$ is the probability that the electrons reflect back to the n_q^{th} subband in the qth lead. Hereafter we use only the transmission coefficients from one lead to another, T_{qp}, which is defined as,

$$T_{qp} = \sum_{n_q}^{N_q} \sum_{n_p}^{N_p} \mathcal{T}^{qp}_{n_q,n_p}. \tag{1.19}$$

With this notation the total net current in the qth lead is,

$$I_q \;=\; \frac{e^2}{\pi\hbar} \left[(N_q - T_{qq})\, V_q - \sum_{p\neq q} T_{qp} V_p \right], \tag{1.20}$$

which is called the Landauer-Bütikker (LB) formula. The LB formalism can also be written in terms of the conductance matrix as,

$$I_q = \sum_p \mathsf{G}_{qp} V_p, \tag{1.21}$$

where ,

$$\mathsf{G}_{qp} = \frac{e^2}{\pi\hbar}\left[\left(N_q - T_{qq}\right)\delta_{qp} - T_{qp}\right]. \tag{1.22}$$

Here we discuss how to obtain the experimentally significant quantities through the LB formula. We start with the conductance matrix [15]. The conductance matrix, G obeys some specific properties due to some physical conditions as we describe follows. The conservation of current gives the relation,

$$N_q - T_{qq} = \sum_p T_{pq}. \tag{1.23}$$

This states that the sum of elements in a column of the conductance matrix equals zero, which makes the conductance matrix singular.

We can also simplify the conductance matrix because, if there is no voltage difference between the leads, there is no current flow which makes the sum of all the elements in a row of the conductance matrix equal to zero. Since both the sums in the rows and in the columns are zero, we get the relation

$$\sum_q T_{pq} = \sum_p T_{pq} = 0. \tag{1.24}$$

With these relations the total current in the qth lead of the system can be written as

$$I_q = \frac{e^2}{\pi\hbar}\left[\sum_{q\neq p} T_{pq}V_q - \sum_{p\neq q} T_{qp}V_p\right]. \tag{1.25}$$

Now we will consider the sum rule (eq.1.24) for the rows and columns of the conductance matrix. We can subtract the diagonal term from the eq. (1.24) which gives

$$\sum_{q\neq p} T_{qp} = \sum_{p\neq q} T_{pq}. \tag{1.26}$$

Now the current in the qth lead is given by

$$I_q = \frac{e^2}{\pi\hbar}\sum_{q\neq p}\left[T_{pq}V_q - T_{qp}V_p\right]. \tag{1.27}$$

1.3 Bend Resistance from the Landauer Bütikker Formula

We are mainly interested in measurements taken in 4-terminal devices, since we ultimately model the experimental observation made in those 4-terminal devices. We will consider one such experimental quantity, the bend-resistance.

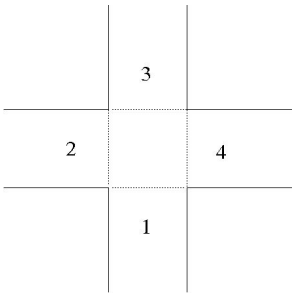

Figure 1.3: A schematic diagram of a 4-terminal device used in the bend resistance experiment. A current I_{14} is injected from the lead 4 to 1 and the voltage created between the leads 2 and 3, V_{23}, is measured. There is a magnetic field perpendicular to the device. The bend resistance, $R_B = V_{23}/I_{14}$ is measured as a function of the strength of the magnetic field [10].

In the bend resistance experiment (fig.1.3), a current I_{14} is injected from the lead 4 to 1, and the voltage, V_{23} is measured between the leads 2 and 3. The bend resistance is defined as,

$$R_B = \frac{V_{23}}{I_{14}}. \tag{1.28}$$

We can use the Landauer-Bütikker formula to get an expression for the bend-resistance in terms of the transmission coefficients of electrons in the device.

We can write the conditions for the electron flow in this system as,

$$I_1 = I, \tag{1.29}$$

$$I_2 = 0, \tag{1.30}$$

$$I_3 = 0, \tag{1.31}$$

$$I_4 = -I. \tag{1.32}$$

Since the leads 2 and 3 are voltage probes, there is no current through those leads (eq.1.30 and 1.31) and a similar current passes through the leads 1 and 4 (eq.1.29 and 1.32). This experimental information together with the equation (1.27) can be put in a matrix form as,

$$\begin{pmatrix} T_{12}+T_{13}+T_{14} & -T_{12} & -T_{13} & -T_{14} \\ -T_{21} & T_{21}+T_{23}+T_{24} & -T_{23} & -T_{24} \\ -T31 & -T_{32} & T_{31}+T_{32}+T_{34} & -T_{34} \\ -T_{41} & -T_{42} & -T_{43} & T_{41}+T_{42}+T_{43} \end{pmatrix} \begin{pmatrix} V_1 \\ V_2 \\ V_3 \\ V_4 \end{pmatrix} = \frac{\pi\hbar}{e^2} \begin{pmatrix} I \\ 0 \\ 0 \\ -I \end{pmatrix} \tag{1.33}$$

This set of equations is linearly dependent. One of the equation is redundant. We eliminate one equation (we choose to eliminate eq.1.32) out of the set since it does not carry any new information. Now the equation becomes,

$$\begin{pmatrix} T_{12}+T_{13}+T_{14} & -T_{12} & -T_{13} & -T_{14} \\ -T21 & T_{21}+T_{23}+T_{24} & -T_{23} & -T_{24} \\ -T_{31} & -T_{32} & T_{31}+T_{32}+T_{34} & -T_{34} \end{pmatrix} \begin{pmatrix} V_1 \\ V_2 \\ V_3 \\ V_4 \end{pmatrix} = \frac{\pi\hbar}{e^2} \begin{pmatrix} I \\ 0 \\ 0 \end{pmatrix}$$

Our goal is to find an expression for the experimentally measured quantity, the bend resistance $R_B = (V_2 - V_3)/I$. We choose to measure all the voltages with respect to

the voltage of the lead 3, and make $V_3 = 0$, which reduces the above equation to,

$$\begin{pmatrix} T_{12}+T_{13}+T_{14} & -T_{12} & T_{14} \\ -T21 & T_{21}+T_{23}+T_{24} & -T_{24} \\ -T_{31} & -T_{32} & -T_{34} \end{pmatrix} \begin{pmatrix} V_1 \\ V_2 \\ V_4 \end{pmatrix} = \frac{\pi\hbar}{e^2} \begin{pmatrix} 0 \\ I \\ 0 \end{pmatrix}$$

This is a set of linearly independent equations which we would like to solve for V_2/I. This gives an equation for the bend resistance, R_B as,

$$R_B = \frac{h}{2e^2} \frac{T_{41}T_{21} - T_{31}^2}{S}, \tag{1.34}$$

where S is given by,

$$S = (T_{21} + T_{41}) \left[(T_{21} + T_{31})^2 + (T_{41} + T_{31})^2 \right]. \tag{1.35}$$

1.4 Conclusion

We have discussed Landauer and Landauer-Bütikker formulas to explain the transport properties of two-dimensional devices. In the Landauer approach, the transport properties are explained in terms of the transmission coefficients from one lead to another. We discussed how to calculate the temperature dependent transport properties and obtained an expression for the bend resistance measured in a 4-terminal device. In the later chapters of this thesis we explain one efficient technique, R-matrix theory, to calculate the transmission coefficients of a multi-lead device. Then we apply the Landauer theory to model devices (ch.5) and explain the existing experimental observations (ch.6).

Chapter 2

Basics of the Variational R-Matrix Theory

2.1 Introduction

In the previous chapter we learned about the importance of scattering theory in solid state devices and in the introduction we mentioned about the standard techniques used to calculate the transmission coefficients of electrons in solid-state devices. In this chapter we discuss one such technique, the R-matrix theory (RMT) in detail.

Our goal is to develop this technique to calculate the transmission coefficients in two-dimensional devices such as quantum wire configurations. A schematic digram of such a device is sketched in figure (2.1). In this two-dimensional device, there are several leads attached to an interior region "A". In the one-dimensional case (sec.1.1), we called the interior region as the "scatterer". In particular it is part of the device where the scattering occurs. Reservoirs and the interior region "A" are connected with the leads as shown in the figure (2.1). Electrons are injected into the system by an external source through these leads. Electrons scatter in the interior region and emerge through the leads. We need to find the transmission coefficients of the electrons in each lead at a given energy, E when only one incoming subband

is occupied.

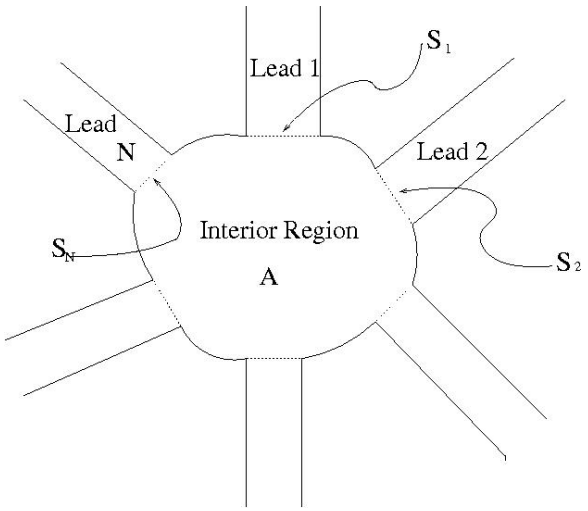

Figure 2.1: A schematic diagram of a two-dimensional device for the scattering calculation. The surfaces $S_1, S_2, \cdots, S_N$ separate the interior region A from the leads. We seek the transmission coefficients of outgoing electrons in the leads when one incoming subband is occupied.

R-matrix theory is a way to calculate the transmission coefficients of such a device without having to calculate the total scattering wave function of the system. Our theoretical model is based on several assumptions:

- The electron transport in the device is ballistic; there is no electron-electron scattering or electron-phonon scattering, all the scattering occurs due to the boundaries. The transport of electrons is independent of the other electrons and phonons, thus we can use the single electron model. In the single electron model, the properties of the system can be obtained by solving the single particle Schrodinger equation.

- These two-dimensional devices are lithographically designed on a periodic crystal potential (the lattice of the material of which the quantum well is made). We assume that this periodic potential can be represented by the effective mass approximation [18]. In the relevant equations the free electron mass m is replaced

by the effective mass m^*. The values of m^* are known for different materials [19]

- The leads of the device (fig.2.1) have Cartesian symmetry. The qth lead can be described by (x_q, y_q) coordinates. The transverse confining potential energy of the lead q, $V_q(y_q)$ in each lead is an infinite square well whose width w_q equals the separation of the (impenetrable) walls of the lead:

$$\begin{aligned} V_q(y_q) &= \infty \quad y_q \leq w_q/2 && (2.1)\\ &= 0 \quad -w_q/2 \leq y_q \leq w_q/2 && (2.2)\\ &= \infty \quad y_q \geq w_q/2 && (2.3) \end{aligned}$$

  Due to these boundary conditions, electrons are confined to the leads in the transverse direction and we assume that the longitudinal potential energy $V(x_q)$ in each lead is a constant whose value we shall take as zero.

With these assumptions, one could calculate the transmission coefficients of electrons in a device at a given energy E by solving the Schrodinger equation to get the total scattering wave function of the system. Knowing the scattering wave function, we could calculate the electron flux going through each lead.

However, when the system geometry becomes complicated, it is hard to solve the Schrodinger equation in the device. If we need to calculate the transmission coefficients at many energies, this would require solving the Schrodinger equation many times making the calculations even slower.

On the other hand, we need the transmission coefficients in the leads, not in the interior region. In fact we do not need to solve for the total scattering wave function in the device at all.

In RMT, in order to get the transmission coefficients in the leads, we do not solve for the scattering wave function in the device. The basic idea is that we divide the system into two parts, the interior scattering region and the outgoing leads. The

interior region is where all the scattering occurs and the leads are uniform regions by which electrons enter and leave the system (fig.2.1).

We expand the scattering wave function in the leads in a linear combination of the lead eigenfunctions. With the hard wall boundary conditions (eq.2.3) and Cartesian symmetry, the lead eigenfunctions are the product of plane waves along the wire and the infinite well wave functions in the transverse direction. In the interior region, the scattering wave function can be expanded as a linear combination of the interior region eigenfunctions. Then we match these two types of solutions on the boundaries where the leads meet the interior region (hereafter we call those boundaries the "soft boundaries") to calculate the transmission coefficients in the leads.

In this chapter we explain the procedure for R-matrix theory in devices in detail. This chapter is structured as follows.

Section (2.2) introduces the basic concepts and develops the necessary equations for the R-matrix formula. To develop the basic equation, we mainly need to solve the interior region problem. In explaining the interior region problem, we introduce the Bloch Hamiltonian, one of the key points in the R-matrix theory.

After explaining the R-matrix formula in sec (2.2), we proceed to the rest of the details of the RMT using two simple examples; the scattering of electrons traveling in a closed tube (sec.2.3) and the scattering of electrons traveling in an open tube (sec.2.4). These are the simplest examples one could think of. The answers to both these problems are straight forward. In the closed tube, the electrons have reflection amplitude -1, and in the open tube, electrons have transmission amplitude 1. However, we solve these systems as scattering problems to explain all the details of the technique. In particular, the closed tube problem has similarities to the spherical R-matrix theory which is popular in nuclear/atomic/molecular physics. When extending the technique from closed tube problem to the open tube problem, we can observe the difference in R-matrix theory from nuclear/atomic/molecular physics to device physics.

Both these sections of RMT applications (section 2.3 and 2.4) are structured in a similar fashion. However, some common techniques such as the generalized eigenvalue problem, are described only in the first application (sec.2.3). In those two sections, we explain the interior region problem and show the calculation of R-matrix elements using different methods. We discuss the advantage of variational RMT in handling the interior region problem through convergence studies of R-matrix elements. Use of variational RMT is one of the main innovations of this research. Then we show how to connect the outgoing lead solutions and the interior region solutions and how to calculate the transmission coefficients of the electrons.

Concluding that the variational R-matrix theory achieves faster convergence that the Wigner-Eisenbud calculation (by the results of sections 2.3 and 2.4), in section(2.5) we discuss the reasons for this convergence. While our analysis shows that convergence is non-uniform, the mathematical explanation for this property remains unexplained.

2.2 R-Matrix Formula

In this section, we develop the mathematical equations to formulate the R-matrix equation and give the physical conditions in which it is applicable. For simplicity, in this chapter, we explain the theory in one dimension. In later chapters, we extend the theory to more dimensions and more complicated geometries.

We consider an electron injected to the device (fig.2.1) at an energy E, where E is the total energy of the incoming electron. We look for a solution to the time independent Schrodinger equation,

$$\mathcal{H}\left|\Psi_E\right\rangle = E\left|\Psi_E\right\rangle, \tag{2.4}$$

where the Hamiltonian $\mathcal{H}$ is given by,

$$\mathcal{H} = -\frac{\hbar^2}{2m^*}\frac{\partial^2}{\partial\tilde{x}^2} + V(\tilde{x}). \tag{2.5}$$

We consider two types of solutions for the equation (2.4), the interior region solution and the lead solution, and match these solutions on the soft boundaries to

get the transmission coefficients in the leads. These boundaries are marked as $\mathcal{S}_i$ in the fig. (2.1), and we call the interior region "A".

Below we discuss the interior region solution and later in the sections (2.3 and 2.4) we discuss the lead solution using some examples.

We need to expand the scattering state $|\Psi_E\rangle$, in terms of $|\zeta_j\rangle$ which are eigenvectors of the interior region Hamiltonian. We shall consider the eigenstates in the coordinate space.

These eigenfunctions $|\zeta_j(\tilde{x})\rangle$ are obtained by solving the equation,

$$\mathcal{H}\,|\zeta_j(\tilde{x})\rangle = E_j\,|\zeta_j(\tilde{x})\rangle\,, \tag{2.6}$$

where $\tilde{x}$ is the spatial coordinate of the system.

Can we expand the scattering wave function $|\Psi_E(\tilde{x})\rangle$ in terms of $|\zeta_j(\tilde{x})\rangle$? Is this set of eigenfunctions $|\zeta_j(\tilde{x})\rangle$ complete?

Bloch [**?**] found that even though the Hamiltonian in equation (2.5) is Hermitian in infinite systems, the Hamiltonian is not in general Hermitian in a finite system unless certain boundary conditions are specified. For instance, if we solve the Hamiltonian inside the interior region with zero value or zero derivative boundary conditions, the Hamiltonian will be Hermitian as we will describe below. We will show the non-Hermiticity of the Hamiltonian inside a finite system below.

We consider a one-dimensional finite region defined by $-a/2 \leq \tilde{x} \leq +a/2$, where $\tilde{x}$ is the space coordinate and a is the length of the system. We start with the single particle Hamiltonian (eq.2.5).

Before explaining any details of the problem, we make the Hamiltonian dimensionless. First we scale the position variable $\tilde{x}$ by some arbitrary convenient length a. Changing the variables to $x = \tilde{x}/a$,

$$\mathcal{H} = -\frac{\hbar^2}{2m^*a^2}\frac{\partial^2}{\partial x^2} + V(x). \tag{2.7}$$

Now we scale the energy by $E_o = \hbar^2/m^*a^2$. We get

$$\mathcal{H} = \frac{\mathcal{H}}{E_o} = -\frac{1}{2}\frac{\partial^2}{\partial x^2} + V(x) \tag{2.8}$$

Hereafter we work with these dimensionless energies and lengths. For instance now our finite system is defined as $-1/2 \leq x \leq +1/2$. The computation is easier when done with dimensionless parameters. We change these dimensionless parameters to real parameters when we apply these models to experiments.

Here we explain why the Hamiltonian (here the kinetic energy operator) is not Hermitian inside a finite region. If the Hamiltonian were Hermitian in the finite region, two eigenfunctions of $\mathcal{H}$, f and g, should satisfy

$$\left(f, -\frac{1}{2}\frac{\partial^2 g}{\partial x^2}\right) = \left(-\frac{1}{2}\frac{\partial^2 f}{\partial x^2}, g\right), \tag{2.9}$$

where the parenthesis, ( ) denotes the volume integration in the finite region. In one dimension the volume integration becomes an integration over the length. Then the LHS of the eq.(2.9) becomes,

$$\left(f, -\frac{1}{2}\frac{\partial^2 g}{\partial x^2}\right) = -\int_{-1/2}^{+1/2} f(x)\ \frac{1}{2}\ \frac{\partial^2}{\partial x^2} g(x) dx \tag{2.10}$$

We have assumed a free particle so that the potential $V(x) = 0$. The above equation (2.9) means that if the kinetic energy operator were Hermitian, it could act on the function as a left handed operator and a right handed operator. We will consider the left hand side (LHS) and the right hand side (RHS) of eq.(2.9) to check for the Hermiticity of the kinetic energy operator.

The left hand side (LHS) of the equation (2.9) is,

$$LHS = \left(f, -\frac{1}{2}\frac{\partial^2 g}{\partial x^2}\right). \tag{2.11}$$

Doing the integration by parts we get,

$$LHS = \left[-\frac{1}{2} f(x) \frac{\partial}{\partial x} g(x)\right]_{-\frac{1}{2}}^{\frac{1}{2}} + \int_{-\frac{1}{2}}^{\frac{1}{2}} \frac{1}{2}\frac{\partial}{\partial x} f(x) \frac{\partial}{\partial x} g(x) dx. \tag{2.12}$$

Similarly, we can write an equation for the RHS of eq.(2.9),

$$RHS = \left[-\frac{1}{2} g(x) \frac{\partial}{\partial x} f(x)\right]_{-\frac{1}{2}}^{\frac{1}{2}} + \int_{-\frac{1}{2}}^{\frac{1}{2}} \frac{1}{2}\frac{\partial}{\partial x} f(x) \frac{\partial}{\partial x} g(x) dx. \tag{2.13}$$

It is clear that the LHS and RHS in eq.(2.9) are not equal unless the first terms in equations (2.12) and (2.13) are equal, which is in general not true. For example, those two terms will be equal if the interior region eigenfunctions satisfy special boundary conditions (zero value or zero derivative boundary conditions) on the soft boundaries. However, our final scattering wave function does not obey any specific boundary conditions on the boundaries of the interior region. It is not convenient to solve the interior region eigenfunctions with specific boundary conditions. If the Hamiltonian does not satisfy the Hermiticity (eq.2.9), its eigenfunctions are not complete. The eigenfunctions of the Hamiltonian, $|\zeta_j(x)\rangle$ could not be used to expand the scattering wave function.

In a finite region, the Hamiltonian is not Hermitian because of the boundary terms in (eq.2.12). If we subtract the boundary terms, the rest will be Hermitian. This Hermitian operator is called the Bloch Hamiltonian and the boundary terms we add to $\mathcal{H}$ are called the Bloch operators. The new Bloch Hamiltonian takes the form,

$$\mathcal{H}_B = H_0 + \mathcal{L}. \tag{2.14}$$

For example, for the kinetic energy operator defined in the finite region $-1/2 \leq x \leq 1/2$, the Bloch operator takes the form,

$$\mathcal{L} = \frac{1}{2}\left[-\delta(x+\frac{1}{2}) + \delta(x-\frac{1}{2})\right]\frac{\partial}{\partial x}. \tag{2.15}$$

The Bloch operator is a sum over all surfaces. In general the Bloch operator has the form,

$$\mathcal{L} = \frac{1}{2}\sum_{s'}(\delta(x-s'))\,\hat{n}\cdot\vec{\nabla}\Psi_{s'}. \tag{2.16}$$

The unit vector $\hat{n}$ is perpendicular to each of the soft boundaries and points outward from the interior region "A".

The Bloch Hamiltonian $\mathcal{H}_B$ has a set of eigenfunctions $|\phi_j(x)\rangle$ defined by,

$$(\mathcal{H}_B - E_j)\phi_j(x) = 0, \tag{2.17}$$

where the spatial coordinate x is defined only inside the interior region "A". As we have proved, since the Bloch Hamiltonian is Hermitian inside the interior region, this set $|\phi_j(x)\rangle$ is complete and orthogonal inside the interior region.

This set of eigenfunctions (which we call the Bloch eigenfunctions) $|\phi_j(x)\rangle$ can be used to expand the scattering wave function inside the interior region as

$$|\Psi_E(x)\rangle = \sum_j^{\infty} C_j \, |\phi_j(x)\rangle \, . \tag{2.18}$$

This expansion is valid only inside the interior region, since the set $|\phi_j(x)\rangle$ is defined only in the interior region. We need to find the expansion coefficients, $C_j = \langle\phi_j(x)|\Psi_E(x)\rangle$ in eq. (2.18). Below we explain how to obtain an expression for these coefficients.

We rearrange eq.(2.4) as

$$(\mathcal{H} + \mathcal{L} - E) \, |\Psi_E\rangle = \mathcal{L} \, |\Psi_E\rangle \, , \tag{2.19}$$

with the goal of obtaining the expansion coefficients C_j. By rearranging eq.(2.19),

$$|\Psi_E(x)\rangle = \frac{1}{\mathcal{H} + \mathcal{L} - E} \mathcal{L} \, |\Psi_E(x)\rangle \, , \tag{2.20}$$

we get C_j as

$$C_j = \langle\phi_j(x)|\Psi_E(x)\rangle = \frac{1}{\mathcal{H} + \mathcal{L} - E} \, \langle\phi_j(x)| \, \mathcal{L} \, |\Psi_E(x)\rangle \, , \tag{2.21}$$

which reduces to

$$C_j = \frac{1}{E_j - E} \, \langle\phi_j(x)| \, \mathcal{L} \, |\Psi_E(x)\rangle \, , \tag{2.22}$$

where E_j's are the eigenvalues of the Bloch Hamiltonian corresponding to the Bloch eigenfunction $|\phi_j(x)\rangle$.

Substituting the expression for C_j in equation (2.18), we get,

$$|\Psi_E(x)\rangle = \sum_j^{\infty} \frac{|\phi_j(x)\rangle}{E_j - E} \left\langle \phi_j(x') \, \mathcal{L} \, \middle| \Psi_E(x') \right\rangle . \tag{2.23}$$

Note that $x^{'}$ lies on the surface of the interior region and it goes over all surfaces as it is required by the Bloch operator (according to the delta function in eq.2.16) and the point x can be anywhere inside the interior region. The point x is always inside the interior region "A". In order to calculate the transmission coefficients in the leads, we need to relate the interior region and the leads. So we consider the equation (2.23) on the soft boundary on the lead q ($x = s_q$, where s_q is a point on the boundary q). We denote $x^{'} = s_p$ where s_p is a point on the soft boundary p, since the point $x^{'}$ lies on the soft boundaries. So with this we write the equation (2.23) on a point s_q as,

$$|\Psi_E(s_q)\rangle = \sum_j^{\infty} \frac{|\phi_j(s_q)\rangle}{E_j - E} \langle \phi_j(s_p) \, \mathcal{L} \, |\Psi_E(s_p)\rangle \, . \tag{2.24}$$

We rearrange the equation (2.24) as,

$$|\Psi_E(s_q)\rangle = \sum_j^{\infty} \frac{|\phi_j(s_q)\rangle \langle \phi_j(s_p)|}{E_j - E} \mathcal{L} \, |\Psi_E(s_p)\rangle \, . \tag{2.25}$$

This is the R-matrix equation. We identify the term,

$$R(E, s_q, s_p) = \sum_j^{\infty} \frac{1}{2} \frac{|\phi_j(s_q)\rangle \langle \phi_j(s_p)|}{E_j - E}, \tag{2.26}$$

as the R-matrix which simplifies the equation (2.24) to,

$$|\Psi_E(s_q)\rangle = \sum_p R(E, s_q, s_p) \vec{\nabla} \, |\Psi_E(s_p)\rangle \, . \tag{2.27}$$

Note that the summation over p comes in the equation (2.27) is due to the summation appear in the Bloch operator (eq.2.16). Also note that the equation (2.27) is true if there is no potential in the system since we have considered $V(x) = 0$ when obtaining the equation (2.16). If there is a potential term we have to find out whether it is Hermitian or not. If the potential takes the typical form $V(x)$, then it is Hermitian. If the potential energy Hamiltonian does not contribute to the Bloch operator, eq.(2.27) is still valid. If the Hamiltonian contains derivatives, it is not Hermitian and we have to find out the relevant Bloch operator term. This issue is addressed in the chapter (6) where we study the magneto-transport properties of solid-state devices.

We use equation (2.24) to calculate the transmission coefficients of the system. In this chapter we consider only the one-dimensional problems. We use the technique for two-dimensional devices in the chapter (3). We explain the total procedure of the R-matrix theory with two applications, the electron transmission through a closed tube (section.2.3) and the electron transmission through an open tube (section.2.4) . Both these problem are very simple problems, however they are important. The closed tube problem has direct relation to the spherical problem in content and having two soft boundaries, open tube problem shows the application of RMT in a non-spherical device.

2.3 Application of the R-Matrix Theory to Electron Transmission through a Closed Tube

We consider an electron moving through a closed tube, (fig.2.2). We call it a tube, however, we consider it completely as a one-dimensional problem suppressing the transverse degree of freedom. Even though the answer to this problem is straightforward, we do it as a scattering problem to explain the technique. This problem is analogous to the spherical R matrix problem in atomic and nuclear physics in that they both have one soft boundary. Since we know the exact answer to this scattering problem (all the electrons will reflect back to the right hand side region with a reflection coefficient 1), we can study and analyze the technique by solving this problem. In the following section, we calculate the required R-matrix elements and in the section after, we use the R-matrix elements to calculate the transmission coefficients.

2.3.1 Calculation of the R-Matrix Elements

The first steps of the R-matrix theory are to identify the interior scattering region, find the Bloch Hamiltonian, and calculate the Bloch Hamiltonian eigenfunctions in the interior region. We define a interior region $0 \leq x \leq L$ which is the shaded region

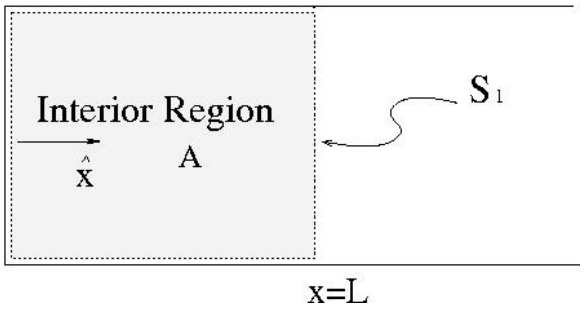

Figure 2.2: A schematic diagram of a closed tube for the R-matrix theory calculation. We artificially divide the system into two parts defining the interior region as A. Electrons are injected from $x > L$. Supposing that electrons undergo scattering in region A, we seek the transmission coefficient in the region, $x > 0$.

in fig.(2.2) where L is dimensionless. According to eq. (2.26), the R-matrix depends on two points in space, s_q and s_p. However, in this problem, we have only one soft boundary so the R-matrix is a single value or a 1×1 matrix. It is easy to show how this single R matrix element is related to the scattering wave function $|\Psi_E(x)\rangle$. The Bloch operator for this system takes the form,

$$\mathcal{L}_B = \frac{1}{2}\delta(x - L)\frac{\partial}{\partial x}.$$

Note that we work in the dimensionless uints. By putting the Bloch operator in the eq. (2.24),

$$|\Psi_E(L)\rangle = R(E, L, L)\frac{\partial}{\partial x}\Psi_E(L). \tag{2.28}$$

That is, the R-matrix,

$$R(E, L, L) = \frac{|\psi_E(L)\rangle}{\frac{d}{dx}|\Psi_E(L)\rangle}, \tag{2.29}$$

is the inverse of the logarithmic derivative of the scattering wave function evaluated at the soft boundary. This is equivalent to the result we see in the conventional spherical R-matrix theory. Since we have only one soft boundary, some times it is denoted as $R_{E,L}$.

We calculate the R-matrix elements using the interior region Bloch eigenfunctions according to eq. (2.26). However for a general scattering problem, it is not possible

to perform the infinite summation as given by eq. (2.26). We have to truncate the summation. If one could perform the infinite summation as required, we would get the exact answer without depending on the numerical methods we used. Since we can only do a finite summation, the way we calculate the Bloch eigenfunctions plays an important role in the convergence of the R-matrix calculation.

However for this simple problem, we can perform the infinite summation over j as in eq. (2.26) and we get the exact result. We compare this exact result with the result we obtain by truncating the summation at $j = j_{\max}$. Then we discuss another approach, the variational basis approach, to approximately calculate the Bloch eigenfunctions and find out the advantages of this approximation.

Exact Bloch Eigenfunctions

Now we need to calculate the interior region Bloch eigenfunctions. In order to calculate the Bloch eigenfunctions, we need to specify some kind of boundary conditions. When R-matrix theory was first founded by Wigner and Eisenbud [5], it was formulated in a way that the interior region eigenfunctions satisfy a specific boundary conditions; the logarithmic derivative boundary conditions on the soft boundaries. The logarithmic derivative boundary condition is that the interior region eigenfunctions satisfy,

$$\frac{d}{dx}\phi = b\phi, \tag{2.30}$$

on the soft boundaries. Here b is a constant typically chosen to be zero and the set of interior region eigenfunctions are denoted by $|\phi\rangle$. We call these interior region eigenfunctions the Wigner-Eisenbud (WE) functions. Considering the soft boundary conditions at $x = L$ and hard wall boundary conditions at $x = 0$ the Bloch eigenfunctions with $b = 0$ take the form,

$$\phi_j(x) = \sqrt{\frac{2}{L}} \sin\left[(2j-1)\frac{\pi}{2L}x\right] \qquad j = 1, 2, \ldots, \tag{2.31}$$

and the Bloch eigenvalues are,

$$E_j = \frac{\pi^2}{8L^2}(2j-1)^2 \qquad j = 1, 2, \ldots \tag{2.32}$$

Note that we use the dimensionless units as explained in eq. (2.8). We also call these eigenfunctions, "the exact Bloch eigenfunctions" as they are in a closed form which perfectly satisfies the given boundary conditions.

According to eq. (2.23), we calculate the R-matrix value $R(E, L, L)$ as,

$$R^{WE}(E, L, L) = \frac{1}{2}\sum_{j}^{\text{jmax}} \frac{|\phi_j(L)\rangle \langle\phi_j(L)|}{E_j - E}. \tag{2.33}$$

Note that we have truncated the summation at $j = j_{\max}$ and we call the R matrix value, the $R^{WE}(E, L, L)$.

Exact Result

Since the exact Bloch eigenfunctions take the analytic form,(eq.2.31 and eq.2.32) for this simple case, we can perform the infinite summation as eq. (2.26), and get the exact form for the R-matrix element as,

$$R^{\text{exact}}(E, L, L) = \frac{1}{k}\tan(kL), \tag{2.34}$$

where $k = \sqrt{2E}$ according to our dimensionless units. To avoid confusion, with dimensions we define $\tilde{k} = \sqrt{\frac{2m^*\tilde{E}}{\hbar^2}}$. Note that we call this result $R^{\text{exact}}(E, L, L)$.

We plot the value of the exact R-matrix as a function of the energy in the figure (2.3).

We can see that at some energies, the R-matrix diverges. By looking at this graph and the list of eigenvalues of the interior region Bloch eigenfunctions (list of $(\frac{2j-1}{2})^2\pi^2$ which are $1.23, 11.10, 30.84$...etc), we find that these divergences occur when the scattering energy equals to one of the eigenenergies of the interior scattering region. The scattering energies which are equal to the Bloch eigenenergies (where the R-matrix diverges) are normally called the R-matrix poles. In the next section we calculate the Bloch eigenfunctions numerically with variational basis functions.

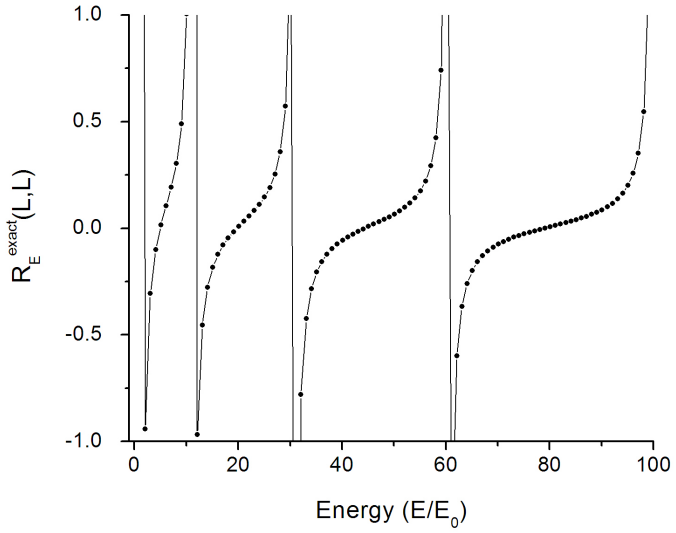

Figure 2.3: The exact R-matrix for the closed tube problem, $R^{\text{exact}}(E,L,L) = \frac{|\Psi_E(L)\rangle}{\frac{d}{dx}|\Psi_E(L)\rangle}$ as a function of the scattering energy. The R-matrix diverges at R-matrix poles. R-matrix poles are the scattering energies which equal to one of the Bloch eigenenergies of the interior region A.

Variational Approach

Here we explain the variational R-matrix theory, one of the main parts of this thesis. In the variational approach, we do not solve for the exact Bloch eigenfunctions. Instead the Bloch eigenfunctions are expanded in terms of a variational basis set. What is this variational basis set? The important thing about the variational basis functions is that they do not obey any particular conditions on the soft boundaries. They only satisfy the physical hard wall boundary conditions.

We choose the variational basis functions as,

$$\eta_a(x) = \sqrt{\frac{2}{\lambda}} \sin \frac{a\pi}{\lambda} x, \tag{2.35}$$

to expand the Bloch eigenfunctions $|\phi_j\rangle$, where λ is larger than the width of the interior region, L. Figure (2.4) shows the boundary conditions of the variational basis functions and of the logarithmic derivative (Wigner-Eisenbud) basis functions.

This figure shows that the Wigner-Eisenbud basis functions has a zero derivative where as the variational basis functions have arbitrary derivative on the boundary. Since the scattering wave function does not obey any particular condition on the boundary, the variational basis functions make a better set to expand the scattering wave function.

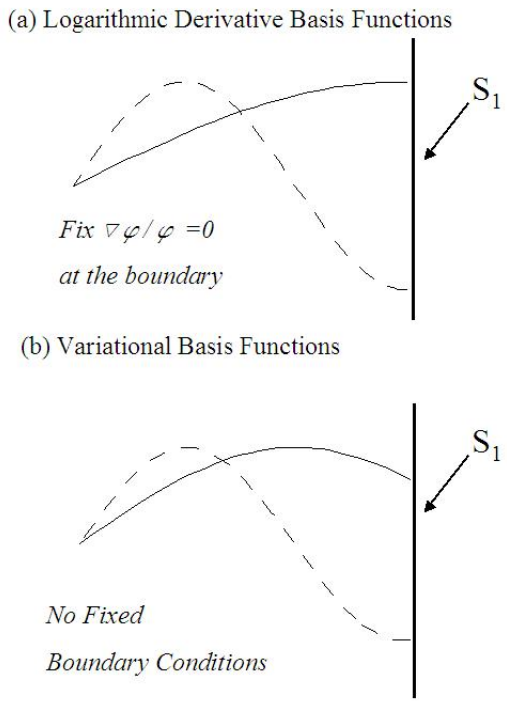

Figure 2.4: A diagram of exact WE basis functions (upper) and the variational basis functions (lower) in the interior region of the closed tube. Note that the WE wave functions have a particular boundary conditions while the variational basis functions have different values and different derivatives on the soft boundary.

This variational basis set is not orthogonal in the interior region. However we choose $\lambda > L$ so that these functions are complete inside the interior region. Since this is not an orthogonal set, we have to find the eigenfunctions of the interior region Bloch Hamiltonian with these basis functions as a generalized eigenvalue problem. The process is slower than diagonalizing the Bloch Hamiltonian with an orthogonal

basis set, however we get better solutions for the extra effort.

The Generalized Eigenvalue Problem

Below we explain the generalized eigenvalue problem that we solve to obtain the Bloch eigenfunctions in terms of the nonorthogonal variational basis function as in eq. (2.35). The Bloch Hamiltonian has the form,

$$\mathcal{H}_B = \mathcal{H}_0 + \mathcal{L}. \tag{2.36}$$

We need to find $|\phi_j\rangle$ and E_j such that,

$$\langle\phi_j|\,\mathcal{H}_B - E_j\,|\phi_j\rangle = 0. \tag{2.37}$$

We expand $|\phi_j\rangle$ in terms of the variational basis functions as,

$$\phi_j(x) = \sum_a d_{j,a}\eta_a(x). \tag{2.38}$$

Using equations (2.37) and (2.38), we get a generalized eigenvalue equation as,

$$\sum_{a,a'} \mathcal{O}^{-1}_{a,a'}\mathcal{H}_{a',a''}\ d_{j,a''} - E_j\ d_{j,a} = 0, \tag{2.39}$$

where $\mathcal{H}_{a',a''} = \langle\eta_{a'}|\,\mathcal{H}_B\,|\eta_{a''}\rangle$ and $\mathcal{O}_{a',a} = \langle\eta_{a'}|\eta_a\rangle$. This equation can be solved for the expansion coefficients $d_{j,a}$'s and the eigenvalues E_j's. With this expansion coefficients, we get the R-matrix,

$$R^{\rm var}(E,L,L) = \frac{1}{2}\sum_{j}^{\rm jmax}\sum_{a,a'} d_{j,a}d^*_{j,a'}\frac{|\eta_a(L)\rangle\,\langle\eta_{a'}(L)|}{E_j - E}. \tag{2.40}$$

Here we call the R-matrix as $R^{\rm var}(E,L,L)$.

In the next section we compare the values we obtained for the R-matrix in the three methods as explained by eq. (2.33), eq. (2.34) and eq. (2.40).

Convergence of R-matrix elements: Exact Result, Wigner-Eisenbud Approach and Variational Approach

We have discussed different methods to calculate the R-matrix element for the one-dimensional closed tube problem according to the equations 2.34 (exact result) , 2.33 (Wigner-Eisenbud result), and 2.40 (variational approach). We now calculate it as a function of the number of basis functions in the latter two cases and compare the result with the first. These answers depend upon how many basis functions we use in the calculation and we plot the result as a function of the number of basis functions used in the calculation. The result is shown in the figure (2.5).

The straight line is the exact value for the R-matrix, $R^{\text{exact}}(E, L, L)$. Since it is calculated by doing the infinite summation analytically, it does not depend on the number of basis functions. The solid dots are the $R^{\text{var}}(E, L, L)$, the value of the R-matrix calculated by the variational basis functions and the open dots are the $R^{\text{WE}}(E, L, L)$, the value of the R-matrix calculated by the Wigner-Eisenbud basis functions.

This result shows that $R^{\text{var}}(E, L, L)$ reaches the exact value with far fewer basis functions when compared to the $R^{\text{WE}}(E, L, L)$. From such results, we conclude that the variational basis functions works better in the R-matrix calculation when compared to the Wigner-Eisenbud basis. We further use these two methods to calculate the transmission coefficients in the following section.

2.3.2 Calculation of the Transmission Coefficients

In the previous section, we calculated the R-matrix elements for the closed tube problem. In this section, we calculate the transmission coefficients for the electron using the R-matrix elements.

As we have discussed, the R-matrix equation (eq.2.23) gives an expression for the scattering wave function $|\Psi_E(x)\rangle$, inside the interior region. We use that to find the transmission coefficients in the leads. The concept here is that in order to get

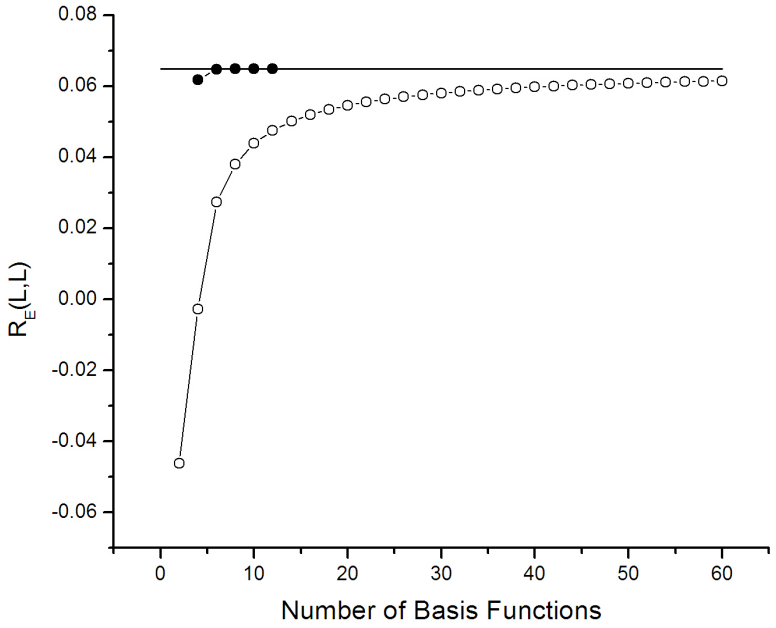

Figure 2.5: Graph of the R matrix as a function of the number of basis functions used in the calculation of electron scattering in a closed tube. We have only one soft boundary so there is only one R matrix element. In this problem R- matrix element relates to the scattering wave function as, $R(E,L,L) = \frac{\Psi}{\frac{d}{dx}\Psi}$. The value is evaluated at energy $E = 100 \times \frac{\hbar^2}{m^* a^2}$. Solid dots are the result obtained by variational basis functions and the open dots are the result obtained by using the Wigner-Eisenbud (logarithmic derivative) basis functions. The straight line is the exact result. This typical case shows that the variational basis functions achieves faster convergence when compared to the Wigner-Eisenbud basis functions.

the information in the leads, we apply the R-matrix formula on the soft boundaries which are common to both the leads and the interior region. We consider a plane wave incident from the right ($x \geq 0$) traveling to the left. There will also be a reflected wave for ($x \geq 0$) traveling to the right. Because of the hard wall at $x = 0$, there is no transmitted wave: $|\Psi_E(x)\rangle = 0$ for $x \leq 0$. We define the wave number corresponding to kinetic energy $E \geq 0$ as $k = \sqrt{2E}$.

We define the incident and reflected energy-normalized traveling waves as,

$$\omega^{(-)}(E,x) = \frac{1}{\sqrt{2\pi k}} e^{-ikx}$$
$$\omega^{(+)}(E,x) = \frac{1}{\sqrt{2\pi k}} e^{ikx}. \tag{2.41}$$

With this, we can write the scattering wave function in the leads as,

$$\begin{aligned} |\Psi_E(x)\rangle &= \omega^{-}(E,x) + \rho(E)\ \omega^{+}(E,x) \quad x \geq 0 \\ &= 0 \quad x \leq 0, \end{aligned} \tag{2.42}$$

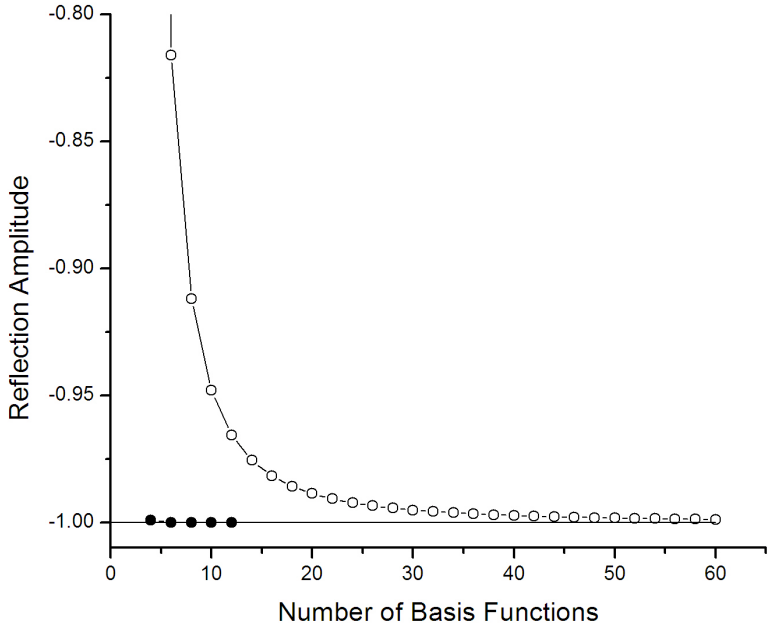

Figure 2.6: Graph of the reflection amplitude of the electron as a function of the number of basis functions used in the calculation of scattering in a closed tube as evaluated at energy $E = 100 \times \frac{\hbar^2}{m^* a^2}$. Solid dots are the result obtained by variational basis and open dots are the result obtained by using the Wigner-Eisenbud basis. The straight line is the exact result (reflection amplitude = -1). This result shows that the variational basis functions achieves faster convergence when compared to the Wigner-Eisenbud basis functions confirming the conclusion made in section (2.3.1).

where ρ is the reflection amplitude. Substituting this form of the wave function in the R-matrix equation (eq.2.23), doing some algebra, we get,

$$\rho = -e^{-2ikL}\left[\frac{1+ikR(E,L,L)}{1-ikR(E,L,L)}\right]. \tag{2.43}$$

This equation correctly implies the unit reflection coefficient ($|\rho|^2 = 1$) of electrons as we expected. Also for this problem we expect the reflection amplitude, $\rho = -1$. Note that the negative sign is for the phase change due to the reflection. We calculate this answer using the R-matrix value and compare the answers obtained by variational basis functions and the Wigner-Eisenbud basis functions. The result is shown in the figure (2.6).

This graph again shows that the reflection amplitude converges to the exact answer with a small number of basis functions, compared to the Wigner-Eisenbud basis functions confirming our conclusion in the previous section, that the variational basis functions work better than the Wigner-Eisenbud basis functions in the R-matrix calculation.

2.4 Application of the R-Matrix Theory to Electron Transmission Through an Open Tube

We learned about the R-matrix theory in devices and the advantage of using the variational RMT in the previous section. For electron scattering in a closed tube (2.3), we have only one soft boundary so that the R-matrix is a single value or a 1×1 matrix.

In this section, we simply extend the theory for electrons scattering through an open tube. We do this to demonstrate the technique in a case that is more relevant to device physics, where the R-matrix is really a matrix rather than a single number. This problem will help understanding the more complicated 2-dimensional scattering problem in chapter (3). We explain the calculation in detail only when it differs from

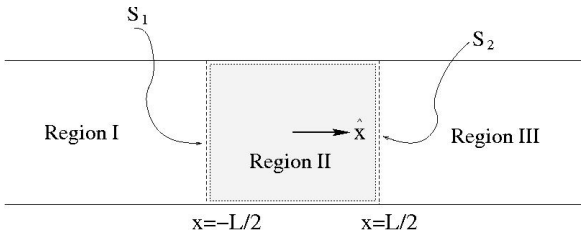

Figure 2.7: A schematic diagram of an open tube for the R-matrix theory calculation. We artificially divide the tube into three regions, regions I, II, and III. Electrons are injected from region I. Supposing that electrons undergo scattering in region II, we seek the transmission coefficient in regions I and III. The answer is known for this problem: The transmission coefficient is 0 in region I and the transmission coefficient is 1 in region III. We look at the convergence of this result as a function of number of basis functions used in calculating the R-matrix elements, in order to study the convergence.

the closed tube case, otherwise we show the results. A schematic diagram for the open tube calculation is given in the figure (2.7).

We assume an imaginary interior scattering region, $(-L/2 < x < L/2)$ as shown in the fig. (2.7). We consider the problem in three regions,I, II, and III. Region I and III are outgoing leads while region II is the interior scattering region. Electrons are injected from the region I, and undergo scattering in region II. We seek the transmission coefficient in regions I and III. Again this probelm has a straightforward answer: The electron will transmit to the region III with a transmission coefficent 1 and there is no transmission to the region I. We solve this problem with the R matrix theory to demonstrate the technique in detail.

2.4.1 Calculation of the R-matrix Elements

The interior scattering region is the shaded region in fig. (2.7). The exact Bloch eigenfunctions satisfy the boundary conditions, (eq.2.30) on the soft boundaries at

$x = \pm\frac{L}{2}$, thus take the form,

$$\begin{aligned} \phi_j &= \sqrt{\frac{1}{\lambda}} \\ &= \sqrt{\frac{2}{L}} \sin \frac{j\pi}{L} x \quad j = 1, 3, ... \\ &= \sqrt{\frac{2}{L}} \cos \frac{j\pi}{L} x \quad j = 2, 4, ... \end{aligned} \tag{2.44}$$

The exact Bloch eigenvalues for this case are,

$$E_j = \frac{j^2 \pi^2 \hbar^2}{2m^* L^2} \quad j = 1, 2, 3..... \tag{2.45}$$

According to eq. (2.26), the value of the R-matrix depends on two points in the system, s_q and s_p. In the one-dimensional open tube problem, we have two boundaries, in that s_q and s_p can be either $\pm L/2$. That is we have 4 possible R-matrix elements. In particular those are, $R(E, +L/2, +L/2)$, $R(E, +L/2, -L/2)$, $R(E, -L/2, +L/2)$ and $R(E, -L/2, -L/2)$. We use shorthand notation to denote them as, $R_E(+,+)$, $R_E(+,-)$, $R_E(-,+)$ and $R_E(-,-)$ respectively.

In the convergence study, we consider only one of these R-matrix elements, $R_E(+,+)$, which takes the explicit form,

$$R_E(+,+) = \frac{1}{2} \sum_j^{\infty} \frac{|\phi_j(L/2)\rangle \langle \phi_j(L/2)|}{E_j - E}. \tag{2.46}$$

Using the exact Bloch eigenfunctions and Bloch eigenvalues, (eq. 2.44 and 2.45), and performing the infinite summation over j analytically, $R_E(+,+)$ reduces to,

$$R_E^{\text{exact}}(+,+) = \frac{-\cot kL/2 + \tan kL/2}{2k}, \tag{2.47}$$

where $k = \sqrt{2E}$.

Convergence of R-Matrix Elements : Exact Result, Wigner-Eisenbud Result and Variational Result

We calculate $R_E^{\text{exact}}(+,+)$, $R_E^{\text{WE}}(+,+)$ and $R_E^{\text{var}}(+,+)$ as a function of the number of basis functions as shown in the graph (fig.2.8). The corresponding equations for the

case of a closed tube can be found at eq. (2.33),eq. (2.34), and eq. (2.40). We do not describe those equations in detail here.

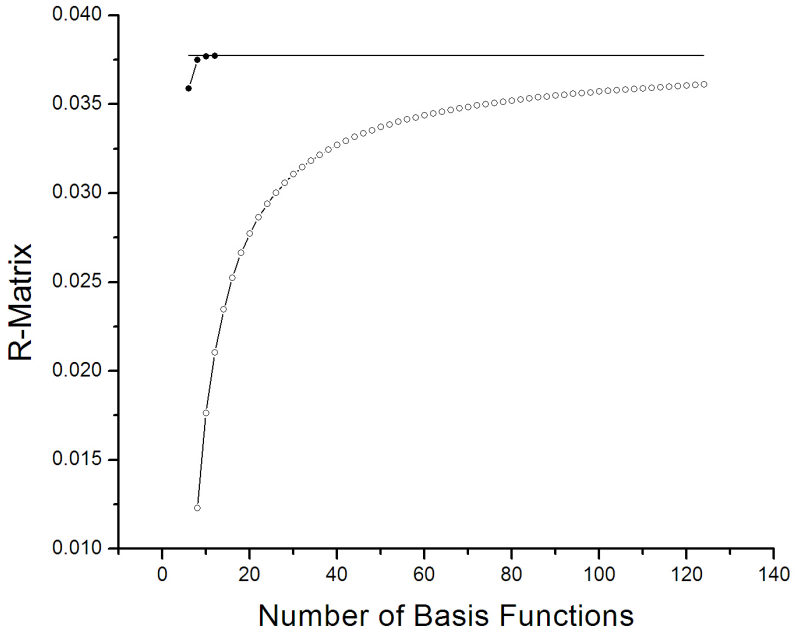

Figure 2.8: Graph of the R-matrix, $R_E(+,+)$ at energy, $E = 100 \times \frac{\hbar^2}{m^* a^2}$ as a function of the number of basis functions used in the calculation. Solid dots are the result obtained by variational basis functions, open dots are the result obtained by using the logarithmic derivative boundary conditions. This graph shows that the variational basis functions give a faster convergence in the R-matrix calculation as we concluded in the section (2.3).

This graph shows that variational basis functions give faster convergence than the Wigner-Eisenbud basis function. We further use these two types of basis functions to calculate the transmission coefficients of an electron being transmitted through the open tube.

2.4.2 Calculation of the Transmission Coefficients

In the previous section we have calculated the R-matrix elements for the open tube problem. In this section, we need to calculate the transmission coefficients for the electron using the R-matrix elements. This calculation is different from the calculation done in the closed tube problem since the open tube problem has two soft boundaries. This calculation shows how the technique changes from a spherical problem to a non -spherical problem.

We consider a plane wave incident from region I ($x \leq 0$) traveling to the right. Those electrons undergo scattering in the region II and electrons will transmit to the region III and reflect back to the region I. We define the wave number corresponding to the incident kinetic energy ($E \geq 0$) as $k = \sqrt{2E}$. We get the incident and reflected traveling waves as,

$$\begin{aligned} \omega^{+} &= \sqrt{\frac{1}{2\pi k}} e^{ikx} \\ \omega^{-} &= \sqrt{\frac{1}{2\pi k}} e^{-ikx} \end{aligned} \tag{2.48}$$

The scattering wave function in those two leads can be written as,

$$|\Psi_E\rangle = \omega^{+}(E,x) + \rho(E)\omega^{-}(E,x); \quad \text{Region I} \tag{2.49}$$

$$= \tau(E)\omega^{+}(E,x); \quad \text{Region III}, \tag{2.50}$$

where $\rho(E)$ is the reflection amplitude and $\tau(E)$ is the transmission amplitude. We expect the solution to be

$$\begin{aligned} \rho(E) &= 0 \\ \tau(E) &= 1 \end{aligned} \tag{2.51}$$

We apply the R matrix equation (eq.2.23) on the boundaries at $x = -L/2$ and $x = L/2$. The Bloch operator for this problem is,

$$\mathcal{L}_B = \frac{\partial}{\partial x}|_{x=L/2} - \frac{\partial}{\partial x}|_{x=-L/2}. \tag{2.52}$$

Notice that we get a term for the Bloch operator at each boundary. The negative sign in the second term is because at the $x = -L/2$ boundary, the perpendicular-norm points to the negative direction.

We will consider the R-matrix equation at the two boundaries, $x = -L/2$ and $x = -L/2$ as,

$$\begin{aligned}\Psi(x = -L/2) &= R_E(-,+)\frac{\partial}{\partial x}|\Psi(x = L/2)\rangle - R_E(-,-)\frac{\partial}{\partial x}|\Psi(x = -L/2)\rangle \\ \Psi(x = +L/2) &= R_E(+,+)\frac{\partial}{\partial x}|\Psi(x = L/2)\rangle - R_E(+,-)\frac{\partial}{\partial x}|\Psi(x = -L/2)\rangle\end{aligned} \tag{2.53}$$

Now we write the scattering wave function $|\Psi\rangle$ and its derivative using eq. (2.49).

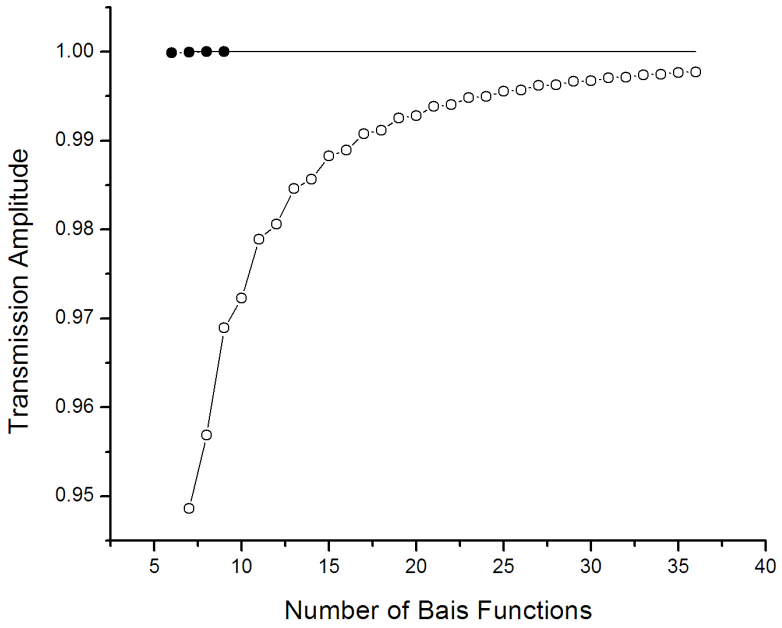

Figure 2.9: A graph of transmission amplitude of the electron as a function of the number of basis functions used in the calculation in the open tube problem as evaluated at the energy $E = 100 \times \frac{\hbar^2}{m^* a^2}$. Solid dots are the result obtained by variational basis functions and the open dots are the result obtained by WE basis functions. The straight line is the exact result.

This will lead to two equations and two unknowns which can be written in the matrix form as,

$$\begin{pmatrix} ikR_E(+,+)-1 & ikR_E(+,-) \\ ikR_E(-,+) & ikR_E(+,+)-1 \end{pmatrix} \begin{pmatrix} \tau \\ \rho \end{pmatrix} = \begin{pmatrix} ikR_E(+,-)e^{-ikL} \\ (1+ikR_E(+,+))e^{-ikL} \end{pmatrix}, \tag{2.54}$$

which can be solved for the unknown scattering amplitudes τ and ρ. Note the difference of eq. (2.54) from the eq. (2.43). When we have more boundaries, the equations get a little complicated. However, the concepts remain the same. We calculate ρ and τ using the R-matrix elements calculated from different methods. The values obtained for the transmission coefficient, $|\rho|^2$ is plotted in the figure (2.9). The result again confirm our conclusion that the variational approach is better in the R-matrix calculation.

In the next section we investigate the reasons for the faster convergence when using the variational basis functions.

2.5 Convergence Studies of the Variational R-Matrix Theory

According to the results obtained for the electron scattering in a closed tube (sec.2.3) and in an open tube (sec.2.4), we found that the variational basis functions give a faster convergence. In this section, we investigate possible reasons for this faster convergence.

When we calculate Bloch eigenfunctions we have to truncate the Hilbert space. We first diagonalize the Bloch Hamiltonian in $N_{\max}$, the number of basis functions. In the Wigner-Eisenbud calculation, the Bloch Hamiltonian is diagonal since WE basis functions are the solutions of that Hamiltonian. However, the Bloch Hamiltonian is a full matrix for the variational calculation.

When we do the summation over eigenfunctions as in eq. (2.26), we do the sum-

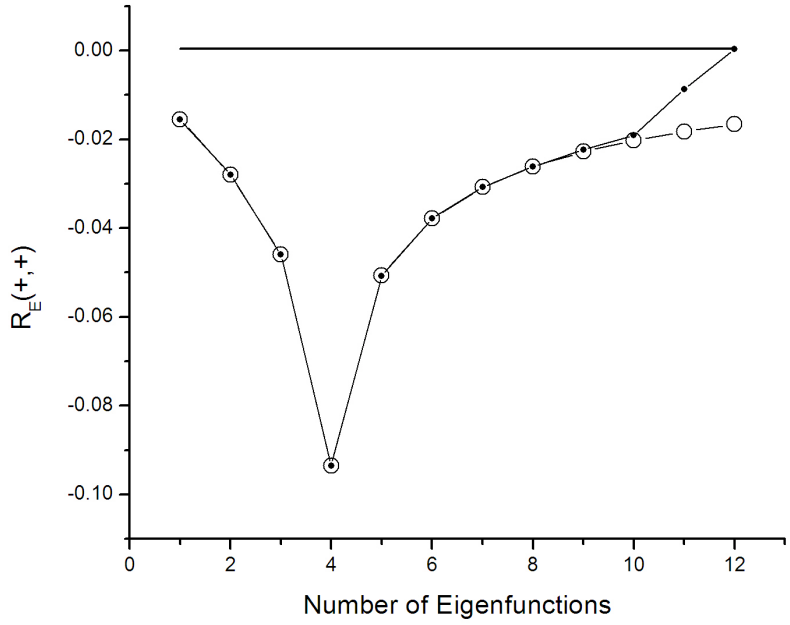

Figure 2.10: The value of the R matrix, $R_E(+,+)$ as a function of the number of eigenfunctions used in the summations. The straight line is the exact result. Solid dots are the result obtained using the variational basis functions and the open dots are the result obtained using the WE functions. In this calculation, the Hilbert space consists of only 12 basis functions and the electron scattering energy is 100 in dimensionless units.

mation as a function of the quantum number j. The result is plotted in fig. (2.10). In this result, we have diagonalized the Bloch Hamiltonian in 12 basis functions. For the plotted result, (fig.2.10) the electron scattering energy $E = 100$ in the dimensionless units (eq.2.8). The solid dots are the result obtained in the variational calculation and the open dots are the result obtained in the Wigner-Eisenbud calculation.

The graph (fig.2.10) shows some interesting behavior. There are two main features one observes in this graph.

- There is a significant dip when there are 4 basis functions included in the summation. This feature is common to both the variational approach and the Wigner-Eisenbud approach.

- There is a non-uniform behavior in the convergence in the variational basis function calculations; The answer suddenly jumps to the exact value when we include the last eigenfunctions in the summation.

The first feature, a dip in the convergence result, can be explained as follows. We will consider the first few eigenvalues of the interior region (Table 2.1).

The Quantum Number j	Eigenvalue (in Dimensionless Units)
1	0
2	4.93
3	19.73
4	44.41
5	78.96
6	123.37
7	177.65
8	241.80

Table 2.1: The eigen-energies E_j of the interior scattering region for different quantum number j for the open tube problem.

The scattering energy for our calculation is $E = 100$. According to the equation (2.26), the largest contributions to the R-matrix come from those eigenfunctions which have the eigenvalues close to the scattering energy. In this particular calculation, the scattering energy is close to the eigenenergy of the 5th and the 6th eigenfunctions. That is why the result start to converge to the exact value only after we include the 5th eigenstate.

The second feature is that the convergence is not uniform: the last eigenfunctions in the summation put the value at the exact answer. One might conclude that this feature is unique to the number of basis function we used in this calculation. We find that this is not a feature that depends on the number of basis functions used in the calculation. In order to demonstrate this statement, we show a similar graph (in fig. 2.11) which was obtained using 10 basis functions in the calculation.

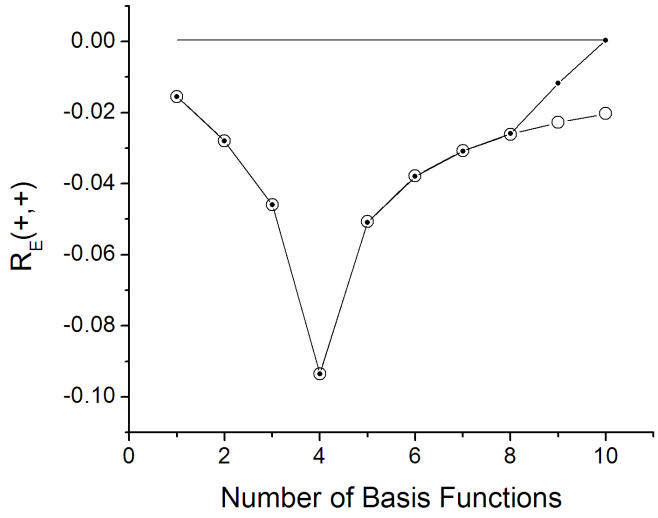

Figure 2.11: The value of the R matrix, $R_E(+,+)$ as a function of the number of basis functions used in the summations. The straight line is the exact result. Solid dots are the result obtained using the variational basis functions and the open dots are the result obtained using the WE functions. In this calculation, the Hilbert space consists of only **10** basis functions and the electron scattering energy is 100 in dimensionless units. The features are the same as the features we observed in the graph (fig.2.10) confirming that this feature is independent of the number of basis functions.

This graph shows the same dip at the 4th eigenenergy and the same kind of nonuniform behavior as we observed with 12 basis functions. It demonstrates that this behavior is common to all the variational calculations, the last elements of the basis put the value exactly at the right answer. This nonuniform feature of the convergence does not have a deep mathematical explanation yet.

According to the above results, a reasonable question to ask is if this faster convergence of the variational RMT occurs only at particular energies. We calculate the R-matrix, $R_E(+,+)$ for the open tube by the two methods as a function of energy. We use 10 basis functions in this study. The figure (2.12) is a plot of the relative error, $(R_E^{\text{numeric}} - R_E^{\text{exact}})/R_E^{\text{exact}}$ as a function of the energy, E. The solids dots are the values obtained for the variational calculation and the open dots are the values

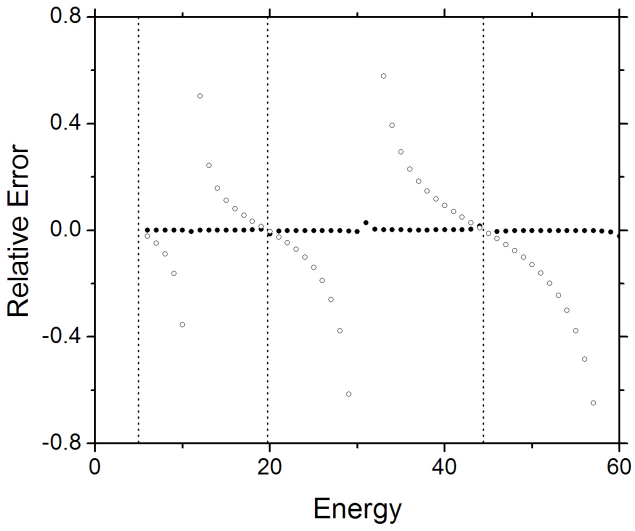

Figure 2.12: Variation of the relative error of $R_E(+,+)$ as a function of scattering energy for both the variational and the Wigner-Eisenbud calculation. Solid dots are for the variational calculation and the open dots are for the WE calculation. The dotted straight lines are the Bloch eigen energies.

obtained in the Wigner-Eisenbud calculation. The dotted straight lines are the Bloch eigenenergies. This result shows that the variational calculation has a small error at all the energies, the WE calculation has a large error at most energies, and the WE answer is exact when the scattering energy, E equals to one of the Bloch eigenenergies. We explain this as follows. The failure of the Wigner-Eisenbud method is that those basis functions have a zero slope where as the scattering wave function does not have any particular condition at the boundaries. However if you think about the one-dimensional R-matrix equation (2.23) the R-matrix is inversely proportional to the logarithmic derivative of the scattering wave function. So Wigner-Eisenbud basis functions do satisfy the boundary conditions for the scattering wave function when the scattering energy equals to the Bloch eigenenergy. That is why we get converged results using the WE basis functions only when the scattering energy equals to one of the Bloch eigenenergies.

2.6 Conclusion

To conclude this chapter,

- We have improved the existing R-matrix theory calculation in device physics by using the variational approach to achieve faster convergence,
- We have applied this variational R-matrix technique to electron scattering in one dimensional problems and demonstrated that the variational technique gives a faster convergence
- We observed the non-uniform behavior of this faster convergence of the variational R-matrix theory, however a deep mathematical explanation for this non-uniform convergence is not yet clear.

Chapter 3

2-Dimensional R Matrix Formula

3.1 Introduction

In the previous chapter, (2), we discussed the basic concepts of the R-matrix theory. We applied the technique to one-dimensional devices and demonstrated the advantage of using the variational basis functions in the R-matrix calculation.

We also discussed the possibility of making different structures in a two-dimensional system. Therefore it is important to know how to apply the variational RMT in a two-dimensional device with many leads. As we learned from the one-dimensional calculation, (sec.2.3 and sec.2.4), when the system geometry becomes complicated the R-matrix gets larger and the calculation becomes little involved. Thus it is very important to have a generalized formula with a systematic notation.

According to eq. (2.23), the R-matrix elements depend on two points, s_q and s_p on the soft boundaries. In the one-dimensional case, the soft boundaries are points. These soft boundaries are surfaces in two-dimensional devices. In applications to atomic and molecular systems, where the soft boundaries are always a spherical surface, this is a minor complication. Unlike the atomic and molecular problems, device problems will typically have several leads. Thus the boundary of the interior region consists of several segments of surfaces some of which are impenetrable walls (hard

walls) and others open to leads (soft boundaries). We symbolically represent them as

$$\mathcal{S} = \mathcal{S}_w + \mathcal{S}_o, \tag{3.1}$$

where $\mathcal{S}_w$ are the hard walls and $\mathcal{S}_o$ are the open or soft boundaries. There are number of soft boundaries depending on the number of leads that,

$$\mathcal{S}_o = \sum_{p=1}^{N_p} \mathcal{S}_p, \tag{3.2}$$

where p denotes the lead.

There is another complication in the two-dimensional problem. The two-dimensional leads add an extra degree of freedom since the electron can occupy in different subbands depending on the total energy. During the scattering, electron can change its subband index. In atomic physics such a transition would be called "inelastic" even though in our case the total energy is conserved. The electron can gain or lose longitudinal kinetic energy by changing the subband state.

Due to this complication of the problem, it is necessary to devise a general formula which can be used for devices with different geometries. Though the concept is the same as in the one-dimensional theory, more systematic notation is required when adding extra degrees of freedom.

When we consider the transmission coefficients of electrons from one lead to another, how many fundamental quantities do we need to calculate? To answer that question, we need to define the incoming state of electrons. How many quantum numbers are required to define the state? How many of these quantum numbers can be changed due to the scattering? We need to calculate the probability of each of these scattering events. The matrix which contains all the information of the probabilities is called the scattering matrix. In this chapter, we generate a formula to calculate the scattering matrix for a two-dimensional device with an application to the scattering of electrons in a T-junction device (fig.3.1). Our formula is generic that it can be used to a device with many number of leads. We discuss the application of this formula to

a plus junction device (fig.3.6) in section (3.4). Finally we discuss the convergence of the 2-dimensional RMT with the T-junction results.

3.2 R-Matrix Formula for a T-Junction Device

We consider electrons traveling in a T-shaped device. Electrons are injected from the lead 1 (input lead) and scattered in the interior region. We seek the transmission coefficients in the lead 1 (reflection), lead 2 (sidearm) and the lead 3 (forward lead).

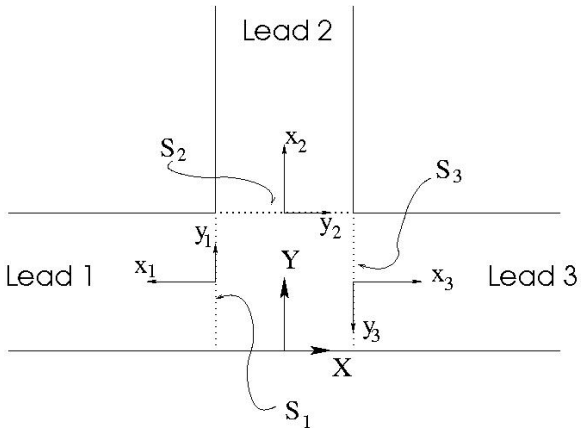

Figure 3.1: A schematic diagram of a T-junction device for the two-dimensional R-matrix formula calculation. Electrons are injected from the lead 1. We seek the transmission amplitudes in lead 1 (reflection), lead 2 and the lead 3.

First we define some notations to explain the device geometry and the electron state. We define a local coordinate system for each lead and we assume that each lead has a Cartesian symmetry (fig.3.1). Each of these coordinate system is explained by two orthogonal coordinates (x_p, y_p) where x_p is the longitudinal coordinate and y_p is the transverse coordinate. We choose $x_p = 0$ where the leads meet the interior region (on the soft boundaries). Another set of coordinates is chosen for the interior scattering region. For the T-junction device, we choose the (x, y) coordinate system for the interior region as shown in the figure.

As explained in the previous chapter, the idea of the RMT is to divide the system into parts, the outgoing leads and the interior scattering region. We solve the Schrodinger equation in these two parts and match them on the soft boundaries to calculate the transmission coefficients. In the following sections we consider these two types of solutions and explain how to calculate the scattering matrix.

3.2.1 Lead Solution

In general there are several leads in the device. We denote the leads by the index $p = 1, 2, \ldots, N$ where N is the total number of leads. We denote the lead, where the electrons are injected from, as $p = p_0$. For the present problem, we consider the electrons injected from the lead 1 that $p_0 = 1$ and there are 3 leads that $N = 3$. Each of these p^{th} leads has transverse quantum channels, $n_p = 1, 2, \ldots$. We assume that the potential $V = 0$ inside the device, although that is not essential to the calculation. The hard walls confine electrons to the system though the exact confining potential in an experimental device may be less abrupt. The potential energy in the longitudinal direction is a constant which we choose to be zero. Now the longitudinal wave function in the leads are traveling waves whereas the transverse wave functions are infinite well wave functions.

Depending on the energy of the incoming electron, these transverse channels will be open (current carrying) or closed (evanescent) states. This can be determined by the energy consideration as follows. The longitudinal and the transverse energies of the electron in lead p can be obtained by the relation,

$$E = \epsilon_{p,n_p} + E_{p,n_p}, \tag{3.3}$$

where E is the total energy, ϵ_{p,n_p} is the transverse energy and E_{p,n_p} is the longitudinal energy of the n_p^{th} subband. The wave vector of the electron occupy in the n_p^{th} subband can be calculated by,

$$E_{p,n_p} = \frac{k_{p,n_p}^2}{2}. \tag{3.4}$$

Note that we are using the dimensionless units that all the lengths are measured by a characteristic length of the system which we choose to be the width of the lead where the electrons are injected from, w_{p_0}. The energy is scaled by $\hbar^2/m^* w_{p_0}^2$ thus the energy of the n_p^{th} subband is given by,

$$\epsilon_{p,n_p} = \frac{\pi^2 n_p^2}{2w_p^2}, \tag{3.5}$$

where w_p is the width of the pth lead in terms of w_{p_0}. For the open channels the wave vector, k_{p,n_p} is real and for the closed channels, the wave vector is imaginary. For the real wave vectors, if k_{p,n_p} is positive (+), it is a scattering electron (traveling away from the interior region) and if k_{p,n_p} is negative (−), it is an incident electron (traveling towards the scattering region). We need three quantum numbers to specify an electron in a lead which we will denote by (p, n_p, k_{p,n_p}). With these quantum numbers, we can write the lead eigenfunctions in the qth lead as,

$$\left|\eta_{p,n_p}(x_p, y_p)\right\rangle = \left|\chi_{p,n_p}(y_p)\right\rangle e^{ik_{p,n_p}x_p}. \tag{3.6}$$

Here $\left|\chi_{p,n_p}(y_p)\right\rangle$ is the transverse wave function of the n_p^{th} subband which takes the form,

$$\left|\chi_{p,n_p}(y_p)\right\rangle = \sqrt{\frac{2}{w_p}} \sin \frac{n_p \pi}{w_p} y_p. \tag{3.7}$$

With the lead eigenfunctions, we can define the asymptotic behavior of the electron. The asymptotic states are defined at a position sufficiently far from the boundary between the lead and the scattering region that all the evanescent waves in the lead have effectively decayed to zero. These asymptotic states carry all the information about the scattering state.

We can expand the asymptotic form of the scattering wave function in the qth lead as,

$$\left|\Psi_{E,n_{p_0}}^{q,p_0}\right\rangle = \left|\chi_{q,n_q}(y_q)\right\rangle e^{-ik_{q,n_q}x_q}\delta_{q,p_0}\delta_{n_q,n_{p_0}} + \sum_{n_q}^{N_{open}^q(E)} \tau_{n_q,n_{p_0}}^{q,p_0} \left|\chi_{q,n_q}(y_q)\right\rangle e^{ik_{q,n_q}x_q}. \tag{3.8}$$

This is the asymptotic state of the wave function in the qth lead for an electron injected to the device from the $n_{p_0}^{th}$ subband in the p_0^{th} lead. The first term in this equation is the incident electron wave function. The sum in the second term contains the scattering wave functions. At the scattering energy E, there are $N_{open}^{q}(E)$ number of open channels in the qth lead. Our goal is to calculate the scattering amplitudes, $\tau_{n_q,n_{p_0}}^{q,p_0}$ which is used to calculate the transmission coefficients. These transmission coefficients make the scattering matrix of the system. It should be noted that $|\tau_{n_q,n_{p_0}}^{q,p_0}|^2$ does not give the transmission coefficient since we have not normalized the incident electron wave to unit flux. We calculate the transmission coefficient from the scattering amplitudes $\tau_{n_q,n_{p_0}}^{q,p_0}$ as,

$$\mathcal{T}_{n_q,n_{p_0}}^{q,p_0} = \frac{k_{q,n_q}}{k_{p_0,n_{p_0}}} |\tau_{n_q,n_{p_0}}^{q,p_0}|^2, \tag{3.9}$$

where the denominator is proportional to the incoming flux and the numerator is proportional to the scattering flux. The proportionality constants in the numerator and the denominator are equal to each other and cancel from the equation. The quantity $\mathcal{T}_{n_q,n_{p_0}}^{q,p_0}$ is the probability that the electron from the $n_{p_0}^{th}$ subband of the p_0^{th} lead to transmit to the n_q^{th} subband of the qth lead. So the elements of the scattering matrix are,

$$\mathcal{S}_{n_q,n_{p_0}}^{q,p_0} = \sqrt{\mathcal{T}_{n_q,n_{p_0}}^{q,p_0}}. \tag{3.10}$$

Since each element of the τ matrix in equation (3.8) corresponds to an open channel, the dimension of the $\mathcal{S}$ matrix is determined by the total number of open subbands in all the leads at energy E,

$$N_{open}(E) = \sum_{p=1}^{N} N_{open}^{p}(E). \tag{3.11}$$

We calculate the number of open channels in the pth lead using the condition, the wave vector k_{p,n_p} has to be real by using the equations (3.3), (3.4) and (3.5) as,

$$N_{\text{open}}^{p}(E) = \text{Integer Part} \left(\sqrt{2E \frac{w_p^2}{\pi^2}} \right) \tag{3.12}$$

In equation (3.8), we have a finite number of basis functions. However, when we do the expansion we should include an infinite number of transverse functions which means the dimension of the τ matrix is infinite. However, for practical purposes, we truncate the summation at a finite value, $N_{\max}$, so the τ matrix is finite. The $\mathcal{S}$ matrix is a $N_{\text{open}} \times N_{\text{open}}$ subset of the τ matrix. Even though all the elements in the τ matrix do not have a physical meaning, the elements of the $\mathcal{S}$ matrix gives the transmission coefficients of the system. In this calculation, one should use enough basis functions to achieve convergence to a desired precision and get only the open channels to calculate the physical $\mathcal{S}$ matrix. This issue is addressed in detail in the implementation section (3.2.3).

3.2.2 R-Matrix Formula and the Interior Region Problem

We start with the R-matrix equation that we developed in the previous chapter (eq2.23),

$$\left|\Psi^{q,p_0}_{E,n_{p_0}}(x_q y_q)\right\rangle = \sum_j \frac{|\phi_j(x_q,y_q)\rangle \langle\phi_j(x_p,y_p)|}{E_j - E}\mathcal{L}_B \left|\Psi^{q,p_0}_{E,n_{p_0}}(x_p y_p)\right\rangle . \tag{3.13}$$

The notation remains the same as in the one-dimensional formula (eq.2.23), however now we have two coordinates to describe the system. Here the $|\phi_j(x,y)\rangle$, the Bloch eigenfunctions are solutions to the equation,

$$\mathcal{H}_B \left|\phi_j(x,y)\right\rangle = E_j \left|\phi_j(x,y)\right\rangle , \tag{3.14}$$

where the Bloch Hamiltonian, $\mathcal{H}_B = -\frac{1}{2}(\nabla_x^2 + \nabla_y^2) + \mathcal{L}_B$.
First we have to identify the Bloch operator, $\mathcal{L}_B$ of the system. In the T-junction device we have three boundaries which we denote as $\mathcal{S}_1$, $\mathcal{S}_2$ and $\mathcal{S}_3$. For the T-junction device, $w_1 = w_3$. Following the equation (2.16), we can write the Bloch operator for this system as,

$$\mathcal{L}_B(x,y) = \frac{1}{2}\left[-\delta(x+\frac{w_2}{2})\frac{\partial}{\partial x} + \delta(x-\frac{w_2}{2})\frac{\partial}{\partial x} + \delta(y-w_1)\frac{\partial}{\partial y}\right] . \tag{3.15}$$

The interior region Bloch Hamiltonian $\mathcal{H}_B$ is separable in x and y coordinates and $|\phi_j(x,y)\rangle$ takes an analytic form. We discuss the form of these Bloch eigenfunctions in the implementation section (3.2.3). Now the scattering wave function in the interior region relates to the R matrix as,

$$\left|\Psi^{q,p_0}_{E,n_{p_0}}(x_q,y_q)\right\rangle = \sum_p R(E;x_q,y_q;x_p,y_p)\nabla\left|\Psi^{q,p_0}_{E,n_{p_0}}(x_p,y_p)\right\rangle. \tag{3.16}$$

The R-matrix is,

$$R(E;x_q,y_q;x_p,y_p) = \frac{1}{2}\sum_j \frac{|\phi_j(x_q,y_q)\rangle\langle\phi_j(x_p,y_p)|}{E_j - E}. \tag{3.17}$$

This equation is valid only for the interior scattering region. The point $s_q = (x_q, y_q)$ can be any where inside the scattering region and the point $s_p = (x_p, y_p)$ lies on the boundaries of the interior region as it is forced by the Bloch operator.

We need to determine the elements of the scattering matrix (scattering amplitudes, $\tau^{q,p_0}_{n_q,n_{p_0}}$) in the leads using the equation (3.16). We use eq. (3.16) to write down the scattering wave function on the boundary of the interior region. That is, we choose s_q to lie on a soft boundary which is common to both the qth lead and the interior scattering region where the scattering wave function $\left|\Psi^{q,p_0}_{E,n_{p_0}}\right\rangle$ can also be written as eq. (3.8).

On all the soft boundaries the value of the longitudinal coordinate $x_q = 0$. This simplifies the R-matrix equation as,

$$\left|\Psi^{q,p_0}_{E,n_{p_0}}(x_q=0,y_q)\right\rangle = \sum_p R(E;x_q=0,y_q;x_p=0,y_p)\nabla\left|\Psi^{q,p_0}_{E,n_{p_0}}(x_p=0,y_p)\right\rangle, \tag{3.18}$$

where R-matrix is given by,

$$R(E;x_q=0,y_q;x_p=0,y_p) = \frac{1}{2}\sum_j \frac{|\phi_j(x_q=0,y_q\rangle\langle\phi_j(x_p=0,y_p|}{E_j - E}. \tag{3.19}$$

On the soft boundaries, the expansion of the scattering wave function (eq.3.8) reduces to,

$$\left|\Psi^{q,p_0}_{E,np_0}(x_q=0,y_q)\right\rangle = \left|\chi_{q,n_q}(y_q)\right\rangle \delta_{q,p_0}\delta_{n_q,n_{p_0}} + \sum_{n_q}^{N^q} \tau^{q,p_0}_{n_q,n_{p_0}} \left|\chi_{q,n_q}(y_q)\right\rangle . \tag{3.20}$$

In this case the summation runs from $n_q = 1$ to N_q. As we have discussed earlier, only the open channels will contribute to the $\mathcal{S}$ matrix, however we include a number of evanescent channels as required for numerical convergence.

Note that our choice of coordinates is facilitated by the fact that, on the soft boundaries where we apply the R-matrix equation, the longitudinal coordinate, $x_q = 0$, hence all the complex harmonic wave factors disappear from the equation.

At the boundary s_q, the normal derivative of the scattering wave function is,

$$\nabla \left|\Psi^{q,p_0}_{E,n_{p_0}}(x_q=0,y_q)\right\rangle = -ik_{q,n_q} \left|\chi_{q,n_q}(y_q)\right\rangle \delta_{q,p_0}\delta_{n_q,n_{p_0}} + \sum_{n_q=1}^{N_q} i \;\; k_{q,n_q}\tau^{q,p_0}_{n_q,n_{p_0}} \left|\chi_{q,n_q}(y_q)\right\rangle . \tag{3.21}$$

Now we can plug this form of the scattering wave function (eq.3.20) and its normal derivative (eq.3.21) in the R-matrix equation (eq.3.18). This was the same in the one-dimensional case. However in the two-dimensional system, since we have the transverse degree of freedom, s_q is not a value on a particular boundary but a function of the transverse coordinate y_q. To overcome this problem, we project the scattering wave function and the interior region eigenfunctions on to the transverse state vector $\left|\chi_{q,n_q}(y_q)\right\rangle$ in the particular lead, q. We write the R matrix in terms of the transverse state vector, $\left|\chi_{q,n_q}(y_q)\right\rangle$.

$$R(E;x_q=0,y_q;x_p=0,y_p) = \frac{1}{2}\sum_j \sum_{n_q} \sum_{n_p} \gamma_{j,q,n_q}\gamma^{\star}_{j,p,n_p} \frac{\left|\chi_{q,n_q}(y_q)\right\rangle \left\langle\chi_{p,n_p}(y_p)\right|}{E_j - E}, \tag{3.22}$$

where,

$$\gamma_{j,q,n_q} = \left\langle \phi_j(x,y) \left|\chi_{q,n_q}(y_q)\right\rangle \right. . \tag{3.23}$$

We project the scattering wave function and its derivative on to the transverse state vector as,

$$\left\langle\chi_{q,n_q}(y_q)\right| \left|\Psi^{q,p_0}_{E,n_{p_0}}(x_q=0,y_q)\right\rangle = \delta_{q,p_0}\delta_{n_q,n_{p_0}} + \tau^{q,p_0}_{n_q,n_{p_0}}, \tag{3.24}$$

and,

$$\left\langle \chi_{q,n_q}(y_q) \left| \nabla \Psi^{q,p_0}_{E,n_{p_0}} \right\rangle = -ik_{q,n_q}\delta_{q,p_0}\delta_{n_q,n_{p_0}} + ik_{q,n_q}\tau^{q,p_0}_{n_q,n_{p_0}} \right. \tag{3.25}$$

We can write the scattering wave function on the qth boundary with the projected R matrix (eq.3.22) as,

$$\left|\Psi^{q,p_0}_{E,n_{p_0}}(x_q=0,y_q)\right\rangle = \sum_j \sum_{p,n_p} \sum_{n_q} \frac{1}{2}\gamma_{j,q,n_q}\gamma^{\star}_{j,p,n_p} \frac{\left|\chi_{q,n_q}(y_q)\right\rangle \left\langle \chi_{p,n_p}(y_p)\right|}{E_j - E} \nabla \left|\Psi^{p,p_0}_{E,n_{p_0}}(x_p=0,y_p)\right\rangle . \tag{3.26}$$

This can be projected on to the transverse state vector as,

$$\left\langle \chi_{q,n_q}(y_q) \left|\Psi^{q,p_0}_{E,n_{p_0}}(x_q=0,y_q)\right\rangle = \sum_j \sum_{p,n_p} \frac{1}{2}\frac{\gamma_{j,q,n_q}\gamma^{\star}_{j,p,n_p}}{E_j - E} \left\langle \chi_{p,n_p}(y_p)\right| \nabla \left|\Psi^{p,p_0}_{E,n_{p_0}}(x_p=0,y_p)\right\rangle . \right. \tag{3.27}$$

Plugging the projection of the scattering wave function and its derivative in the equation (3.27) we get,

$$\delta_{q,p_0}\delta_{n_q,n_{p_0}} + \tau^{q,p_0}_{n_q,n_{p_0}} = \sum_j \sum_{p,n_p} \frac{1}{2}\frac{\gamma_{j,q,n_q}\gamma^{\star}_{j,p,n_p}}{E_j - E} \left(-ik_{p,n_p}\delta_{p,p_0}\delta_{n_p,n_{p_0}} + ik_{p,n_p}\tau^{p,p_0}_{n_p,n_{p_0}}\right) \tag{3.28}$$

We write this equation as,

$$\delta_{q,p_0}\delta_{n_q,n_{p_0}} + \tau^{q,p_0}_{n_q,n_{p_0}} = \sum_{p,n_p} \mathcal{M}_{q,n_q,p,n_p} \left(-ik_{p,n_p}\delta_{p,p_0}\delta_{n_p,n_{p_0}} + ik_{p,n_p}\tau^{p,p_0}_{n_p,n_{p_0}}\right), \tag{3.29}$$

where,

$$\mathcal{M} = \sum_j \frac{1}{2}\frac{\gamma_{j,q,n_q}\gamma^{\star}_{j,p,n_p}}{E_j - E}. \tag{3.30}$$

Equation (3.29) gives a set of linear equations which can be solved for the unknown scattering amplitudes, $\tau^{q,p_0}_{n_q,n_{p_0}}$. There are different ways to calculate the elements of $\mathcal{M}$ matrix. We can follow the conventional R-matrix theory or we can use the variational R-matrix theory. We discuss these two methods with the implementation to the T-junction device. After explaining the variational and conventional R-matrix theory using the T-junction device we show the results and discuss the faster convergence of the variational R-matrix theory.

Note that even though we use the T-junction to explain some of the details of the above calculation, the equation (3.29) does not have any notation specific to the T-junction device. That is the equation (3.29) can be used to calculate the scattering amplitudes of electron in a device with many leads. In section (3.4), we use the same equation to calculate the transmission coefficients of electrons traveling in a plus-junction device.

3.2.3 Implementation of the Device R-Matrix Formula for a T Junction Device

In order to calculate the scattering amplitudes, $\tau^{q,p_0}_{n_q,n_{p_0}}$, we need to simultaneously solve the set of equations given by eq. (3.29). It requires the quantities γ_{j,p,n_p} for each of the pth leads as defined by equation (3.23). Those are the projection integrals of the Bloch eigenfunctions, $|\phi_j\rangle$ at the boundary p on to the transverse state vector, $\left|\chi_{p,n_p}\right\rangle$. We need to find out the Bloch eigenfunctions and then do the projection. The Bloch operator $\mathcal{L}$ is given by eq. (3.15). The Bloch eigenfunctions are the solutions to the equation (3.14). The Bloch Hamiltonian is separable in x and y coordinates that we need to solve for,

$$\begin{aligned} \mathcal{H}_{B_x} |\phi^x_n(x)\rangle &= E_n |\phi^x_n(x)\rangle \\ \mathcal{H}_{B_y} |\phi^y_m(y)\rangle &= E_m |\phi^y_m(y)\rangle \end{aligned} \tag{3.31}$$

In the following three subsections we explain different approaches to calculate these γ_{j,p,n_p} values.

Bloch Eigenfunctions from Wigner-Eisenbud Method

For the T-junction problem Bloch eigenfunctions take an analytic form. The x and y dependent Hamiltonians are similar to the closed tube (2.3) and the open tube (2.4) problems we discussed in chapter (2). We here repeat the form of these functions.

The x dependent Bloch eigenfunctions take the form,

$$\begin{aligned} |\phi_n^x(x)\rangle &= \sqrt{\frac{1}{w_2}} \\ &= \sqrt{\frac{2}{w_2}} \sin \frac{n\pi}{w_2} x \quad for \quad n = 1, 3, \ldots \qquad (3.32) \\ &= \sqrt{\frac{2}{w_2}} \cos \frac{n\pi}{w_2} x \quad for \quad n = 2, 4, \ldots, \end{aligned}$$

(3.33)

with the eigenvalues,

$$E_n = \frac{n^2\pi^2}{2w_2^2} \quad n = 0, 1, 2, 3 \ldots . \qquad (3.34)$$

Here w_2 is the width of the lead 2 (sidearm). Now the y dependent Bloch eigenfunctions take the form,

$$\phi_m^y(y) = \sqrt{\frac{2}{w_1}} \sin \frac{(2m-1)^2\pi}{2w_1} y, \qquad (3.35)$$

with the eigenvalues,

$$E_m = \frac{(2m-1)^2\pi^2}{8w_1^2}, \qquad (3.36)$$

where w_1 is the width if the lead 1. The total eigenfunctions are $|\phi_{n,m}(x,y)\rangle = |\phi_n^x(x)\rangle \times |\phi_m^y(y)\rangle$ with the eigenvalues $E_{n,m} = E_n + E_m$. With these values, we calculate the projection of the Bloch eigenfunctions to the transverse state vectors γ_{j,p,n_p}.

Variational R-matrix Theory

As explained in the previous chapter, we use a set of variational basis functions to expand the Bloch eigenfunctions. That is we write,

$$|\phi_{n,m}(x,y)\rangle = \sum_{a,b} d_{n,m,a,b} \, |\eta_a(x)\rangle \, |\zeta_b(y)\rangle \, , \qquad (3.37)$$

which is analogous to the one-dimensional equation (2.38). We solve the generalized eigenvalue problem (eq.2.39) to find out the expansion coefficients, $d_{n,m,a,b}$. Then we

can calculate the required quantities γ_{j,p,n_p}. We use a variational functions as follows. The x dependent functions take the form,

$$\begin{aligned} |\eta_a^x(x)\rangle &= \sqrt{\frac{1}{\lambda_x}} \\ &= \sqrt{\frac{2}{\lambda_x}} \sin \frac{a\pi}{\lambda_x} x \quad \text{for} \quad a = 1, 3, \ldots \qquad (3.38) \\ &= \sqrt{\frac{2}{\lambda_x}} \cos \frac{a\pi}{\lambda_x} x \quad \text{for} \quad a = 2, 4, \ldots, \end{aligned}$$

(3.39)

And the y dependent basis functions, $\zeta_b(y)$ takes the form,

$$\zeta_b(y) = \sqrt{\frac{2}{\lambda_y}} \sin \frac{(2b-1)\pi}{2\lambda_y} y. \qquad (3.40)$$

The Bloch eigenfunctions obtain from this method are approximate solutions to the equation (3.14). We also calculate the corresponding approximate eigenenergies.

An Alternate Approach

Here we present an alternative approach to calculate the R-matrix elements. We start with the equation (2.19),

$$\left|\Psi_{E,n_{p_0}}(x,y)\right\rangle = \mathcal{G}_B \mathcal{L} \left|\Psi_{E,n_{p_0}}(x,y)\right\rangle, \qquad (3.41)$$

where we have defined,

$$\mathcal{G}_B = (\mathcal{H} + \mathcal{L} - E)^{-1}. \qquad (3.42)$$

We now insert a unit operator $\vec{1} = \sum_j |\psi_j(x,y)\rangle \langle\psi_j(x,y)|$ before and after the Green's operator,

$$\left|\Psi_{E,n_{p_0}}\right\rangle = \sum_j \sum_{j'} |\psi_j(x,y)\rangle \, \mathcal{G}^B_{j,j'}(E) \left\langle\psi_{j'}(x,y)\right| \mathcal{L} \left|\Psi_{E,n_{p_0}}\right\rangle. \qquad (3.43)$$

where $\psi_j(x,y)$ is a complete set of basis functions defined in the interior region. We consider this equation on the qth boundary where the longitudinal coordinate $x_q = 0$

and then project the wave function on to the transverse state vector, $\left|\chi_{q,n_q}(y_q)\right\rangle$ as,

$$\left\langle \chi_{q,n_q}(y_q)\right| \Psi^{q,p_0}_{E,n_{p_0}}(x_q=0,y_q)\Big\rangle = \sum_j \sum_{j'} \sum_{n_p} \quad \left\langle \chi_{q,n_q}(y_q)\right| \psi_j\rangle\, \mathcal{G}^B_{j,j'}(E)\, \langle\psi_j|\, \chi_{p,n_p}(y_p)\rangle$$
$$\left\langle \chi_{p,n_p}(y_p)\right| \mathcal{L}\Psi^{p,p_0}_{E,n_{p_0}}\Big\rangle . \tag{3.44}$$

By defining $\left\langle \chi_{q,n_q}(y_q)\,|\psi_j(x_q=0,y)\rangle\right. = \beta_{j,q,n_q}$ and plugging the form of the Bloch operator,

$$\left\langle \chi_{q,n_q}(y_q)\right| \Psi^{q,p_0}_{E,n_{p_0}}(x_q=0,y_q)\Big\rangle = \sum_{j,j'} \frac{1}{2}\beta_{j,q,n_q}\mathcal{G}^B_{j,j'}(E)\beta^{\star}_{j',p,n_p} \left\langle \chi_{p,n_p}(y_q)\right| \nabla\, \Psi^{p,p_0}_{E,n_{p_0}}(x_p=0,y_p)\Big\rangle . \tag{3.45}$$

We identify the $\mathcal{M}$ matrix as,

$$\mathcal{M}_E(s_p,s_q) = \sum_{j,j'} \frac{1}{2}\beta_{j,q,n_q}\mathcal{G}^B_{j,j'}(E)\beta^{\star}_{j,p,n_p}\,, \tag{3.46}$$

where the matrix for the Green's operator is evaluated in the basis $|\psi_j(x,y)\rangle$. If we choose $|\psi_j(x,y)\rangle$ to be the exact Bloch eigenfunctions $|\phi_j(x,y)\rangle$, the Green's operator is diagonal that,

$$\mathcal{G}^B_{j,j'} = \left\langle \phi_{j'}\right| \frac{1}{E_j - E}\,|\phi_j\rangle = \frac{1}{E_j-E}\;\delta_{j,j'}. \tag{3.47}$$

It recovers the previous result (eq.3.22). Now this equation is similar to the eq. (3.29) which can be solved for the unknown transmission coefficients τ^{q,p_0}_{q,n_q}. The advantage of calculating the R-matrix elements (or the $\mathcal{M}$ matrix elements) from equation (3.46) is that we do not need to solve for the Bloch eigenenergies.

For the T-junction problem, we follow this alternative method. The $\mathcal{M}$-matrix elements are calculated according to the equation (3.46) and then we solve the set of linear equations (3.29) to calculate the transmission coefficients of the system. We have chosen the variational basis set as,

$$\psi_j(x,y) = \eta_a(x)\zeta_b(y). \tag{3.48}$$

The form of these variational basis functions is given in the previous section (eq.C.4).

It is important to note that these variational basis functions are not orthogonal inside the interior region even though they are complete. When we put the basis functions in the Green's operator, we have to make them orthogonal by the Gram-Schmidt orthogonalization, or else the Green's operator takes the form $\mathcal{G}^B_{j,j'} = HB_{j,j'} - E\mathcal{O}_{j,j'}$ where $\mathcal{O}_{j,j'} = \langle \psi_j \left| \psi_{j'} \right\rangle$ is the overlap matrix. In the variational method, this second method is more effective in that we do not need to explicitly solve the generalized eigenvalue problem (eq.2.39) and we do not have to keep track with the eigenvalues.

In the results section (3.3), we show the values of the transmission coefficients for a range of energy. We study the convergence of these results as a function of the number of basis functions used in the calculation. The behavior is studied for both the variational and Wigner-Eisenbud calculations. When doing the projection on to the transverse state vector, we have to choose how many transverse state functions we use. In performing the summation in the equation (3.29), we truncate the summation at a finite value. In this calculation we have found that we need to include a number of evanescent waves to achieve convergence. The number of transverse functions used in this calculation, N should always be larger than the number of open channels $N^q_{\text{open}}(E)$ at that energy. In our calculation we included 10 closed channels so that,

$$N = N^q_{\text{open}}(E) + 10. \tag{3.49}$$

However this number, 10 is not an optimized value. We simply wanted to make sure that we have enough closed channels. Then our results will not depend on the closed channels. We study the convergence of the result with respect to the number of basis functions we used in the interior region calculation.

3.3 Results of the Scattering of Electrons in the T-junction Device

When we look at the transmission coefficients, there are several quantities one can think of. The fundamental quantity is the transmission coefficient from a n_{p_0} subband in the p_0^{th} lead to a n_q^{th} subband in the qth lead, $\mathcal{T}^{q,p_0}_{n_q n_{p_0}}$ which can be calculated according to the equation (3.9). We call this "the state to state transmission coefficient". However when we want to calculate most physical quantities, we have to sum over all the output subbands n_q. That is, the transmission coefficient from the input subband n_{p_0} in the lead p_0 to the output lead q equals $\sum_{n_q}^{N^q_{open}(E)} \mathcal{T}^{q,p_0}_{n_q,n_{p_0}}$ which we call the "state to the lead transmission coefficient". In order to calculate the most relevant quantity, we need to add all the possible input subbands in a given lead which equals $\sum_{n_p}^{N^p_{open}(E)} \sum_{n_q}^{N^q_{open}(E)} \mathcal{T}^{q,p}_{n_q,n_p}$ which we call the "lead to lead transmission coefficient". We denote this as T_{qp}. The transport properties depend on the lead to

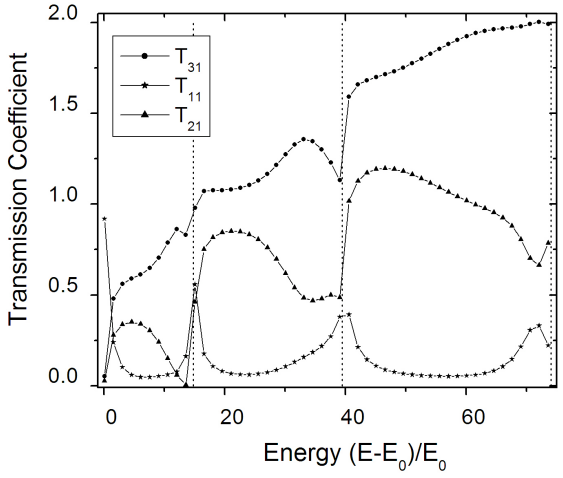

Figure 3.2: Transmission coefficients of electrons traveling in the T junction device. The electrons are injected from the lead 1. The plotted quantities are the lead to lead transmission coefficient. The dotted lines are the threshold energies of the input lead. For this device $w_1 = w_2 = w_3 = 1$.

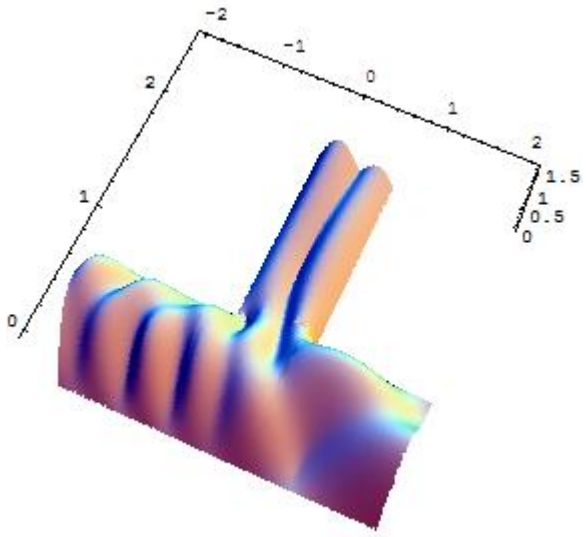

Figure 3.3: A plot of the probability density of electrons traveling in a T-junction device. The energy of the scattering electron, $E = 26$ in the dimensionless units.

lead transmission coefficient T_{qp} which appears in the Landauer equation (eq.1.12).

In the T-junction device we calculate the lead to lead transmission for an electron injected from the lead 1 as shown in the figure (3.1). We show the result (fig.3.2) obtained by 8×8 basis functions. In this case we used the variational parameter $\lambda_x = \lambda_y = 1.3$. This result agrees with the result obtained by John L. Bohn[21] by a different method. In the Bohn's method, he added extra set of basis functions to achieve faster convergence. Our method is easy to code and we need fewer number of basis functions to achieve the convergence. Most importantly, our method is easy to extend for more complicated geometries as we will discuss in the following chapter (ch. 4).

The results in the graph (fig.3.2) also show that the flux is conserved that,

$$\sum_{q=1}^{3} \sum_{n_q=1}^{N^q_{open}(E)} \tau^{q,p_0}_{n_q,n_{p_0}}(E) = 1, \tag{3.50}$$

for all energies.

The probability density for the electron traveling in the T-junction at energy,

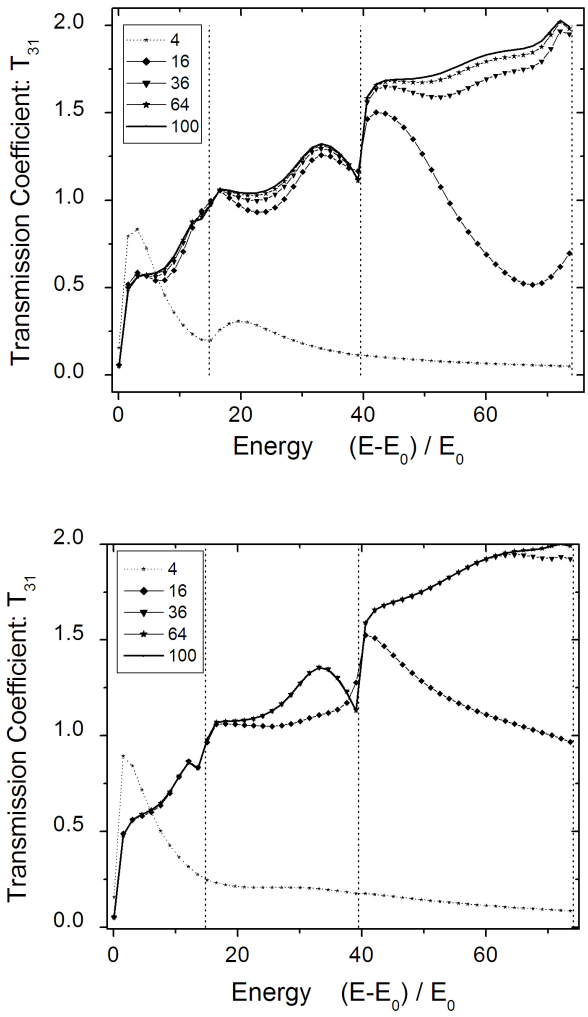

Figure 3.4: Graph of the lead to lead transmission coefficient T_{31}, that is the transmission coefficient of electron to the lead 3 when the electrons are injected from the lead 1. The upper plot is the result obtained using the Wigner-Eisenbud (WE) basis functions and the lower plot is the result obtained using the variational basis functions. In the WE calculation the results are not converged even with 100 (10×10) basis functions. In this variational calculation, there is no graphical difference between the 36 (6×6) calculation and 100 (10×10) calculation which means that the result is converged with 36 (6×6) basis functions. The dotted lines are the threshold energies for the incoming lead.

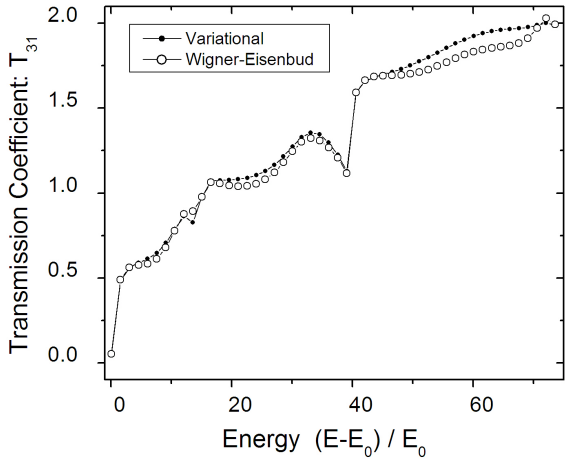

Figure 3.5: The forward lead transmission coefficient calculated using the Wigner Eisenbud (open dots) and the variational (solid dots) basis functions. In both the calculations, we used 100 (10×10) basis functions.

$E = 26$ is shown in the figure (3.3). The calculation parameters for obtaining this plot is as same as that used in the fig.(3.2). Here the wave function is calculated in different segments using the calculated $\tau^{q,p_0}_{n_q n_{p_0}}$ quantities. Each of these segments are plotted together. This diagram (fig.3.3) shows that the probabilities are conserved confirming the accuracy of the technique.

Now we study the convergence of the result shown in the fig. (3.2). In the convergence study, we compare the number of basis functions ($n_{\max} \times m_{\max}$), where $n_{\max}$ is the number of horizontal basis functions and $m_{\max}$ is the number of vertical basis functions used in the calculation. The transmission coefficients are calculated for the forward lead using different numbers of basis functions in the interior region calculation. We do the calculation with the Wigner-Eisenbud calculations and with the variational basis functions. In the variational method, we used the variational parameters as $\lambda_x = \lambda_y = 1.3$. The result is shown in the fig. (3.4). This result shows that the variational calculation achieves the convergence with 36 (6×6) basis functions for most of the energies where as the Wigner-Eisenbud calculation does not

achieve convergence even with 100 (10×10) basis functions. The dotted lines in the figure are threshold energies of the incoming lead. We discuss more about this convergence in the conclusion (sec.3.5).

In the figure (3.5) we plot the results obtained for the transmission coefficient to the lead 3 calculated using the variational and Wigner-Eisenbud basis functions with 10×10 basis functions. It shows that both the results are converged to the same answer. The results in the figure (3.4) shows that the variational basis functions are surely a good set of basis functions to do the calculation. We discuss more about the convergence results in the section (3.5)

3.4 R-Matrix Formula for a Plus-Junction

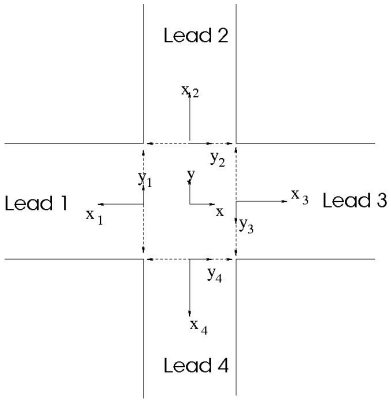

Figure 3.6: A schematic diagram for the plus junction device geometry. We calculate the transmission coefficients of electrons traveling in this device.

As we have mentioned, the equation (3.29) is a common equation that we can use for a device with any number of leads. We use the same formula to calculate the electron scattering in the device sketched in the figure (3.6). The electrons are injected from the lead "1", undergo scattering in the square type scattering region and we are looking for the transmission coefficients in all the 4 outgoing leads.

The only difference between this problem and the T-junction problem is the inte-

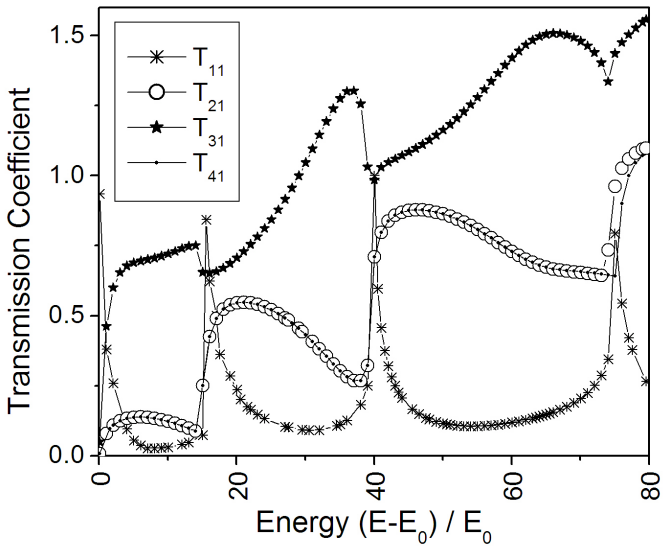

Figure 3.7: Lead to lead transmission coefficients of electrons traveling in the plus junction device (fig.3.6). Electrons are injected from the lead 1. For this device $w_1 = w_2 = w_3 = w_4 = 1.0$.

rior region. The Bloch operator takes the form,

$$\mathcal{L}(x,y) = \frac{1}{2}\left[-\delta(x+\frac{w_2}{2})\frac{\partial}{\partial x} + \delta(x-\frac{w_2}{2})\frac{\partial}{\partial x} - \delta(y+\frac{w_1}{2})\frac{\partial}{\partial y} + \delta(y-\frac{w_1}{2})\frac{\partial}{\partial y}\right]. \tag{3.51}$$

We use a set of variational basis function and then diagonalize the Bloch Hamiltonian for the interior region and find the Bloch eigenfunctions. Then we calculate the $\mathcal{M}$ matrix elements and solve the resultant set of linear equations from (eq.3.29) for the unknown transmission coefficients. In this calculation we used 8×8 variational basis functions for the interior region calculation and 10 non-propagating modes as described in the section (3.2.3). We study the case for a symmetric plus junction for which all the leads are equal in width, however the codes are written for the general case $w_1 \neq w_2$. The figure (3.7) shows the transmission coefficients of electrons in the plus-junction device.

3.5 Conclusion

We have devised a generic R-matrix formula for calculating the transmission coefficients of two-dimensional multi-lead devices. According to the convergence studies of the T-junction results, the transmission coefficients achieved a faster convergence with the variational basis functions. It is important to note that we achieve the convergence with variational basis functions using 36 (6×6) basis functions where as the Wigner-Eisenbud basis functions do not converge the result even with 100 (10×10) basis functions.

Recall that, in the one-dimensional RMT, we found that the Wigner-Eisenbud

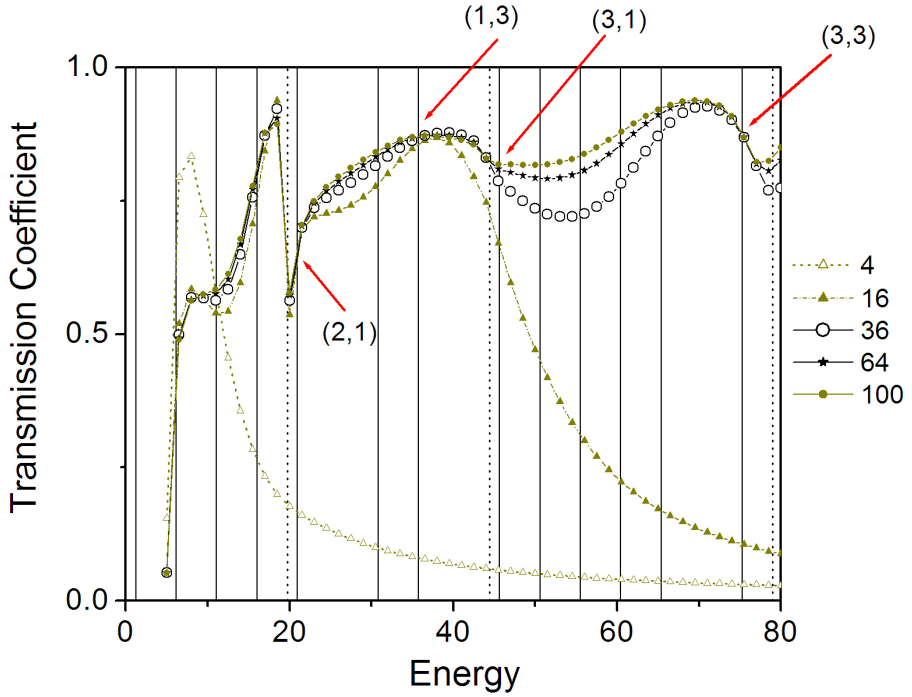

Figure 3.8: State to state transmission coefficient of electrons traveling in the T-junction device. Electrons are injected from $n_1 = 1$ and transmit to $n_3 = 1$. The solid straight lines are the Bloch eigenenergies and the dotted lines are the threshold energies of the lead 1. The Wigner-Eisenbud result does not converge at every Bloch eigenenergy as in the one-dimensional case.

calculation does converge to the correct answer when the scattering energy equals to the Bloch eigenenergies (fig.2.12). In the 2-dimensional case, we see the same sort of behavior, the WE basis functions achieve convergence at certain scattering energies but not at all the scattering energies like the variational approach. The question is do these converging energies equal to the Bloch eigenenergies as in the one-dimensional case?

We find that the quantity we should look at is the state to state transmission coefficient, but not the state to lead or lead to lead transmission coefficient because state to state transmission coefficient is the raw outcome of the R-matrix calculation. We plot the state to state transmission coefficient, $n_1 = 1$ in the lead 1 to the $n_2 = 1$ in the lead 3 in the T-junction device as shown in the figure (3.8). The solid straight lines are the Bloch eigenenergies of the system where as the dotted straight lines are the threshhold energies of the input lead. The result clearly shows that the convergence of the WE calculation occurs at some Bloch eigenenergies but not at all the Bloch eigenenergies. This is clear that unlike in the one-dimensional case not all the Bloch eigenenergies have the correct symmetry as in the scattering wave function. Even though the scattering wave function has the zero derivative boundary conditions at the Bloch eigenenergies, it can have different symmetries than the Wigner-Eisenbud basis functions. In the graph (fig.3.8), we mark arrows where we see the convergence behavior in the Wigner-Eisenbud calculation. Those converged points correspond to some Bloch eigenenergies (n,m) as marked in the figure. Here n and m are the quantum numbers corresponding to the horizontal and vertical directions respectively. According to these results, we conclude that when the quantum number of the Bloch eigenenergy in the vertical directions is an odd number, we get maximum convergence in the Wigner-Eisenbud calculation.

Chapter 4

R-Matrix Connection Formula

4.1 Introduction

In the previous chapter (ch.3), we formulated a generalized R-matrix equation which can be used to calculate the transmission coefficients of a multi-lead device. The main requirement of RMT is to calculate the interior region Bloch eigenfunctions. At the least, it is required to find a set of basis functions that satisfy the physical hard wall boundary conditions of the interior scattering region. Then we can use either the Green function equation (3.43) or directly diagonalize the Bloch Hamiltonian to calculate the R-matrix elements. We have demonstrated the technique for calculating the transmission coefficients of electrons in devices such as the T-junction and the plus junction.

However due to some experimental settings and physical advantages, experimentalists often design devices in which the interior region geometries are more complicated. In such cases it is hard to calculate the Bloch eigenfunctions and it is hard to find a set of basis functions that satisfies the physical boundary conditions. While it is still possible to calculate the Bloch eigenfunctions by discretizing real space, the process will be computationally slow. Therefore it is important to develop a method to calculate the transmission coefficients of such a device without having to consider

the solutions in the total interior region.

We have developed a technique which we call "the R-matrix connection formula" to calculate the transmission coefficients of electrons in such a device with a complicated interior region geometry. The basic idea of this technique is that we divide the complicated interior scattering region into parts such that the interior region can be identified as a combination of some simple geometries. For instance, we shall consider the device shown in the figure (4.2). The interior region (shaded region) does not have a simple geometry. It is hard to find a set of basis functions which satisfy the physical boundary conditions that confines the electron to the shaded region. In our new technique, the R-matrix connection formula, we identify the shaded region in the figure (4.2) as a combination of two wedge geometries as shown in the inset of the same figure. We can find a set of basis functions to satisfy the boundary conditions for electrons confined in a single wedge. Even though the basis functions for a single wedge is not obvious, we can find such a set as we describe in the appendix (C). Knowing the Bloch eigenfunctions in a single wedge, we combine two wedges to calculate the transmission coefficients.

The technique we use is similar to the R-matrix propagation technique that is used in atomic and molecular physics [22]. We extend this idea to two-dimensional devices. The main goal of this chapter is to explain the procedure for calculating the transmission coefficients for electrons in a two-dimensional device with a complicated geometry without considering the total scattering region as a whole, but considering it as a combination of several simple geometries. This chapter is structured as follows.

First we will explain the basic concept for a one-dimensional tube (sec.4.2) where we follow the calculation done by Light et al. [22]. In the section (4.3), we extend this propagation technique to a two-dimensional device. There we develop the mathematical equations to connect two interior regions in two-dimensions with an example, the electron scattering in a diamond-shaped device (fig.4.2).

Then we discuss the application of this theory to a four-terminal wedge geome-

try (fig.4.2). This geometry is similar to the geometry of the device made by Goel et al. for an experiment on ballistic transport in InSb quantum wells. In this experiment, the transport properties are measured when there is an applied magnetic field perpendicular to the device. However in this chapter we study the scattering of this geometry with no magnetic field. We develop the technique here to handle this complicated geometry. In the chapter (6), we show how to study the scattering of electrons in the presence of an applied magnetic field.

4.2 One-Dimensional R-Matrix Connection Formula

The goal of this section is to discuss the basics of "R matrix connection formula" . We start with a one-dimensional device. We explain the technique with an application, electrons traveling in an open tube. It is the same problem we discussed in the previous chapter (sec.2.4), however here we use two interior regions.

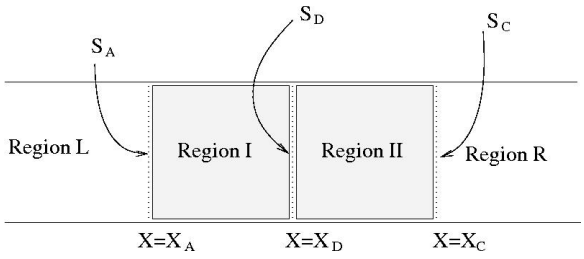

Figure 4.1: A schematic diagram of an open tube with two interior regions. Electrons are injected from the region L, undergo scattering in the regions I and II. We seek the transmission amplitude in the region R which we solve using the R-matrix connection formula.

We consider the tube in four different regions as shown in the figure (4.1), where regions I and II are the interior regions for an electron injected from region L. We seek the final solution, the transmission amplitude in the region R. This problem has a known answer: the electron will have unit transmission amplitude in the region R. We use this problem to explain the basics of the R-matrix connection formula.

The four regions, I, II, L and R are separated by the boundaries S_A, S_D and S_C (fig.4.1). We avoid using the character B in the notation as we need to save that for denoting the magnetic field in the chapter (6). To clearly understand the algorithm, we define the R-matrices R^I, R^{II} and R^{total}. The matrix, R^I relates the scattering wave function in the regions L and II, R^{II} relates the scattering wave function in regions I and R, and R^{total} relates the scattering wave function in regions L and R. Our goal is to find out the components of R^{total} knowing the components of R^I and R^{II}.

We apply the R-matrix equation (eq.2.27) to relate the scattering wave function in different regions and then apply the boundary conditions to connect the matrices which we will describe here.

Using the R-matrix, R^I we can write the scattering wave function in the region L and in the region II which takes the matrix form as,

$$\begin{pmatrix} \Psi^L(x=x_A) \\ \Psi^{II}(x=x_D) \end{pmatrix} = \begin{pmatrix} R_1^I & R_2^I \\ R_3^I & R_4^I \end{pmatrix} \begin{pmatrix} -\frac{d}{dx}\Psi^L(x=x_A) \\ \frac{d}{dx}\Psi^{II}(x=x_D) \end{pmatrix}. \tag{4.1}$$

The superscripts on the wave functions are to denote the region where the function is defined. For instance $\Psi^L(x=x_D)$ means that the scattering wave function defined in the region L and evaluated at the boundary D. The R-matrices also have superscripts, R^I is the R-matrix evaluated in the region I using the Bloch eigenfunctions of the interior region I. Now using the R-matrix R^{II}, we can relate the scattering wave function at the boundaries D and C,

$$\begin{pmatrix} \Psi^I(x=x_D) \\ \Psi^R(x=x_C) \end{pmatrix} = \begin{pmatrix} R_1^{II} & R_2^{II} \\ R_3^{II} & R_4^{II} \end{pmatrix} \begin{pmatrix} -\frac{d}{dx}\Psi^I(x=x_D) \\ \frac{d}{dx}\Psi^R(x=x_C) \end{pmatrix}. \tag{4.2}$$

Since we are not interested in the scattering wave function in the interior region, we want to eliminate the terms Ψ^I and Ψ^{II} from these equations. We want to write an equation which relates the scattering wave function in the incoming and outgoing regions (L and R) only. Mathematically this can be written as,

$$\begin{pmatrix} \Psi^L(x=x_A) \\ \Psi^R(x=x_C) \end{pmatrix} = \begin{pmatrix} R_1^{total} & R_2^{total} \\ R_3^{total} & R_4^{total} \end{pmatrix} \begin{pmatrix} -\frac{d}{dx}\Psi^L(x=x_A) \\ \frac{d}{dx}\Psi^R(x=x_C) \end{pmatrix} \tag{4.3}$$

However, since the Bloch eigenfunctions of the total interior region are assumed to be hard to calculate, the elements of the matrix R^{total} are not known. Our goal is to find out the elements of the matrix R^{total} in terms of the elements of R^I and R^{II} using the boundary conditions.

The scattering wave function should satisfy the physical boundary conditions, the continuity of the wave function,

$$\Psi^I(x=x_D) = \Psi^{II}(x=x_D), \tag{4.4}$$

and the continuity of the derivative of the wave function,

$$\frac{d}{dx}\Psi^I(x=x_D) = \frac{d}{dx}\Psi^{II}(x=x_D), \tag{4.5}$$

at $x = x_D$. Invoking these boundary conditions, the terms $\Psi^{I,II}(x = x_D)$ and $\frac{d}{dx}\Psi^{I,II}(x)|_{x=x_D}$ can be eliminated from (4.1) and (4.2) and then we get an equation of the form (4.3).

This yields,

$$R_1^{\text{total}} = R_1^I - R_2^I Z R_3^I \tag{4.6}$$

$$R_2^{\text{total}} = R_2^I Z R_2^{II} \tag{4.7}$$

$$R_3^{\text{total}} = R_3^{II} Z R_3^I \tag{4.8}$$

$$R_4^{\text{total}} = -R_3^{II} Z R_2^{II} + R_4^I \tag{4.9}$$

where, $Z = (R_4^I + R_1^{II})^{-1}$

The elements of the two R-matrices R^I and R^{II} can be calculated exactly following the method described in the section (2.4) and then calculate the elements of the matrix, R^{total}. Once we know the elements of R^{total}, we can calculate the transmission amplitudes following the procedure explained in the section (2.4). We can numerically calculate the transmission amplitude.

By looking at the above procedure, a reasonable question arises. Why cannot we use only the equation (4.1) to calculate the transmission coefficients on the region L and likewise use only the equation (4.2) to find the transmission coefficient in the region R? In particular, one can use the equation (4.1) and write Ψ^L in terms of the transmission coefficients in the region R and write Ψ^{II} in terms of the Bloch eigenfunctions in the region II. We found that when we take the derivative of the Bloch eigenfunctions, the scattering amplitudes does not converge to the correct answer. In fact, the value of the scattering wave function matches, but the derivative of the scattering wave function does not match in this approach. So it is important to avoid taking the derivative of the Bloch eigenfunctions.

4.3 2-Dimensional R-Matrix Connection Formula: Application to the Electron Scattering by a Diamond-Shaped Device

Here we extend the one-dimensional connection formula described in the section (4.2) to a two-dimensional device using the example of the scattering of electrons in a diamond shaped geometry (fig.4.2). Electrons are injected to the system from the region L, undergo scattering in the shaded region, then reflect and transmit into the regions L and R.

If we were to solve this problem using single interior region R-matrix theory (ch.3), we would have to first find out a set of basis functions which goes to zero on the edges of the diamond structure and then using these basis functions to calculate the elements of the R matrix (or $\mathcal{M}$ matrix eq.3.29). It is possible to find a basis set to satisfy the hard wall boundary conditions of the diamond-shaped geometry by discretizing the real space, however the process will be computationally slow. We would rather use a set of analytic basis functions, then most of the overlap integrals can be done

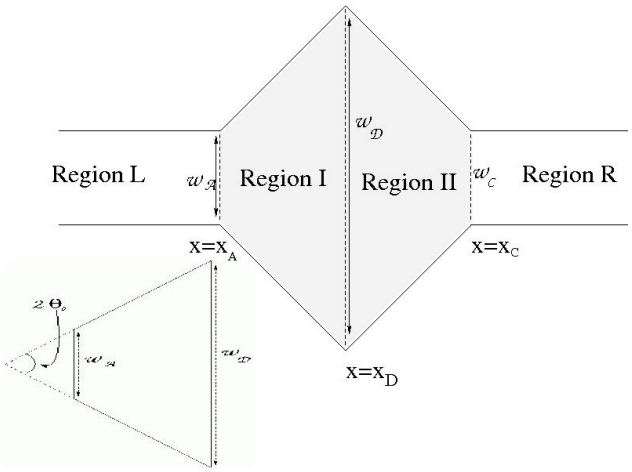

Figure 4.2: A schematic diagram of a device with a diamond geometry. We consider this device in 4 regions, L, I, II, and R, which are separated by the soft boundaries at $x = x_A$, $x = x_D$, and $x = x_C$. Electrons are injected from the left lead, undergo scattering in the regions I and II, and scatter into the regions L and R. We recognize the diamond shaped interior region as a combination of two wedges as shown in the inset. We calculate the transmission coefficients in the two outgoing leads L and R using the R-matrix connection formula by connecting the Bloch eigenfunctions of a wedge, but not using the eigenfunctions of a diamond shaped geometry.

analytically. Since it is hard to find such a set of analytic basis functions for the diamond geometry, we identify this diamond-shaped interior region as two wedge geometries (inset of fig.4.2) connected together. We find a set of basis functions to satisfy the physical boundary conditions for a single wedge and then connect them to solve for the transmission coefficients. The Bloch eigenfunctions of a single wedge are also not obvious, however we find a way to do this analytically. The calculation of the Bloch eigenfunctions is explained in the appendix (C). Knowing the Bloch eigenfunctions in a wedge, we explain the procedure for calculating the transmission coefficients of electrons traveling in a diamond shaped geometry.

Our starting point is the single interior region R-matrix equation (eq.3.27). This equation is used to relate the scattering wave function $\left|\Psi^L\right\rangle$, $\left|\Psi^I\right\rangle$, $\left|\Psi^{II}\right\rangle$ and $\left|\Psi^R\right\rangle$ in four different regions. In detail $\left|\Psi^L\right\rangle$ and $\left|\Psi^{II}\right\rangle$ are related by R^I, the R-matrix

in the interior region I which is defined in terms of $\left|\phi_j^I\right\rangle$, the Bloch eigenfunctions in that region. In a similar way, $\left|\Psi^I\right\rangle$ and $\left|\Psi^R\right\rangle$ are related by R^{II}, the R-matrix defined using $\left|\phi_j^{II}\right\rangle$, the Bloch eigenfunctions in the interior region II. We call the three soft boundaries as A, D and C. Again, we avoid using "B" to prevent confusion with the symbol for the magnetic field in chapter (6).

As we have proved in the previous chapter (eq.3.27), we can write the scattering wave function on the qth boundary projected on to the transverse state vector $\left|\chi_{q,n_q}\right\rangle$ as,

$$\left\langle \chi_{q,n_q}(y_q)\left|\Psi_{E,n_{p_0}}(x_q=0,y_q)\right\rangle\right. = \sum_{p,n_p} \mathsf{M}_{q,n_q,p,n_p}\left\langle \chi_{p,n_p}\left|\mathcal{L}\Psi_{E,n_{p_0}}(x_q=0,y_q)\right\rangle\right., \quad (4.10)$$

where,

$$\mathsf{M}_{q,n_q,p,n_p} = \sum_j \frac{\gamma_{j,q,n_q}\gamma^{\star}_{j,p,n_p}}{E_j - E}. \quad (4.11)$$

Note that the matrices $\mathcal{M}$ (eq.3.30) and M only differ by a factor 2. That is because we here choose to keep the Bloch operator as $\mathcal{L}$ without substituting the explicit form. For simplicity, we shall use the notation $f^j_{q,n_q} = \left\langle \chi_{q,n_q}(y_q)\left|\Psi^j_{E,n_{p_0}}(x_q,y_q)\right\rangle\right.$. The superscript j denotes the region where the function is defined. Also note that p_0 is the lead where the electrons are injected from that for this problem $p_0 = L$. However, throughout this calculation, we keep it as p_0. Now we write the function f^j_{q,n_q} in different regions. First we use the equation (4.10) to write down f^L_{A,n_A} and f^{II}_{D,n_D} using the interior region I as,

$$\begin{aligned} f^L_{A,n_A}(x=x_A) &= \sum_{n'_A} \mathsf{M}^I_{A,n_A,A,n'_A}\left\langle \chi_{A,n'_A}(y_A)\right|\left.\mathcal{L}^I_A\Psi^L_{E,n_{p_0}}(x=x_A,y_A)\right\rangle + \\ &\quad \sum_{n_D} \mathsf{M}^I_{A,n_A,D,n_D}\left\langle \chi_{D,n_D}(y_D)\left|\mathcal{L}^I_D\Psi^{II}_{E,n_{p_0}}(x=x_D,y_D)\right\rangle\right., \quad (4.12) \end{aligned}$$

and,

$$\begin{aligned} f^{II}_{D,n_D}(x=x_D) &= \sum_{n_A} \mathsf{M}^I_{D,n_D,A,n_A}\left\langle \chi_{A,n_A}(y_A\left|\mathcal{L}^I_A\Psi^L_{E,n_{p_0}}(x=x_A,y_A)\right\rangle\right. + \\ &\quad \sum_{n'_D} \mathsf{M}^I_{D,n_D,D,n'_D}\left\langle \chi_{D,n'_D}(y_D)\left|\mathcal{L}^I_D\Psi^{II}_{E,n_{p_0}}(x=x_D,y_D)\right\rangle\right. . \quad (4.13) \end{aligned}$$

Note that when compared to the single interior region problem, we have an additional superscript to specify the region. For instance $\mathsf{M}^{I}_{q,n_q,p,n_p}$ is the M_{q,n_q,p,n_p} evaluated according to the equation (4.11) using the basis functions defined in the interior region I. Similar to the equations (4.12) and (4.13), we can write another two equations for f^{I}_{D,n_D} and f^{R}_{C,n_C} using the interior region II,

$$\begin{aligned} f^{I}_{D,n_D}(x = x_D) &= \sum_{n'_D} \mathsf{M}^{II}_{D,n_D,D,n'_D} \left\langle \chi_{D,n'_D}(y_D) \left| \mathcal{L}^{II}_{D} \Psi^{I}_{E,n_{p_0}}(x = x_D, y_D) \right\rangle + \right. \\ &\quad \sum_{n_C} \mathsf{M}^{II}_{D,n_D,C,n_C} \left\langle \chi_{C,n_C}(y_C \left| \mathcal{L}^{II}_{C} \Psi^{R}_{E,n_{p_0}}(x = x_C, y_C) \right\rangle \right., \end{aligned} \tag{4.14}$$

and

$$\begin{aligned} f^{R}_{C,n_C}(x = x_C) &= \sum_{n_D} \mathsf{M}^{II}_{C,n_C,D,n_D} \left\langle \chi_{D,n_D}(y_D \left| \mathcal{L}^{II}_{D} \Psi^{I}_{E,n_{p_0}}(x = x_D, y_D) \right\rangle + \right. \\ &\quad \sum_{n'_C} \mathsf{M}^{II}_{C,n_C,C,n'_C} \left\langle \chi_{C,n'_C}(y_C \left| \mathcal{L}^{II}_{C} \Psi^{R}_{E,n_{p_0}}(x = x_C, y_C) \right\rangle \right. . \end{aligned} \tag{4.15}$$

Now we introduce the physical boundary conditions, the wave function and the flux are continuous across the boundary D,

$$\left| \Psi^{I}_{E,n_{p_0}}(x = x_D, y_D) \right\rangle = \left| \Psi^{II}_{E,n_{p_0}}(x = x_D, y_D) \right\rangle, \tag{4.16}$$

$$\mathcal{L}^{I}_{D} \left| \Psi^{II}_{E,n_{p_0}}(x = x_D, y_D) \right\rangle = -\mathcal{L}^{II}_{D} \left| \Psi^{I}_{E,n_{p_0}}(x = x_D, y_D) \right\rangle. \tag{4.17}$$

It is important to note that the second boundary equation is the continuity of the derivative of the wave function, or in a more physical sense the continuity of the momentum or the flux through the boundary. The negative sign indicates that flux going out from the surface D of interior region I is injected into the interior region II from the surface D. The Bloch operator turns out to be the flux operator through the surfaces of the finite region.

In two dimensions, the boundary conditions become functions of the transverse coordinate y_D. These boundary conditions can also be projected on to the transverse state vector $|\chi_{D,n_D}(y_D)\rangle$ of the surface D, that the equations (4.16) and (4.17) reduced to,

$$f^{I}_{D,n_D} = f^{II}_{D,n_D}, \tag{4.18}$$

and

$$\langle\chi_{D,n_D}(y_D)\left|\mathcal{L}_D^I\Psi_{E,n_{p_0}}^{II}(x=x_D)\right\rangle = -\langle\chi_{D,n_D}(y_D)\left|\mathcal{L}_D^{II}\Psi_{E,n_{p_0}}^{I}(x=x_D)\right\rangle. \quad (4.19)$$

For simplicity we use the symbol $\mathsf{D}_{n_D} = \langle\chi_{D,n_D}(y_D)\left|\mathcal{L}_D^I\Psi_{E,n_{p_0}}^{II}(x=x_D,y_D)\right\rangle$. We apply the boundary condition, eq.(4.18) and eq.(4.19) in the equation (4.13) and (4.14) which gives,

$$\sum_{n_A}\mathsf{M}^I_{D,n_D,A,n_A}\langle\chi_{A,n_A}\left|\mathcal{L}_A^I\Psi^L_{E,n_{p_0}}(x=x_A)\right\rangle + \sum_{n'_D}\mathsf{M}^I_{D,n_D,D,n'_D}\mathsf{D}_{n'_D} =$$
$$\sum_{n'_D}\mathsf{M}^{II}_{D,n_D,D,n'_D}(-\mathsf{D}_{n'_D}) + \sum_{n_C}\mathsf{M}^{II}_{D,n_D,C,n_C}\langle\chi_{C,n_C}\left|\mathcal{L}_C^{II}\Psi^R_{E,n_{p_0}}(x=x_C)\right\rangle. \quad (4.20)$$

Also with the new notation D_{n_D}, the equations (4.12) and (4.15) are reduced to,

$$f^L_{A,n_A}(x=x_A) = \sum_{n'_A}\mathsf{M}^I_{A,n_A,A,n'_A}\left\langle\chi_{A,n'_A}\left|\mathcal{L}_A^I\Psi^L_{E,n_{p_0}}(x=x_A)\right\rangle + \sum_{n_D}\mathsf{M}^I_{A,n_A,D,n_D}\mathsf{D}_{n_D},\right. \quad (4.21)$$

and,

$$f^R_{C,n_C}(x=x_C) = \sum_{n_D}\mathsf{M}^{II}_{C,n_C,D,n_D}(-\mathsf{D}_{n_D}) + \sum_{n'_C}\mathsf{M}^{II}_{C,n_C,C,n'_C}\left\langle\chi_{C,n'_C}\left|\mathcal{L}_C^{II}\Psi^R_{E,n_{p_0}}(x=x_C)\right\rangle.\right. \quad (4.22)$$

Our system of equations now consist of eq.(4.20), eq.(4.21) and eq.(4.22). Since these equations have the Bloch operator term $\mathcal{L}_A^I{}^{II}_C$, we will write the explicit form of them. Note that the Bloch operator term in these final equations acts on the scattering wave functions in the outgoing leads L or R. It is convenient to write the Bloch operator in the lead coordinates. The Bloch operators take the form,

$$\mathcal{L}_A^I = \frac{1}{2}\frac{\partial}{\partial x_L}, \quad (4.23)$$

and

$$\mathcal{L}_C^{II} = \frac{1}{2}\frac{\partial}{\partial x_R}, \quad (4.24)$$

where x_L and x_R are the longitudinal coordinates which are defined in the similar way as the lead coordinates in the T-junction problem (sec.3.2).

Also note that we can use the equations (3.20) and (3.21) to simplify the equations (4.20), (4.21) and (4.22) which gives our final system of equations as,

$$\sum_{n_A} \mathcal{M}^{I}_{D,n_D,A,n_A} \left(-ik_{A,n_A}\delta_{n_A,n_{p_0}} + ik_{A,n_A}\tau^{L,L}_{n_A,n_{p_0}} \right) + \sum_{n'_D} \left(\mathcal{M}^{I}_{D,n_D,D,n'_D} + \mathcal{M}^{II}_{D,n_D,D,n'_D} \right) \mathcal{D}_{n'_D} = \sum_{n_C} \mathcal{M}^{II}_{D,n_D,C,n_C} ik_{C,n_C}\tau^{R,L}_{n_C,n_{p_0}}, \quad (4.25)$$

$$\delta_{n_A,n_{p_0}} + \tau^{L,L}_{n_A,n_{p_0}} = \sum_{n'_A} \mathcal{M}^{I}_{A,n_A,A,n'_A} \left(-ik_{A,n'_A}\delta_{n'_A,n_{p_0}} + ik_{A,n'_A}\tau^{L,L}_{n'_A,n_{p_0}} \right) + \sum_{n_D} \mathcal{M}^{I}_{A,n_A,D,n_D} \mathcal{D}_{n_D}, \quad (4.26)$$

and,

$$\tau^{R,L}_{n_C,n_{p_0}} = \sum_{n_D} \mathcal{M}^{II}_{C,n_C,D,n_D}(-\mathcal{D}_{n_D}) + \sum_{n'_C} \mathcal{M}^{II}_{C,n_C,C,n'_C} ik_{C,n_C}\tau^{R,L}_{n_C,n_{p_0}}. \quad (4.27)$$

We have substituted $\mathcal{M} = \mathsf{M}/2$ and define a new symbol $\mathcal{D} = \mathsf{D}/2$. Now this set of equations (4.25, 4.26 and 4.27) can be solved for the unknown transmission amplitudes $\tau^{L,L}_{n_A,n_{p_0}}$, $\tau^{R,L}_{n_C,n_{p_0}}$ and the unknowns, $\mathcal{D}_{n_D}$ related to the boundary surface D.

It is possible to eliminate the unknowns $\mathcal{D}_{n_D}$ from the above equations and solve only for the transmission amplitudes. However it is simpler and convenient to keep $\mathcal{D}_{n_D}$'s as unknowns and solve the above three equations simultaneously. Calculation of the elements of matrix $\mathcal{M}$ is explained in the appendix(C).

Knowing the $\mathcal{M}$ matrix elements, we can simultaneously solve the set of equations (4.25, 4.26 and 4.27), for the transmission amplitudes. With the transmission amplitudes, we calculate the transmission coefficients, $\mathcal{T}^{R,L}_{n_R,n_{p_0}}$ $\mathcal{T}^{L,L}_{n_L,n_{p_0}}$ using the eq.(3.9). These are the state to state transmission coefficient as we explained in the chapter (3). That is $\mathcal{T}^{R,L}_{n_R,n_{p_0}}$ is the transmission coefficient of electrons from the $n^{th}_{p_0}$ subband of the lead L to the n^{th}_R subband of the lead R. The graph (fig.4.3) shows the state to lead reflection and transmission coefficients, $\sum_{n_R} \mathcal{T}^{R,L}_{n_R,n_{p_0}}$ and $\sum_{n_L} \mathcal{T}^{L,L}_{n_L,n_{p_0}}$ of the electrons traveling in a double-wedge geometry when the incoming electron is in the first subband.

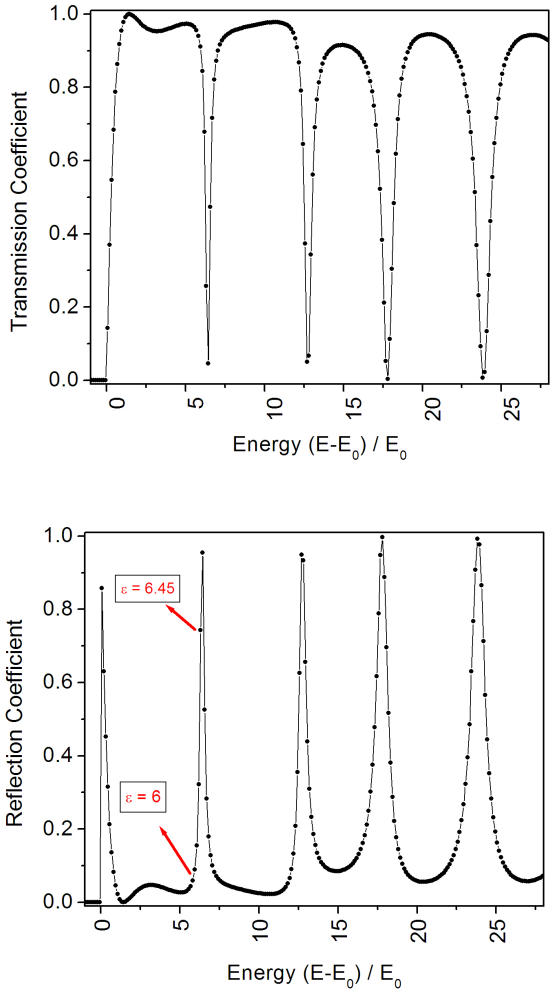

Figure 4.3: Transmission and reflection coefficients of the electrons injected to a double-wedge geometry shown in the figure (4.2). The upper plot is the transmission coefficients (to the lead R) and the lower plot is the reflection coefficients (to the lead L) as a function of the energy of the electron. In this calculation the wedge is defined by $w_A = 1$ (all the lengths of the system is measured in terms of the width w_A), $w_D = 2.5$. The opening angle of the wedge (inset of the figure 4.2), $2\theta_0 = \pi/3$. The electron is injected in the first subband and the transmission coefficients are summed over all the output subbands, so that this is the state to lead transmission coefficients. We have marked the anti-resonance ($\epsilon = 6$) and the resonance state ($\epsilon = 6.45$). The probability densities at the resonance and the anti-resonance are shown in the figure (4.4).

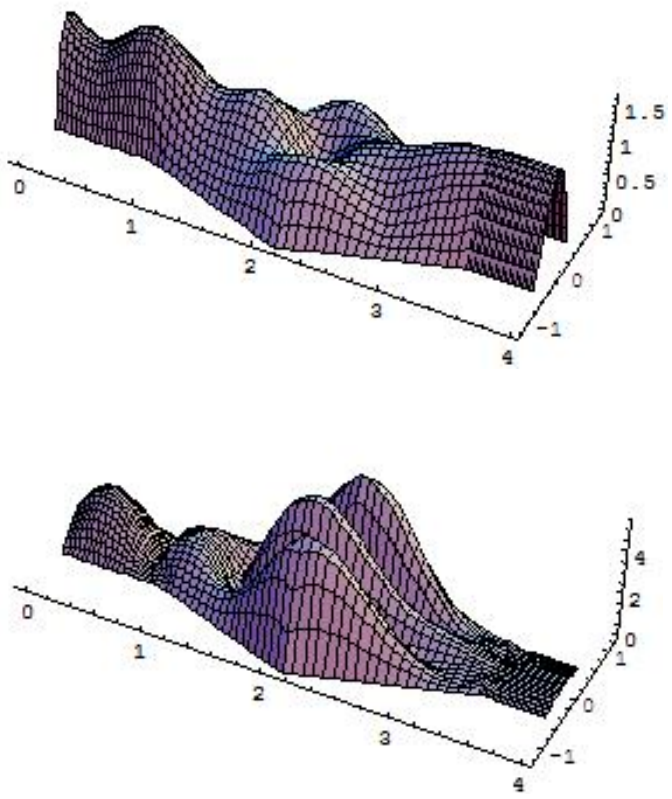

Figure 4.4: The probability density of an electron traveling in a device with a diamond shaped geometry at resonances and anti-resonances. The upper figure is the $|\Psi|^2$ at energy, $E = 6$ (anti-resonance: electron has a minimum amplitude inside the scattering region.) and the lower figure is the $|\Psi|^2$ at $E = 6.45$ (resonance: electron has a maximum amplitude inside the scattering region).

The transmission through a diamond-shaped device has interesting resonance behaviors. For instance, in the graph (fig.4.3), at the energy $\epsilon = 6$, we get maximum transmission that the system is at anti-resonance as shown in the upper plot of the figure (4.4). The electron state has a minimum amplitude in the scattering region at the anti-resonance state. At energy $\epsilon = 6.45$ we get the maximum reflection that the system is at resonance as shown in the figure (4.4). At this resonance state, the electron state has a higher amplitude inside the scattering region. These resonances should be due to the eigenstates of the interior region. At such resonances in atomic

systems the electron has a large amplitude at the location of the scatterer. We can find that from the scattering wave function in the device. We calculate the scattering wave function in the device using the transmission amplitudes and the coefficients $\mathcal{D}_{n_D}$.

Even though the unknowns, $\mathcal{D}_{n_D}$ do not lead to physical quantities such as the transmission coefficients in the out going leads, we need those coefficients to calculate the scattering wave functions inside the interior region. The figure (4.4) shows the probability density of the electrons traveling in a double wedge geometry at resonances and anti resonances. We see that in resonances, the probability for the electron to be found within the diamond is maximum. For an anti-resonance this is reversed.

4.4 Scattering of Electrons in a 4-Terminal Wedge Geometry

In this section, we apply the 2-dimensional R-matrix connection formula to devices with many leads and more complicated interior regions. This is very important since most of the experimental devices have more than two outgoing leads.

We consider a 4-terminal device which has a more complicated interior region than the 4-terminal square junction device which we discussed in the section (3.4). We sketch the device in the figure (4.5) which we refer to as the 4-terminal wedge junction device.

This geometry (fig.4.5) was initiated by the geometry of the device that was made for the bend resistance experiment by Goel et. al [10]. Our ultimate goal is to simulate the transport properties of such a device via Landauer-Bütikker theory. In the mentioned bend resistance experiment, the transport properties were measured in the presence of a magnetic field. In this chapter we do not address this exact experimental observation with the magnetic field, however we develop the technique for handling the complicated geometry. In the chapter (6) we use the connection

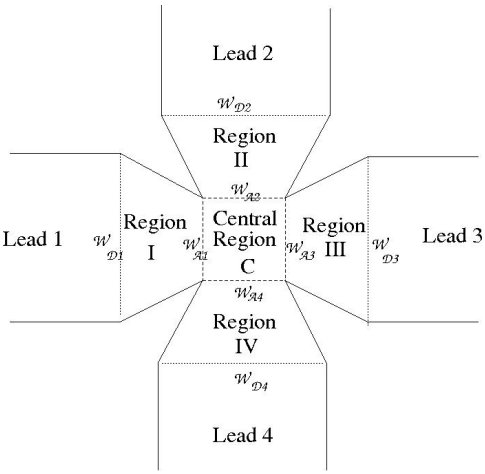

Figure 4.5: A schematic diagram of a 4-terminal wedge junction device. Electrons are injected from the lead 1 and scatter in the interior region and scatter out in to leads 1, 2, 3, and 4. We seek for the transmission coefficients of the electrons to those 4 leads. We calculate the transmission coefficients using the R-matrix connection formula since the interior scattering region has a complicated structure.

technique with the magnetic-field RMT to model that experimental observation.

We recognize the interior scattering region of this device as a combination of 4 wedge geometries attached to the central square region. There are 5 interior regions which we call region I, II, III, IV and C. So we need to write 5 sets of equations corresponding to each interior region. There are four internal boundaries that we name as s_{D1}, s_{D2}, s_{D3} and s_{D4}. We call them internal boundaries since they are not attached to an outgoing lead. We need to invoke the boundary conditions similar to eq.(4.16) and (4.17) at all of these 4 internal surfaces.

We have 4 sets of unknown transmission amplitudes corresponding to the 4 outgoing leads and another 4 sets of unknowns, $\mathcal{D}1_{n_{D1}}$, $\mathcal{D}2_{n_{D2}}$, $\mathcal{D}3_{n_{D3}}$ and $\mathcal{D}4_{n_{D4}}$ corresponding to the 4 internal boundaries which do not carry physical information. However, we solve for all of these 8 sets of unknowns and calculate the transmission coefficients by the first 4 sets of unknowns. The algebra is quite involved and we explain it in detail in the appendix (D).

In this calculation, we have used 10×10 basis functions to diagonalize the Bloch Hamiltonians in both the square type central interior region and the wedge-shaped interior regions. We use 10 non-propagating channels in each of the out going leads. More about the calculation can be learned from the appendix.

We can transform the 4-terminal wedge geometry to a 4-terminal square device by adjusting the dimensions of the wedge (we use $w_{A1} = 1.0$, $w_{D1} = 1.05$ and $\theta_0 = \pi/4$). The result is shown in the figure (4.6). It correctly recovers the result for the 4-terminal square junction device.

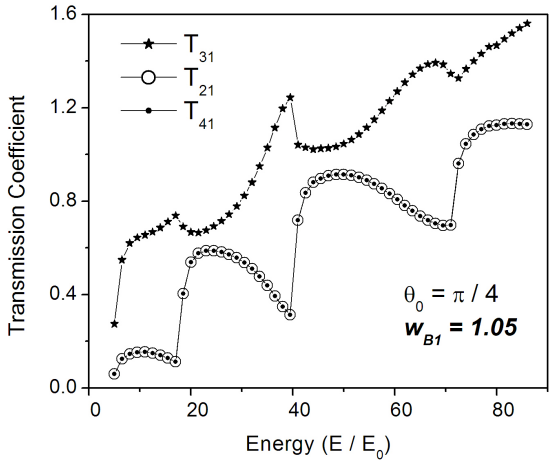

Figure 4.6: Transmission coefficients of the electrons in a 4-terminal wedge junction. The stars are the transmission coefficient to the forward lead, open dots are to the left lead and the solid dots are to the right going lead. The device used here is symmetric. The specifics of each wedge are such that $\theta_0 = \pi/4$, $w_{A1} = 1.0$, and $w_{D1} = 1.05$, in which the 4-terminal wedge device is turned onto a 4-terminal square junction device. This results recovers the result we obtained in the section 3.4.

We calculate the transmission coefficients of the electrons in this 4-terminal wedge device with different specifics of the wedge geometry. We keep the opening angle $2\theta_0 = 43^0$, $w_{A1} = 1.0$ and calculate the transmission coefficients for different values of w_{D1}. The result is shown in the figure (4.7).

This value of opening angle is similar to that of the experimental device [10] that

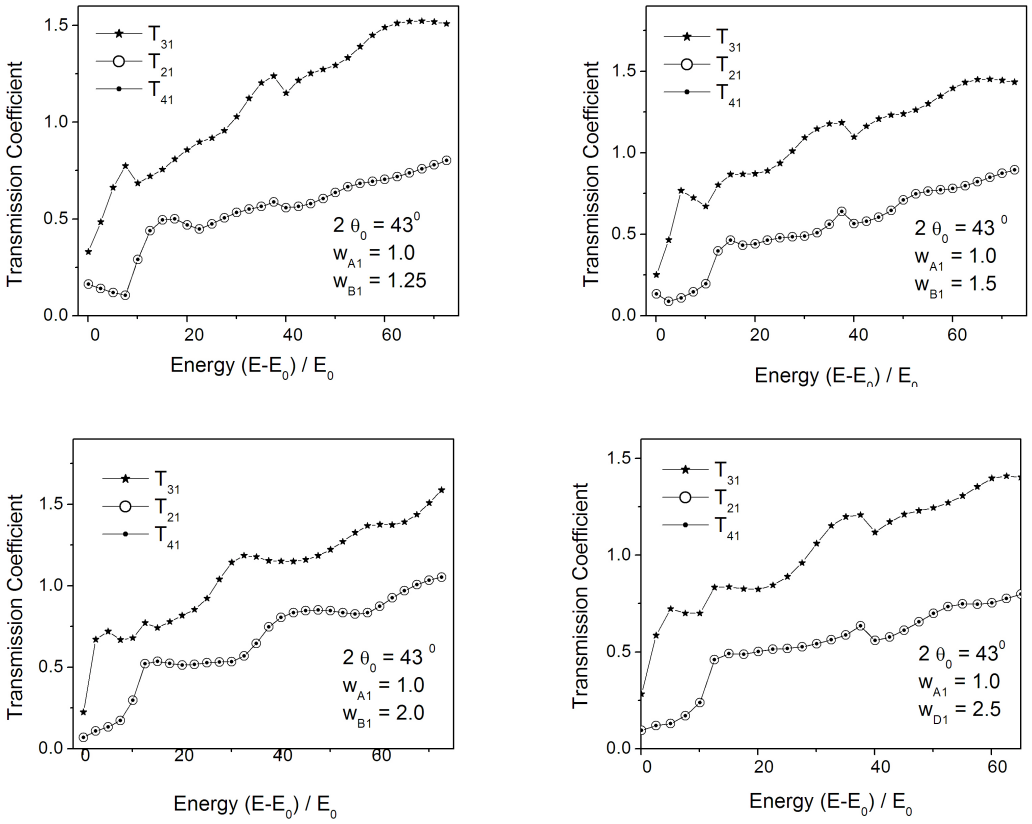

Figure 4.7: Transmission coefficients of electrons traveling in a 4-terminal wedge junction device. We use a symmetric wedge that all the four sides are similar. The opening angle of the wedge is kept constant that $2\theta_0 = 43^0$ and $w_{A1} = 1.0$. The transmission coefficients are plotted for devices with different values of w_{D1} as shown in the inset of each plot.

we will compare our results with. However for the experimental device $w_{D1} = 4.0$. We have not calculated the transmission coefficients for that specific device as it requires more basis functions for convergence. This is because the energy of the states is $\hbar^2\pi^2n^2/2m^*w_D^2$, so that large w_D requires a large quantum number n to reach the same energy.

4.5 Summary

Since the R-matrix connection formula is algebraically complicated, we here present a bulleted summary of the procedure as follows.

- Identify the interior scattering region.
- Break the interior scattering region into parts such that it can be recognized as a combination of simple geometries.
- Find a good set of variational basis functions for each of the interior region.
- Calculate the Bloch eigenfunction in each interior region.
- Calculate the $\mathcal{M}$ matrix elements, $\mathcal{M}_{q,n_q,p,n_p}$ for each q, n_q, p, n_p.
- Write down the R-matrix equation (eq.3.16) to relate the scattering wave function in each different region.
- Apply the boundary conditions at each internal boundary to eliminate the scattering wave function Ψ defined in the internal regions
- Simultaneously solve the resultant equations to find the unknown scattering amplitude
- Calculate the transmission coefficients from the scattering amplitudes according to the eq. (3.9).

4.6 Conclusions

We have developed a method to calculate the transmission coefficients of electron in a device with a complicated scattering region. However, one of the drawbacks for this technique is that we have not formed a generic expression like the one we have derived for two-dimensional single interior-region RMT (eq.3.29). We believe that

we can develop this formula and obtain a generic equation that can be deduced for different geometries which is not included in this thesis.

Chapter 5

Evaporative Cooling in Semiconductor Devices

5.1 Introduction

As electronic devices become smaller, they cross over between classical physics to quantum physics. Many classical quantities (eg.resistance) must be reinterpreted when they are examined on a mesoscopic level. One such classical concept is that of the refregirator - a device that uses an external source of work to cool a gas. It is interesting to ask if this classical concept can be applied to an electron gas so that by applying a voltage we get cooling in the system.

There are many ways to achieve electron cooling in condensed matter systems. For example, thermoelectric coolers based on the Peltier [23] effect are available commercially. A different kind of electron cooling mechanism in semiconductor devices is presented by G.Rego et.al [24] based on the quasi-static expansion of a two dimensional electron gas. Still other possibilities include taking advantage of many-body effects that can lead to liquid/gas phase transitions in the electron populations in semiconductor quantum wells [25].

In this chapter we investigate the theory of cooling electrons in solid state devices

via evaporative cooling. Evaporative cooling is the removal of the higher energy particles in a system and the subsequent relaxation of the remaining system to a temperature lower than the temperature of the initial system. Evaporative cooling is widely used in bosonic systems [26]. However it is harder to implement for fermionic systems, as we will discuss below. Our approach has simple analogs in classical refrigeration [27, 28] which is called the Hilsch vortex tube. A Hilsch vortex tube uses a T-shaped assembly of tubes to separate high pressure air into a higher and lower energy parts. A diagram of a Hilsch vortex tube is shown in the figure (5.1). A high pressure air is injected into the vortex from the side arm of the T-shaped assembly of tubes. Air molecules rotate around the vortex and the hot and cold parts are separated by this vortex. This process does not violate the second law of thermodynamics since the system is obviously driven by an external force.

We use the same concept to achieve cooling an electron gas system. A T-shaped assemble of quantum wires is used to separate high energy and low energy electrons. It should be noted that when the electron gas injected into the system, the total energy is same for all the electrons. However, since we use a 1-dimensional wire system, even

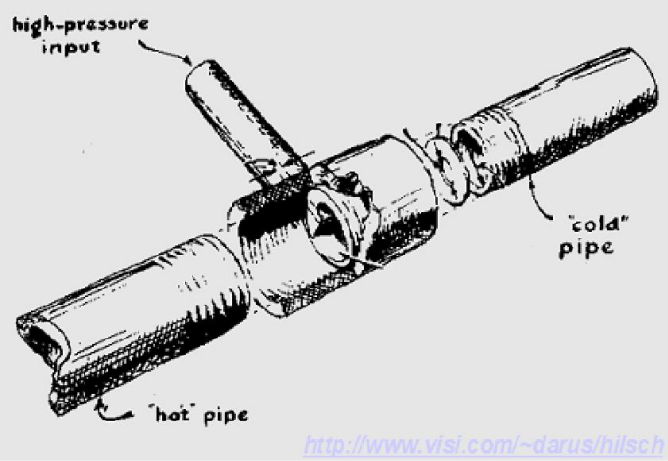

Figure 5.1: A schematic diagram of a T shaped assemble used in the Hilsch vortex tube. High pressure air is injected from the side arm and separated into cold and hot parts using the vortex operated in the middle of the T assembly.

though the total energy of the electrons is the same, the energy associated with the longitudinal direction or the kinetic energy of the system is different.

In this chapter we prove in principle that we can achieve cooling by the evaporative emission of the higher subband electrons from the system. This chapter is structured as follows. In section 5.2, we develop a theory and a simple design for the evaporative cooling of electrons via subband filtering in quantum wires. First we consider ideal subband filtering which means that we start with an equilibrium system of electrons and then all the second subband electrons are scattered from the system. Since the system is disturbed from the equilibrium, electrons rethermalize to a new equilibrium. Since the higher energy electrons are evaporated, the rest of the system will equilibrate at a lower temperature. We demonstrate this in the section (5.2).

In a real system, not all the higher subband electrons are evaporated from the system. Not all the lower subband electrons stay in the system. We use the Landauer formula (ch.1) to analyze the cooling characteristics of the system. The Landauer formula was originally developed to explain the transport properties of a quantum mechanical system. It describes how the transport properties of a quantum mechanical system relate to the transmission coefficients of electrons that pass through the system. We extend this idea to explain the cooling properties of a device. To get the transmission coefficients that the Landauer formula requires, we use a variational RMT, which we have developed in the chapter (3). We then examine several more realistic device geometries and discuss their cooling properties. Our calculations show that for naive designs we might get electron heating, and we discuss the reasons for this flaw. However, when we optimize the system we can get cooling. We conclude with a discussion of applications as well as realistic device parameters.

5.2 Theory: Ideal Model

We propose a theory for cooling which has a classical analog to the working principle of the Hilsch vortex tube. The Hilsch vortex tube uses a T-shaped assembly of pipes

to separate high pressure air into high temperature and low temperature systems. We apply a similar idea to cool electrons in a quantum mechanical system. A T-shaped assembly of a quantum wire configuration is used to evaporate high energy electrons out of the system. A schematic diagram of the proposed T shaped quantum wire configuration is shown in the figure (5.2).

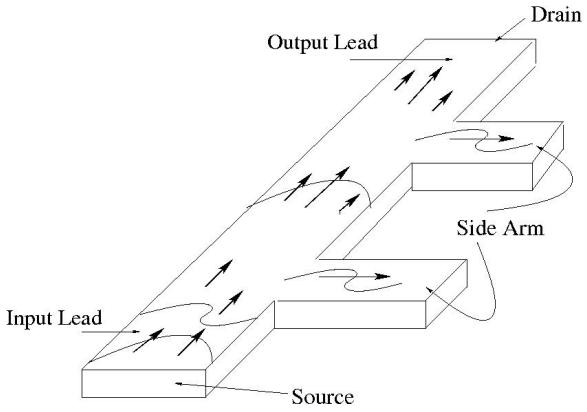

Figure 5.2: A schematic diagram of a T-shaped assemble of a quantum wire configuration. Electrons are injected from the source and they scatter into all the output leads. Since the equilibrium electron distribution is disturbed by scattering, they re-thermalize in the output leads. In the text, we show how to calculate the new equilibrium temperature for some systems with particular geometries and show that we can find some geometries and initial chemical potentials for which the final temperature is less than the initial temperature which means the cooling of the system.

Electrons are injected into the system from the source region where those electrons are in thermal equilibrium at a temperature, T_i and a chemical potential μ_i. These electrons scatter into all the output leads. Since the initial equilibrium electron system is disturbed by scattering, at the exit of the scattering region electrons are not in equilibrium and they re-thermalize in the output leads. Below we show how to calculate the new equilibrium temperature T_o and the new chemical potential, μ_o in the output lead. We denote the three leads as i, s and o which stand for the input lead, sidearm and the output lead respectively. In order to ease the explanation of the calculation, we divide the T-junction into parts as shown in the figure (5.3).

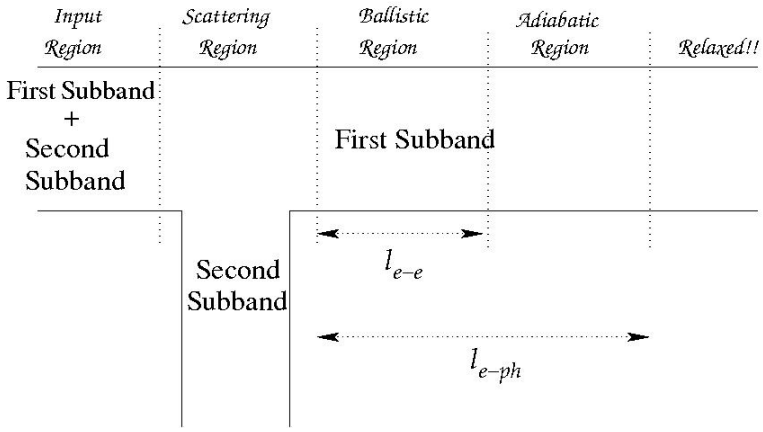

Figure 5.3: A quantum wire T junction device is divided into regions to explain the electron cooling behavior. Electrons are injected from the input region, and undergo scattering in the scattering region. In the ballistic region, electrons are not in equilibrium, and the electron population is determined by the product of incoming-electron distribution and the transmission coefficient. Electrons re-thermalize and come to an equilibrium in the adiabatic region; however, there is no relaxation with the phonons. In the text we show how to calculate this new equilibrium temperature and the new chemical potential.

In the input region, electrons are in thermal equilibrium at temperature T_i and chemical potential μ_i. All filtering occurs in the scattering region. Electrons scatter into the input lead (reflection), sidearm, and the output lead. We concentrate on the electrons scattering into the output lead. In the ballistic region, the electron population is entirely determined by the product of the incoming electron distribution and the transmission coefficient to the output lead. At this region, electrons are in a highly non-equilibrium state and cannot be characterized by a temperature and a chemical potential. In the adiabatic region, we consider only the internal relaxation of electronic distribution because by that time electrons have traveled a distance that is of the order of electron-electron relaxation length l_{e-e}. Usually this distance is shorter than the electron-phonon relaxation length, l_{e-ph}. In the internal relaxation of the electron distribution, there is no heat transfer from the phonons in the lattice; hence the term "adiabatic". Electrons will transfer heat among themselves and relax to a

different temperature T_o and a chemical potential μ_o. In principle, T_o and μ_o can be found using the particle and energy conservation. Our calculation shows that for some device geometries this equilibrium temperature T_o is less than the initial temperature T_i. This is the desired cooling effect. We characterize the cooling property by a dimensionless parameter $\eta = T_o/T_i$, where $\eta < 1$ means the cooling.

In order to understand the cooling phenomenon, we first discuss an *ideal* two subband model. We consider a T-shaped quantum mechanical device designed on the two-dimensional electron gas system. We assume that the width of the input quantum wire, w_i, is so small that the incoming electrons can only occupy the first subband or the second subband in the wire. In the *ideal* two band case, all of the electrons in the second subband scatter into the sidearm, whereas those in the first subband scatter forward to the output lead (fig.5.2).

The particle number and the energy are conserved between the ballistic region and the adiabatic region because there is no external field acting on the system. As we have explained earlier, the electron distribution in the ballistic region cannot be explained in terms of a temperature and a chemical potential since the electron distribution in the ballistic region is out of equilibrium. We can find the particle number in the ballistic region of the output lead as the product of the incoming electron distribution and the transmission coefficient of electrons from the input to output lead. We use the symbols $\mathbb{N}$ and $\mathbb{E}$ for the particle number and the energy. Since the electrons in the ballistic region are out of equilibrium, we will use the symbols $\mathbb{N}^{o,i}$ and $\mathbb{E}^{o,i}$ for the particle number and the energy in that region. The superscripts are to denote the transmitted electrons from the input lead (i) to the output lead (o). We use the symbols $\mathbb{N}^{\ell}$ and the $\mathbb{E}^{\ell}$ for the particle number and the energy of electrons associated with an equilibrium distribution in the ℓth lead.

Now we need to find out the total number of electrons and the energy associated with an equilibrium electron distribution in a lead ℓ. We need to consider each

subband. The density of electrons associated with the n_ℓ^{th} subband in each lead ℓ is,

$$\rho_{n_\ell}^{\ell}(E, \tau_\ell, \mu_\ell) \;=\; f(E, \tau_\ell, \mu_\ell)\mathcal{D}_{n_\ell}^{\ell}(E). \tag{5.1}$$

In this equation, the one dimensional (it is one-dimensional since two degrees of freedom are confined) density of states ($\mathcal{D}_E^\ell$) is given by [18],

$$\mathcal{D}_E^\ell = \Theta\left[E - \mathcal{E}_{n_\ell}^{\ell}\right]^{-1/2}, \tag{5.2}$$

where $\mathcal{E}_{n_\ell}^{\ell}$ is the energy of the n_ℓ^{th} subband of the ℓth lead which is given by $(n_\ell^2/w_\ell^2 - 1)$ in our dimensionless units. The step function Θ indicates that the n_ℓ^{th} subband is occupied only if the total energy is higher than the subband energy. In this chapter we scale all the lengths by w_i, the width of the input lead, and all the energies by $\mathcal{E}_0^i$, the first subband energy of the input lead, and we measure all the energies from the first subband energy. Note that in the other chapters we scale the energies by $\hbar^2/m^* w_i^2$, while in this chapter we have scaled the energy by $\hbar^2\pi^2/2m^* w_i^2$.

With these units, the energy, the chemical potential, and the temperature are scaled as,

$$E = \frac{\tilde{E} - \mathcal{E}_0^i}{\mathcal{E}_0^i}, \tag{5.3}$$

$$\mu = \frac{\tilde{\mu} - \mathcal{E}_0^i}{\mathcal{E}_0^i}, \tag{5.4}$$

and,

$$T = \frac{k\tilde{T}}{\mathcal{E}_0^i}, \tag{5.5}$$

where the tilded symbols are the dimensional quantities and the un-tilded quantities are dimensionless. In the equation (5.1), $f(E, \mu_\ell, T_\ell)$ is the Fermi-Dirac distribution function at a temperature T_ℓ and the chemical potential μ_ℓ which is given by,

$$f(E, \mu_\ell, T_\ell) = \frac{1}{1 + e^{\frac{E-\mu_\ell}{T_\ell}}}. \tag{5.6}$$

Now we can calculate the number of electrons and the energy associated with the n_ℓ^{th} subband in the ℓth lead as,

$$\mathbb{N}_{n_\ell}^{\ell}(T_\ell, \mu_\ell) = \int_{\mathcal{E}_{n_i}^i}^{\infty} \rho_{n_\ell}^{\ell}(E, T_\ell, \mu_\ell)\; dE, \tag{5.7}$$

and,

$$\mathbb{E}^{\ell}_{n_\ell}(T_\ell, \mu_\ell) = \int_{\mathcal{E}^i_{n_i}}^{\infty} \rho^{\ell}_{n_\ell}(E, T_\ell, \mu_\ell)\ E\ dE. \tag{5.8}$$

With this we can calculate the total number of electrons and the total energy associated with the electrons in the ℓth lead as,

$$\mathbb{N}^{\ell}(T_\ell, \mu_\ell) = \sum_{n_\ell=1}^{\infty} \mathbb{N}^{\ell}_{n_\ell}(T_\ell, \mu_\ell), \quad \text{and,} \quad \mathbb{E}^{\ell}(T_\ell, \mu_\ell) = \sum_{n_\ell=1}^{\infty} \mathbb{E}^{\ell}_{n_\ell}(T_\ell, \mu_\ell). \tag{5.9}$$

Now we will proceed the calculation for the ideal two-subband model. At the entrance to the conductor, the total number of electrons, $\mathbb{N}^i(\mu_i, T_i)$ is equal to the sum of the number of electrons in the first and second subbands. Similarly, the total energy, $\mathbb{E}^i(\mu_i, T_i)$ is equal to the sum of the energies of the electrons in first and second subbands. We write this as:

$$\mathbb{N}^i(\mu_i, T_i)\ = \mathbb{N}^i_1(\mu_i, T_i) + \mathbb{N}^i_2(\mu_i, T_i), \tag{5.10}$$

and,

$$\mathbb{E}^i(\mu_i, T_i)\ = \mathbb{E}^i_1(\mu_i, T_i) + \mathbb{E}^i_2(\mu_i, T_i). \tag{5.11}$$

We explicitly write the above equations, since it might help to understand the calculation more clearly, as,

$$\mathbb{N}^i(\mu_i, T_i) = \int_0^{\infty} \mathcal{D}^i_1(E) \frac{1}{1 + e^{\left(\frac{E-\mu_i}{T_i}\right)}} dE + \int_{\mathcal{E}^i_2}^{\infty} \mathcal{D}^i_2(E) \frac{1}{1 + e^{\left(\frac{E-\mu_i}{T_i}\right)}} dE\,, \tag{5.12}$$

and

$$\mathbb{E}^i(\mu_i, T_i) = \int_0^{\infty} E\,\mathcal{D}^i_1(E) \frac{1}{1 + e^{\left(\frac{E-\mu_i}{T_i}\right)}} dE + \int_{\mathcal{E}^i_2}^{\infty} E\,\mathcal{D}^i_2(E) \frac{1}{1 + e^{\left(\frac{E-\mu_i}{T_i}\right)}} dE\,. \tag{5.13}$$

where $\mathcal{D}^i_1(E)$ and $\mathcal{D}^i_2(E)$ are defined as,

$$\mathcal{D}^i_1(E) = E^{-1/2}, \tag{5.14}$$

and,

$$\mathcal{D}^i_2(E) = (E - 3\mathcal{E}^i_0)^{-1/2} \tag{5.15}$$

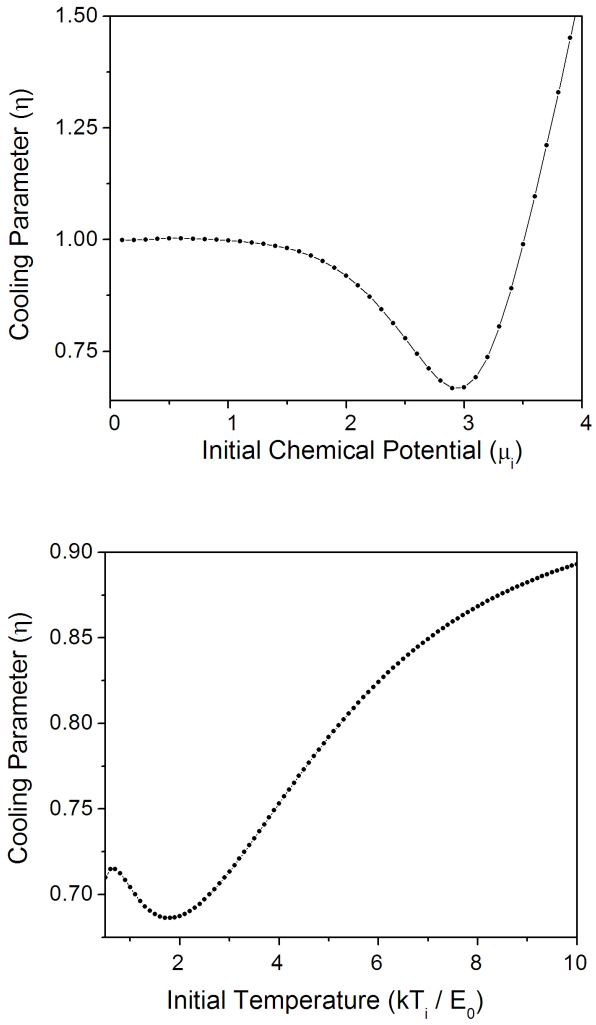

Figure 5.4: Upper plot is a graph of cooling parameter, $\eta = T_f/T_i$ as a function of the chemical potential μ_i. The initial temperature $T_i = 0.25$ for this calculation. This variation of η shows that, for some chemical potentials, $\eta \leq 1$, which means we get cooling. Also there is a significant minimum in the cooling parameter when $\mu_i = 3$; the reason for this behavior is explained in the text. The lower plot is the variation of the cooling parameter a function of the initial temperature, $T_i = k\tilde{T}_i/\mathcal{E}_0^i$. The initial chemical potential is kept at the edge of the second subband, which is the optimum value from the upper plot . This shows a maximum of 30% cooling.

since $\mathcal{E}_1^i = 0$ and $\mathcal{E}_2^i = 3\mathcal{E}_0^i$.

In the ideal model only the lower subband electrons $\mathbb{N}_1^i(\mu_i, T_i)$ scatter forward into the output lead. The total energy in the output lead after scattering is $\mathbb{E}_1^i(\mu_i, T_i)$. We mathematically write this as,

$$\mathbb{N}^{o,i} = \mathbb{N}_1^i(\mu_i, T_i), \tag{5.16}$$

and,

$$\mathbb{E}^{o,i} = \mathbb{E}_1^i(\mu_i, T_i). \tag{5.17}$$

Now the electrons are not in the equilibrium. These electrons will come to an equilibrium distribution as,

$$\mathbb{N}^o(\mu_o, T_o) = \mathbb{N}^{o,i}, \tag{5.18}$$

and,

$$\mathbb{E}^o(\mu_o, T_o) = \mathbb{E}^{o,i}. \tag{5.19}$$

We numerically solve the equations (5.18) and (5.19) along with the equations (5.16) and (5.17) at a fixed initial temperature for a range of values of the chemical potential. Figure (5.4) shows the variation of cooling parameter η as a function of the initial chemical potential μ_i when the initial temperature $T_i = 0.25$. Upper plot of the figure (5.4) shows that we get maximum cooling when the chemical potential, $\mu_i = 3$. Note that we work in units of the first subband energy and the energy is measured from the first subband energy. So the minimum of this plot corresponds to the edge of the second subband. At this chemical potential, electrons populate the higher subband only because they are thermally excited in that range thus all of the evaporated electrons are "hot" electrons. This gives the maximum cooling.

We repeat the above calculation at a fixed chemical potential which equals to the optimum chemical potential in the previous calculation. The lower plot of the figure (5.4) shows the variation of the cooling parameter η with the initial temperature τ_i. The graph (fig5.4) shows a maximum of 30% decrease in the temperature ($\eta \sim 70\%$).

5.3 Applications to Real Devices

To achieve optimum cooling, the higher subband electrons should scatter to the sidearm and the lower subband electrons should scatter forward into the output lead. In a real device not all the higher subband electrons scatter out of the system, and not all of the lower subband electrons will stay in the system. The scattering of electrons depends on the system properties such as the geometry and the scattering potentials. We consider pure samples in which we assume there are no scattering potentials and all the scattering of the system occur due to the boundaries. Even though the theory presented here has a flexibility to include a non-zero scattering potential, this present calculation considers zero potential energy in the device. We can alter the scattering of electrons in this system by changing the ratio of the width of the sidearm to that of the main lead (fig 5.2). The higher subband electrons scatter preferentially to the sidearm because they have a higher transverse momentum.

To calculate the cooling parameter η we need to know how the electrons scatter in the system. That is, we need to know the electron population in each subband which requires the transmission coefficients from state to state. To calculate the transmission coefficients of the system, we use variational RMT which we have discussed in the chapter (3). We first present the calculation of the cooling parameter in general and then apply it to some devices.

In the earlier section we showed how to calculate the cooling parameter in an *ideal* device. The procedure is the same for a real device, however, in order to calculate the electron and the energy density in the ballistic region, we need to use the transmission coefficients.

Now we have to change the equations to calculate the electron population and the energy density in the output lead using the transmission coefficients. In particular, the equations (5.16) and (5.17) do not hold for the real device. We can write the density of electrons transmitted from the subband n_i of the ith lead into the subband

n_ℓ of the ℓth as,

$$\rho^{\ell,i}_{n_\ell,n_i}(E,T_i,\mu_i) = \rho^{i}_{n_i}(E,T_i\mu_i)\ \mathcal{T}^{\ell,i}_{n_\ell,n_i}(E). \tag{5.20}$$

With this we can calculate the number of electrons from all the subbands in the input lead into all the subbands in the lead ℓ as,

$$\mathbb{N}^{\ell,i} = \sum_{n_\ell=1}^{\infty}\sum_{n_i=1}^{\infty}\int_{\mathcal{E}^{\max}_{\ell,i}}^{\infty} \rho^{\ell,i}_{n_\ell,n_i}(E,T_i,\mu_i)\,dE, \tag{5.21}$$

where the lower limit of the integration,

$$\mathcal{E}^{\max}_{\ell,i} = \max\left\{\mathcal{E}^{i}_{n_i},\mathcal{E}^{\ell}_{n_\ell}\right\} \tag{5.22}$$

ensures that both the incoming and outgoing subbands are open.

In the similar way we can calculate the energy of the electrons in the ballistic region of the lead ℓ as,

$$\mathbb{E}^{\ell,i} = \sum_{n_\ell=1}^{\infty}\sum_{n_i=1}^{\infty}\int_{\mathcal{E}^{\max}_{n_{\ell,i}}}^{\infty} \rho^{\ell,i}_{n_\ell,n_i}(E,T_i,\mu_i)\,E\,dE. \tag{5.23}$$

Now this amount of electrons and the energy is redistributed in the adiabatic region of the output lead and we can simultaneously solve the equations (5.18) and (5.19) along with the equations (5.21) and (5.23) to find the T_ℓ and μ_ℓ. We are interested in the equilibrium quantities in the output lead that $\ell \to o$.

5.3.1 T-junction as a Cooling Device

We calculate the cooling parameter η using the real transmission coefficients in the T junction device for certain ratios of the widths of the sidearm, w_s and the input lead, w_i, We always keep the width of the input lead, w_i equal to the width of the output the lead, w_o. We use the equations developed in the chapter (3) for solving the transmission coefficients of electrons in the T-junction device. In the equation (3.29), electrons are injected from the lead p_0 that for our present problem $p_0 = i$

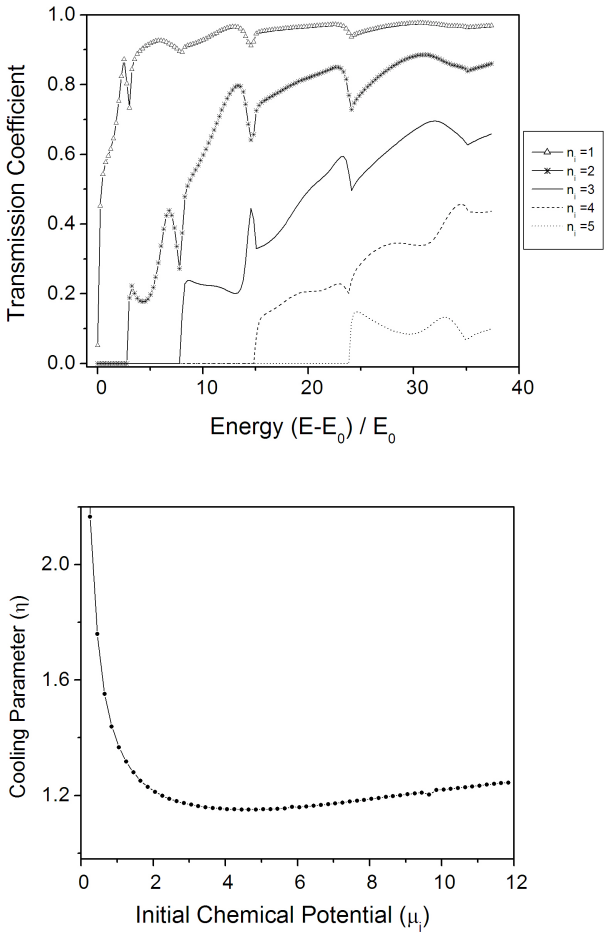

Figure 5.5: The upper plot is the transmission coefficients of electrons to the output lead in a T-junction device with $w_i = w_s = w_o = 1$. The different curves are for different subband index of the incoming electron. The x axis is the energy of the incoming electron which is measured in terms of $\mathcal{E}_0^i = \hbar^2\pi^2/2m^*w_i^2$ and is measured from $\mathcal{E}_0^i$. We calculate the cooling parameter using these transmission coefficients. Since there are some higher subband electrons lost from the input distribution, we expect $\eta < 1$. This graph shows that the cooling parameter $\eta > 1$ which means $T_o > T_i$. Even though we lose higher subband electrons from the system, it does not achieve cooling.

T-junction Device with $w_s = w_i = 1.0$

First we will consider a T-junction devices where $w_i = w_s = w_o = 1.0$. The transmission coefficients for such a T-junction device are shown in the figure (5.5).

The graph (5.5) shows the transmission coefficients of electron into the output lead when the electron is in different subbands in the incoming lead. This graph shows that there are some higher subband electrons lost from the input distribution. According to the *ideal* model we discussed, we would expect $\eta < 1$ for this device.

The cooling parameter is calculated for different values of initial temperatures keeping the initial chemical potential $\mu_i = 0$. Note that we measure the energy in terms of $\mathcal{E}_0^i$, and all the energies are measured from $\mathcal{E}_0^i$. So $\mu_i = 0$ means that the external potential of the system is set such that the Fermi energy, $E_F = \hbar^2\pi^2/2m^*w_i^2$. The lower plot of the figure (5.5) shows the cooling parameter for this device as a function of the initial temperature. This graph shows that for all the initial temperatures the cooling parameter $\eta > 1$. We do not get cooling as we expected, instead these transmission coefficients result in heating. The reasons for this flaw can be explained as follows.

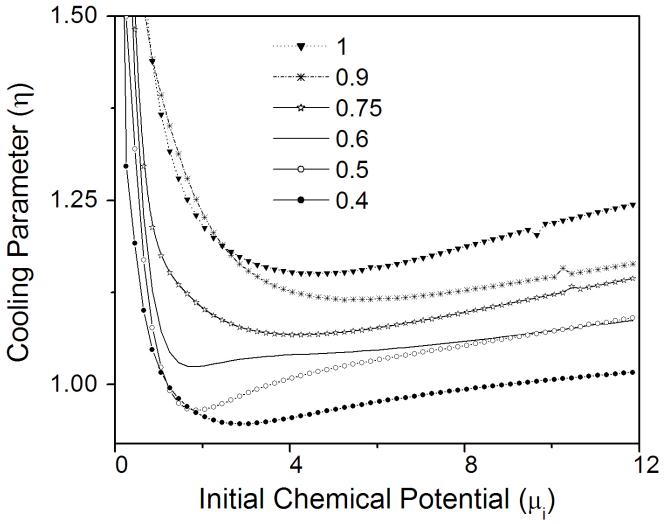

Figure 5.6: The cooling parameter η as a function of the initial temperature T_i when the initial chemical potential $\mu_i = 0$ for different w_i values. This graph shows that the cooling parameter η is always larger than 1 for some w_s values and $\eta < 1$ for some w_s values. This says that by changing the transmission coefficients we can change the cooling parameter.

Losing high energy electrons can produce cooling. But losing the low energy electrons heats the system. The loss of low energy electrons opens gaps in the electron population at low energies in the electron distribution. The higher energy electrons can then relax to low energy states liberating the energy difference as thermal energy. Thus losing low energy electrons heats the system. Even if the distribution has a small dip at low energies, it will have large effect in the final temperature. The naive T junction does not produce cooling.

Different T-junction Geometries

We alter the T-junction geometry by changing the width of the sidearm, w_s. The transmission coefficients are calculated using the variational RMT and the cooling

w_s	μ_i	T_i	T_o	μ_o	η
1.0	0.0	4.65	5.35	-6.24	1.15
	3.0	5.85	7.06	-5.63	1.21
	6.0	6.77	8.69	-5.06	1.28
0.9	0.0	5.68	6.34	-6.27	1.11
	3.0	6.52	7.58	-4.97	1.16
	6.0	7.63	9.33	-4.31	1.22
0.75	0.0	4.18	4.463	-3.68	1.07
	3.0	5.36	6.01	-2.58	1.22
	6.0	6.59	7.84	-1.80	1.19
0.6	0.0	1.79	1.84	-1.09	1.02
	3.0	6.00	6.53	-1.84	1.09
	6.0	7.39	8.40	-0.77	1.14
0.5	0.0	1.85	1.79	-0.75	0.96
	3.0	3.62	3.86	0.38	1.06
	6.0	6.52	7.35	0.58	1.13
0.4	0.0	2.89	2.73	-0.71	0.95
	3.0	3.28	3.25	1.54	0.99
	6.0	5.47	5.74	2.75	1.05

Table 5.1: The cooling parameter of the T-junction with different width of the sidearm. We have also tabulated the input chemical potential, output chemical potential and output temperature at the maximum cooling parameter.

parameter is calculated as discussed above. We tabulate the minimum cooling parameter for T junctions with different width of the sidearm. The table (5.1) shows the initial and final chemical potentials (μ_i and μ_o), the initial and final temperatures (T_i and T_o) at the maximum cooling parameter, η for different widths of the sidearm, w_s.

We can see that as we change the geometry, the cooling parameter changes. The graph (fig.5.6) shows the variation of η vs. the initial temperature T_i when the initial chemical potential $\mu_i = 0$ for T-junction devices with different widths of the sidearm, w_s as shown in the inset of the figure. These results show that we can achieve $\eta < 1$ for some T-geometries and $\eta > 1$ for some other geometries. The only difference for these geometries is that they have different transmission coefficients. That means by changing the scattering in the device we can achieve cooling. The device with $w_s = 0.4$ gives around 0.05% of cooling. Following we show the details for the device with $w_s = 0.4$.

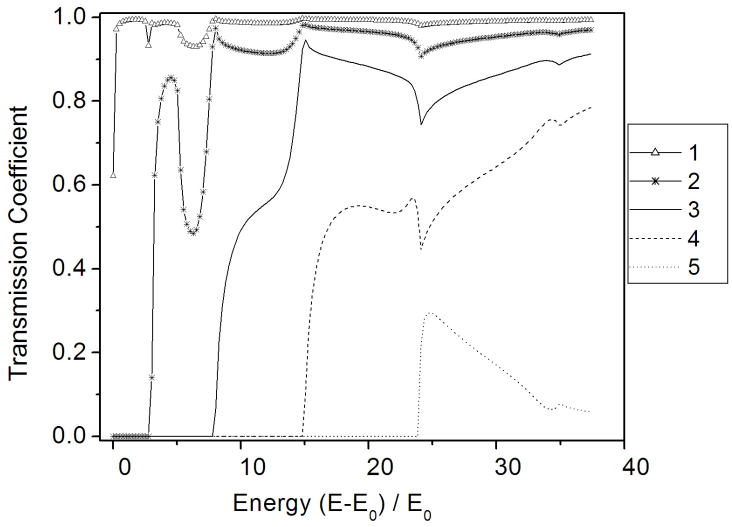

Figure 5.7: The state to state transmission coefficients of electrons to the output lead in a T-junction device with $w_i = w_o = 1.0$ and $w_s = 0.4$. The data in table (5.1) shows that this transmission coefficients gives 0.05% of cooling.

T-junction Device with $w_s = 0.4$

The graph (fig.5.7) shows the state to lead transmission coefficients of electrons in the T-junction device with $w_s = 0.4$. The different curves are for the electrons in different incoming subbands.

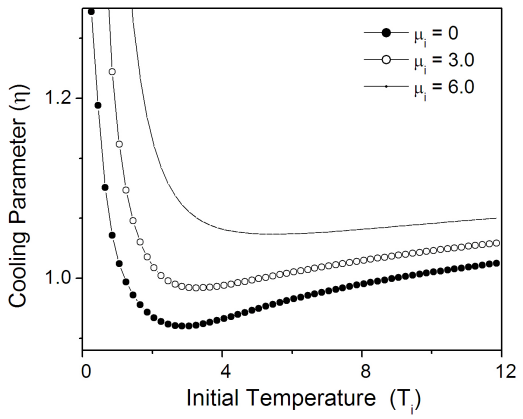

Figure 5.8: The cooling parameter as a function of the initial temperature for the T-junction device with $w_i = w_o = 1.0$ and $w_s = 0.4$. We calculate the cooling parameter using the transmission coefficients shown in the figure (5.7) at different initial chemical potentials, $\mu_i = 0.0, 3.0, 6.0$. The results show that we achieve the best cooling when $\mu_i = 0$.

Using the transmission coefficients as shown in the figure, we calculate the cooling parameter for the device. The graph (fig.5.8) shows the variation of the cooling parameter as a function of the initial temperature for three different initial chemical potentials, $\mu_i = 0.0, 3.0, 6.0$. This graph shows that we get maximum cooling when the initial chemical potential equals to 0. At this chemical potential all of the lost electrons were in the thermally activated region of the Fermi Distribution. Even though, we get cooling from the T-junction with $w_s = 0.4$, the maximum cooling is at $\eta = 0.95\%$. This certainly proves the principle that we can achieve cooling. However it is not enough to make experimental devices. We change the device geometry to a plus junction device and calculate the cooling parameter, η.

5.3.2 Plus Junction as a Cooling Device

Since the cooling we achieve with the T-junction device was not very significant, we try other geometries as cooling devices. Here we try a device with a plus junction as shown in the figure (3.6). Since we achieve cooling with $w_s = 0.4$ in the T-junction device, we use a plus junction with $w_1 = w_3 = 1.0$ and $w_2 = w_4 = 0.4$. The

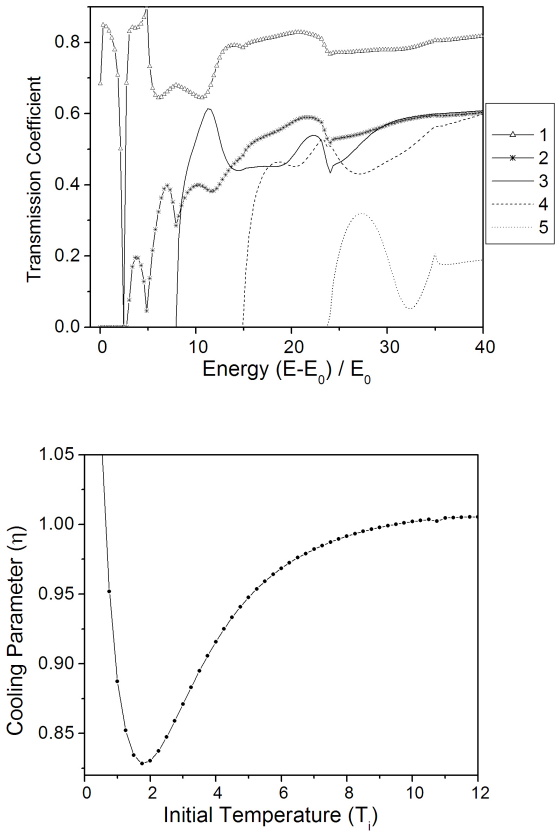

Figure 5.9: Upper plot is the transmission coefficients of electrons to the output lead in a plus-junction device with $w_2 = 0.4$. The different curves are for different subband index of the incoming electron. The x axis is the energy of the incoming electron which is measured in terms of $\mathcal{E}_0^1 = \hbar^2\pi^2/2m^*w_1^2$ and is measured from $\mathcal{E}_0^1$. We calculate the cooling parameter using these transmission coefficients and the result is shown in the lower plot. It shows $\eta \sim 0.85$ which means more than 15% of cooling.

transmission coefficients for this device is shown in the upper plot of the figure (5.9) and the resultant cooling parameter as a function of the initial temperature is shown in the lower plot of the figure (5.9).

The graph (fig.5.9) shows around 15% of cooling. This is a single unit of plus junction. The cooling can be further enhanced by cascading these units together.

In order to summarize the cooling devices we discussed, we plot the cooling parameter for three different devices together. The graph (5.10) shows the variation of the cooling parameter, η as a function of the initial temperature T_i keeping the initial chemical potential $\mu_i = 0$.

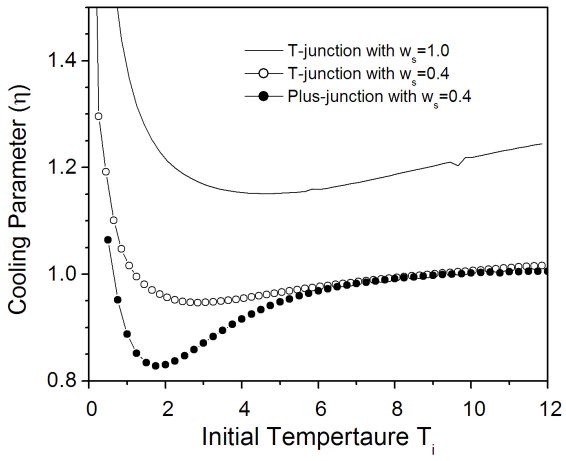

Figure 5.10: This graph shows a summary of the cooling calculations we have done in this chapter. The solid line is the cooling parameter for the T-junction device with $w_i = w_s = w_o = 1.0$, open dots are the cooling parameter for the T-junction device with $w_i = w_o = 1.0$ and $w_s = 0.4$. The solid dots are for the plus junction device with $w_1 = w_3 = 1.0$ and $w_2 = w_4 = 0.4$. All the calculations are done when the initial chemical potential $\mu_i = 0$.

In the following section, we calculate the experimental device parameters for Insb and GaAs for the optimum cooling properties we have obtained with the plus junction device.

5.4 Considerations for experiment

As it was explained earlier, we have done all the calculations in dimensionless units. In this section, we convert our results to real units and present the parameters for the cooling devices with two materials, InSb and GaAs.

All the material properties depend on the Fermi energy, E_F of the system. The Fermi energy E_F is inversely proportional to the effective mass of the electrons in the material and is set by the density of electron in the electron reservoir (see appendix B). For our device we set the initial chemical potential (which is approximately the Fermi energy) equal to zero. Since we have scaled the energy in the problem by $\mathcal{E}_0^i$ and measured from the $\mathcal{E}_0^i$, the initial chemical potential equals zero means that,

$$\mu_i = E_F = \frac{\hbar^2 \pi^2}{2m^* w_i^2}, \tag{5.24}$$

where w_i is the width of the input lead of our quantum wire plus-junction device shown in the figure (3.6). The condition (eq.5.24) allows us to determine the width of the quantum wire as a function of the electron density.

Different materials are characterized by the effective mass of electrons in the system. The condition to calculate the width of the wire is given by equation (5.24). In the appendix we have shown that the Fermi energy is inversely proportional to the effective mass of electrons. Since both the Fermi energy and the subband energy depend on the effective mass in the same fashion, the width of the quantum wire in our device is independent of the material.

If we assume a sample with the density of electrons is n, we combine the equation (5.24) with the equation (B.4) as,

$$\frac{\pi \hbar^2}{m^*}\, n \;=\; \frac{\hbar^2 \pi^2}{2m^* w_i^2}, \tag{5.25}$$

which gives the width of our quantum wire as,

$$w_i \;=\; \sqrt{\frac{\pi}{2\,n}}. \tag{5.26}$$

For instance, if we assume $n = 1.0 \times 10^{11}\text{cm}^{-2}$, $w_i = 39.6\,\text{nm}$. This is quite a small value. However, lowering the density of electrons makes the device larger.

We get maximum cooling with the plus junction when the initial temperature ~ 2 in the dimensionless units. We will convert the dimensionless temperature back to the real temperature using the equation (5.5). That is, at the optimum temperature T_{opt},

$$k\tilde{T} = T_{\text{opt}}\ \mathcal{E}_0^1. \tag{5.27}$$

With the equation (5.24), this reduces to,

$$k\tilde{T} = T_{\text{opt}}\, E_F. \tag{5.28}$$

In the appendix (B), we calculated the Fermi energy for InSb and GaAs (eq.B.5 and B.6). We obtain the initial temperature of the system at the optimum cooling parameter (for a sample with $n = 1.0 \times 10^{11}\text{cm}^{-2}$) as, $T \sim 82K$ for GaAs and $T \sim 399K$ for InSb. Room temperature, (300K) corresponds to $T \sim 1.5$ for InSb, allowing substantial cooling due to quantum effects in a room temperature device. Even a cooling parameter $\eta \sim 0.9$ means that the electron population would be cooled by $30K$. This would be useful to produce a population of electrons that could then be used for photo detection of frequencies near room temperature.

The above results also only have one unit of a cooling device. If multiple plus-junctions are connected in series, we may be able to get greater cooling.

5.5 Conclusions

A variety of photo detection applications require a cold detector. We have presented a prototype device which cools electrons in a single particle picture. Such a device could be used to cool the photo detection electron population. We have shown that while a naive design produces heating, by a slight change in geometry we can get cooling of at least 10%. Future studies will allow this to be maximized.

Chapter 6

Magneto-Transport Properties in Semiconductor Devices

In the introduction we discussed the existence of interesting magneto-transport properties such as negative bend resistance (NBR) and the quantum Hall effect in two-dimensional devices. NBR is a signature of ballistic electron transport in two-dimensional devices and has been observed in different materials such as InSb [10] and GaAs [29]. In this chapter we will discuss how to calculate the bend resistance of a two-dimensional four-terminal device. This research is motivated by the experimental observation of NBR in two-dimensional InSb devices by Goel et.al [10] at the University of Oklahoma.

In previous chapters we learned that the transport properties of a quantum mechanical device can be studied as a scattering problem according to Landauer theory. The Landauer-Bütikker [13] formula is still valid for magneto-transport. The LB formula requires the transmission coefficients from one lead to another in the device. Sometimes these transmission coefficients, (i.e. the probabilities) are calculated using a classical billiard ball model [30] in the case of ballistic transport which is called the semi-classical model. However, as we will explain below, the effective mass is very small for InSb so that only a few quantum channels are occupied in the narrow InSb

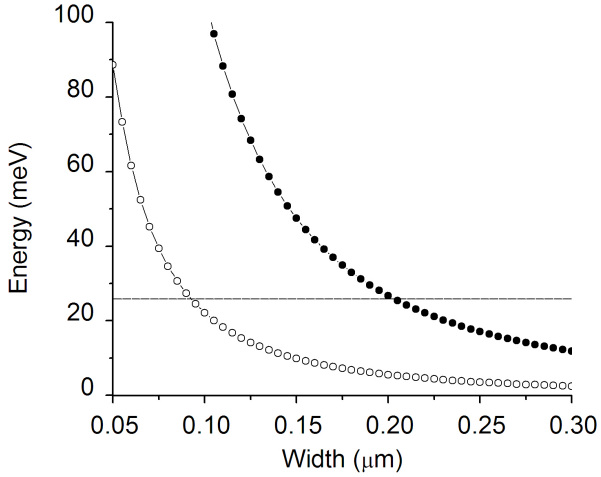

Figure 6.1: The unit of quantum confinement energy, $\hbar^2\pi^2/2m^*w^2$ as a function of the well width, w. The solid dots are for InSb and the empty dots are for GaAs. The straight line is the room temperature thermal energy.

devices (see appendix B).

The effective mass of InSb is very small ($m^* = 0.0139 \times m_0$, where m_0 is the free electron mass) so that the confinement energy of InSb is larger than the other $III-V$ semiconductors for comperable size structures. The figure (6.1) shows the variation of confinement energy, ($\hbar^2\pi^2/2m^*w^2$, where w is the width of the sample in the confined direction) as a function of the width of the quantum well, w. The solid dots are for InSb and the empty dots are for GaAs. The straight line is the room temperature thermal energy, kT_0 where we use $T_0 = 300K$. It shows that the confinement energy of InSb is larger than that of GaAs. We will consider devices that have feature size in the order of $< 0.2\mu$m so that the quantum confinement energy is comparable to the thermal energy. In such a device only a few quantum channels are occupied. Since the effective mass is small, the energy gap between two adjacent quantum levels are large compared to that of other $III - V$ semiconductors. Actually these devices are on the border between quantum and classical limits. It is not clear which way

the device transport will behave. In order to understand the device properties, it is very important to treat the transport of the devices both quantum mechanically and classically. Then only we can decide whether the transport properties are due to the classical effects or quantum mechanical effects. This understanding is very useful to improve experimental features. Our goal in this chapter is to model the transport properties of these devices in a quantum mechanical fashion.

We will again use RMT to calculate the transmission coefficients. In the previous chapters, we discussed RMT for two-dimensional devices with no external magnetic field. In this chapter, we extend this technique to calculate the transmission coefficients of electrons in two-dimensional devices in the presence of a magnetic field. This chapter is structured as follows:

First we will recall some aspects of magneto-transport in semiconductor devices. We will also briefly explain the details of the experiment we are going to model as it was carried out by Goel et. al. [10].

In the section (6.2), we explain the basics of the magnetic-field RMT. We introduce a new Bloch operator and explain how to set up the equations to solve for the unknown scattering amplitudes which will give the transmission coefficients of the electrons in the system. Then in section (6.3), we apply the magnetic-field RMT to calculate the transmission coefficients in a 4-terminal device. An image of such a device is shown in the figure (6.2) [32]. We show the transmission coefficients and the resultant magneto-transport properties of this 4-terminal square junction device.

As we have discussed in the chapter (4), for some experimental devices the interior region is not very simple and it is hard to calculate the interior region Bloch eigenfunctions. An image of the device we are concentrated on is shown in figure (6.3) and sketched in figure (4.5). Since the interior region of this device is not simple, we need the connection formula to calculate the transmission coefficients in such a device. We did this exact problem with no external magnetic field in the section (4.4). In section (6.4), we discuss the application of magnetic-field RMT with the connection formula

and show the results of the magneto-transport properties of 4-terminal devices with wedge geometries (fig.6.3).

In calculating the transport properties as discussed above, we assume the zero temperature limit. In the section (6.5), we discuss the effect of finite temperature on the transport properties as we discussed in the section (1.1.1).

Finally we draw some conclusions related to experiments.

6.1 Magneto-Transport Properties of Electrons in Two-Dimensional Devices

First we will consider a two-dimensional electron gas in a magnetic field. In the classical limit, electron transport in a magnetic field shows the classical Hall effect which creates a transverse voltage drop for an applied longitudinal bias voltage [18]. The same sort of observation was made in the two-dimensional electron gas at high temperature. However many features show interesting quantized effects at low temperature due to the confinement in the growth direction. When there is a magnetic field, the electrons are deflected by the Lorentz force. In the two-dimensions the electron's path is circular. In the quantum limit the same thing happens, however only certain radii will be allowed. That is because when there is a magnetic field, the potential can be represented as a simple harmonic potential where the electron energies are given by the discrete Landau levels. Only orbits with the Landau energies are allowed.

The density of states of a two-dimensional electron gas (at zero field) is a constant as you change the energy. When there is an external field, the density of states will fall into a discrete set of delta functions located at $(n + 1/2)\hbar\omega_c$, where $\omega_c = eB/c$ is the cyclotron frequency and n is the Landau level index. The spacing between any two adjacent energy levels is equal. In the simplest picture, this discrete density of states give rise to the quantum Hall effect, Shubinikov De Haas oscillations etc. For

a complete explanation of these quantized effects, one should take the delocalization of these delta function states in to account. This field has been widely studied [34] and we will not discuss about these effects further in this thesis. We concentrate on the devices designed on the two-dimensional electron gas instead.

In these devices electron motion is further confined in the lateral direction in addition to the growth direction. The electron motion is confined by lithographically designed insulating layers. In this model we treat these lithographic boundaries as hard wall potentials even though this may not be the experimental case. The Landau level discreteness does not exist in these devices because of the hard wall boundary conditions. When the cyclotron radius is larger than the width of the lead, those Landau levels cannot exist in the system. However when the magnetic field is so large that the cyclotron radius is smaller than the width of the lead, Landau levels start to appear. Shubinikov De Haas like oscillations have been observed in such devices at a large magnetic field [31].

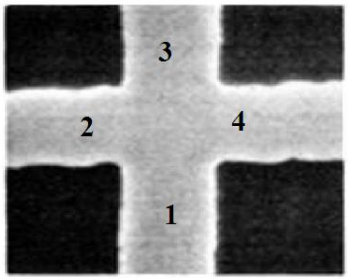

Figure 6.2: An image of a typical 4-terminal device [32]. The interior region of this device is square-shaped and all the outgoing leads are rectangular. A sketch of this figure with the coordinates used for the calculation is shown in the figure (3.6). In the text we explain how to calculate the transmission coefficients of electrons in such a device.

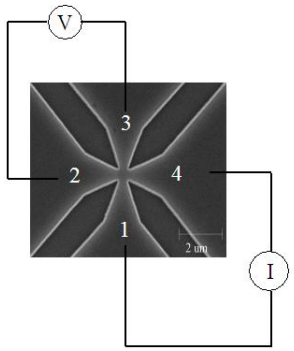

Figure 6.3: An image of the 4-terminal device designed on InSb quantum well used for the bend resistance experiment [10]. In the bend resistance experiment, a current I_{14} is injected from lead 4 to lead 1 and the voltage created between the leads 2 and 3, V_{23} is measured. The bend resistance, $R_B = V_{23}/I_{14}$ is measured. The experiment is done in the presence of a perpendicular magnetic field. Goel et. al has reported a negative bend resistance as shown in the figure (6.7). This is a signature of the ballistic transport. In the text we explain how to calculate the bend resistance of such a device.

We are particularly interested in the following experimental observation made on bend resistance, R_B in InSb 4-terminal devices. A typical four-terminal device has a 4-terminal square geometry as shown in the figure (6.2) [32]. This geometry is similar to the geometry we studied with no magnetic field which is sketched in the figure (3.6). The device of Goel et. al has a 4-terminal wedge geometry (fig.6.3) [11] which is sketched in the figure (4.5).

In the bend resistance experiment, a current I_{14} is injected from lead 4 to lead 1. The voltage created between the lead 2 and lead 3, V_{23} with respect to the injected current, I_{14} is measured. The bend resistance is defined as,

$$R_B = \frac{V_{23}}{I_{14}}. \tag{6.1}$$

There is an applied magnetic field, B perpendicular to the device. The bend resistance, R_B is measured as a function of the applied magnetic field, B. Goel et. al has

reported a negetive bend resistance at zero magnetic field [10]. If the electrons travel ballistically, they will tend to overshoot lead 1 and travel to lead 4. This contains with a charge accumulation in lead 2 giving a negative voltage. A magnetic field deflects charge into lead 2 decreasing this voltage.

Our goal in this chapter is to model this experimental result. We develop a method in general so that it can be applied to study the magneto-transport properties in general. It is easy to model the device in the figure (6.2) than the device sketched in the figure (6.3). We first explain the technique for modeling the 4-terminal square junction device and then we show how to extend the technique for complicated geometries. At the end of this chapter, after explaining all the computational details, we will show the results of magneto transport properties of a 4-terminal square device and a 4-terminal wedge device.

6.2 Two-Dimensional R-Matrix Formula with an Applied Perpendicular Magnetic Field

The notations in this section is similar to that of the zero-field RMT and we will note when it is different.

We start with the time-independent Schrodinger equation for a single electron in an applied perpendicular magnetic field,

$$\hat{\mathcal{H}} \left| \Psi_{E,n_{p_0}} \right\rangle = E \left| \Psi_{E,n_{p_0}} \right\rangle, \tag{6.2}$$

where $\left| \Psi_{E,n_{p_0}} \right\rangle$ is the scattering wave function. The subscript E is the total energy and n_{p_0} denotes the quantum number of the incoming electron in the lead p_0. The Hamiltonian $\hat{\mathcal{H}}$ is given by,

$$\hat{\mathcal{H}} = -\frac{\hbar^2}{2m^*}(\vec{P} - e\vec{A})^2 + V(\vec{r}), \tag{6.3}$$

where $\vec{A}$ is the vector potential. We have chosen $V(\vec{r}) = 0$ inside the device.

We will first make the Hamiltonian dimensionless. We measure the lengths in terms of a characteristic length in the device (typically we choose w_0, the width of the input lead), and energies in terms of $E_0 = \hbar^2/m^* w_0^2$ and define $\epsilon = E/E_0$ and $l_B^2 = \hbar/eB$. This new quantity, l_B has the units of length and is called the magnetic length of the system. The magnetic length, l_B is the average radius of the lowest Landau level of the system.

With this notation, the Schrodinger equation (eq.6.2) becomes,

$$\left[-\frac{1}{2}\left(\frac{\partial^2}{\partial x^2}+\frac{\partial^2}{\partial y^2}\right)+\frac{i}{B}\frac{w_0^2}{l_B^2}A_x\frac{\partial}{\partial x}+\frac{i}{B}\frac{w_0^2}{l_B^2}A_y\frac{\partial}{\partial y}+\frac{1}{2B^2}\frac{w_0^2}{l_B^2}\left(A_x^2+A_y^2\right)\right]\left|\Psi_{E,n_{p_0}}\right\rangle=\epsilon\left|\Psi_{E,n_{p_0}}\right\rangle, \tag{6.4}$$

where x and y are the dimensionless coordinates. Now we perform the calculation with two different gauges, the symmetric gauge, $\vec{A}^{\text{symm}} = (-By/2, Bx/2, 0)$ and the asymmetric gauge, $\vec{A}^{\text{asymm}} = (-By, 0, 0)$. With the symmetric gauge, the equation (6.4) becomes,

$$\left[-\frac{1}{2}\left(\frac{\partial^2}{\partial x^2}+\frac{\partial^2}{\partial y^2}\right)-\frac{iy}{2}\frac{w_0^2}{l_B^2}\frac{\partial}{\partial x}+\frac{ix}{2}\frac{w_0^2}{l_B^2}\frac{\partial}{\partial y}+\frac{1}{8}\frac{w_0^4}{l_B^4}\left(x^2+y^2\right)\right]\left|\Psi_{E,n_{p_0}}\right\rangle=\epsilon\left|\Psi_{E,n_{p_0}}\right\rangle. \tag{6.5}$$

With the asymmetric gauge, the equation (6.4) becomes,

$$\left[-\frac{1}{2}\left(\frac{\partial^2}{\partial x^2}+\frac{\partial^2}{\partial y^2}\right)-iy\frac{w_0^2}{l_B^2}\frac{\partial}{\partial x}+\frac{1}{2}\frac{w_0^4}{l_B^4}y^2\right]\left|\Psi_{E,n_{p_0}}\right\rangle=\epsilon\left|\Psi_{E,n_{p_0}}\right\rangle. \tag{6.6}$$

Note that the quantity w_0^2/l_B^2 is dimensionless and it is a measure of the strength of the magnetic field, B [35]. Hereafter we use the notation, $\mathcal{B} = w_0^2/l_B^2$ which further simplifies the above equations. The Schrodinger equation with the symmetric gauge (eq.6.5) becomes,

$$\left[-\frac{1}{2}\left(\frac{\partial^2}{\partial x^2}+\frac{\partial^2}{\partial y^2}\right)-\frac{iy}{2}\mathcal{B}\frac{\partial}{\partial x}+\frac{ix}{2}\mathcal{B}\frac{\partial}{\partial y}+\frac{\mathcal{B}^2}{8}\left(x^2+y^2\right)\right]\left|\Psi_{E,n_{p_0}}\right\rangle=\epsilon\left|\Psi_{E,n_{p_0}}\right\rangle, \tag{6.7}$$

and the Schrodinger equation with the asymmetric gauge (eq.6.6) becomes,

$$\left[-\frac{1}{2}\left(\frac{\partial^2}{\partial x^2}+\frac{\partial^2}{\partial y^2}\right)-i\mathcal{B}y\frac{\partial}{\partial x}+\frac{\mathcal{B}^2}{2}y^2\right]\left|\Psi_{E,n_{p_0}}\right\rangle=\epsilon\left|\Psi_{E,n_{p_0}}\right\rangle. \tag{6.8}$$

Both these equations, eq.(6.7) and eq.(6.8) have the same mathematical meaning, however choice of the gauge is important when we solve the problem approximately. We have to choose the gauge such that the solution will satisfy the boundary conditions of the system. An appropriate choice of gauge will achieve faster convergence of the results.

In solving the magnetic scattering problem, similar to what we did in the zero-field problem, we divide the system into two parts, the interior scattering region and the leads and then match the two solutions on the soft boundaries to solve for the transmission coefficients. We choose the symmetric gauge (eq.6.7) for the interior region. The asymmetric gauge (eq.6.8) is convenient for the leads as it correctly reduces the problem to give a traveling wave solution in the longitudinal direction [40]. As we described in the zero field RMT, since we use the solutions of equations (6.7) or (6.8) as a set of basis functions to expand the final scattering wave function, we do not need to transform the gauges from one region to the other. In the following sections we consider these two solutions, the interior region and the lead solutions, and develop the necessary equations to calculate the transmission coefficients.

We do not examine multiply connected structures and thus do not enforce any global phase relationships.

6.2.1 Lead Eigenfunctions

In the present application, the leads have a Cartesian symmetry and we use the notation described in the section (3.16). In the absence of a magnetic field, the lead eigenfunctions have a full symmetry in the transverse direction and take the form of the sine functions with a wave vector equals $(2E - \frac{n_p^2\pi^2}{w_p^2})^{1/2}$ where E is the total energy, n_p is the quantum number and w_p is the width of the pth lead. However, the applied magnetic field breaks the reflection symmetry and the eigenfunctions are no longer sine functions. Although the lead eigenfunctions are still analytic for a non zero magnetic field [36] these forms involve special functions that complicates the

calculation. Therefore we seek a numeric solution for them. We exactly follow the theory presented by Tamura and Ando [36]. We repeat the procedure here for the completeness.

Recall that the lead coordinate system is (x_p, y_p) where x_p is the longitudinal and y_p is the transverse coordinate, we seek for a solution of the form,

$$\zeta^p_{n_p}(x_p, y_p) = e^{ik_{p,n_p}x_p} f_{p,n_p}(y_p), \tag{6.9}$$

where p denotes the lead index and k_{p,n_p} is the wave number of the electron in the longitudinal direction when the electron is in the subband n_p. In order to have this form for the lead eigenfunctions, we choose the asymmetric gauge for the vector potential $A = (-\mathcal{B}y, 0, 0)$. We substitute the form of the wave function (eq.6.9) in the equation (6.8) and get,

$$\left[-\frac{1}{2}\frac{\partial^2}{\partial y_p^2} + \frac{1}{2}(k_{p,n_p} + y_p\mathcal{B})^2\right] f_{p,n_p}(y_p) = \epsilon f_{p,n_p}(y_p). \tag{6.10}$$

In the infinite plane the solutions to this equation are shifted simple harmonic wave functions in which the eigenspectrum is given by discrete Landau levels. We no longer have Landau level discreteness due to the hard wall boundary conditions. Since the lead eigenfunctions should obey the hard wall boundary conditions, those can be expanded in terms of the infinite well wave functions, $\chi_{p,m_p}(y_p)$,

$$f_{p,n_p}(y_p) = \sum_{m_p}^{\infty} c^p_{n_p,m_p}\chi_{p,m_p}(y_p), \tag{6.11}$$

where $\chi_{p,m_p}(y_p) = \sqrt{\frac{2}{w_p}}\sin\frac{m_p\pi}{w_p}y_p$. We look for the expansion coefficients, $c^p_{n_p,m_p}$. In this process, we define another set of vectors, $d^p_{n_p,m_p} = k_{p,n_p}c^p_{n_p,m_p}$. This substitution allows us to turn a quadratic eigenvalue equation into a linear equation. By plugging these forms in the equation (6.10), we get the matrix equation,

$$\begin{pmatrix} 0 & 1 \\ \alpha & \beta \end{pmatrix} = k \begin{pmatrix} c \\ d \end{pmatrix}, \tag{6.12}$$

which is evidently an eigenvalue equation for the wave vector k. We have omitted all the superscripts and subscripts for simplicity. In this equation,

$$\alpha_{m,m_p} = \left(2\epsilon - \frac{m^2\pi^2}{w_p^2}\right)\delta_{m,m_p} - \mathcal{B}^2 \left\langle y^2 \right\rangle_{m,m_p}, \tag{6.13}$$

and,

$$\beta_{m,m_p} = -2\mathcal{B} \left\langle y \right\rangle_{m,m_p}. \tag{6.14}$$

This is an eigenvalue equation with dimension $2N \times 2N$, which gives $2N$ eigenvalues and $2N$ eigenvectors which represent two sets of solutions for the lead eigenfunctions. Half of these solutions are right going and the other half are left going waves. The wave vector k can be real, imaginary or complex. The real wave vectors are current carrying waves, whereas the imaginary wave vectors are evanescent waves. While only the current carrying waves have a physical meaning, we need to include the evanescent waves for the mathematical completeness. The graph (fig.6.4) shows the real part of the eigenfunctions of the lead when the magnetic field is given by $\mathcal{B} = 15$.

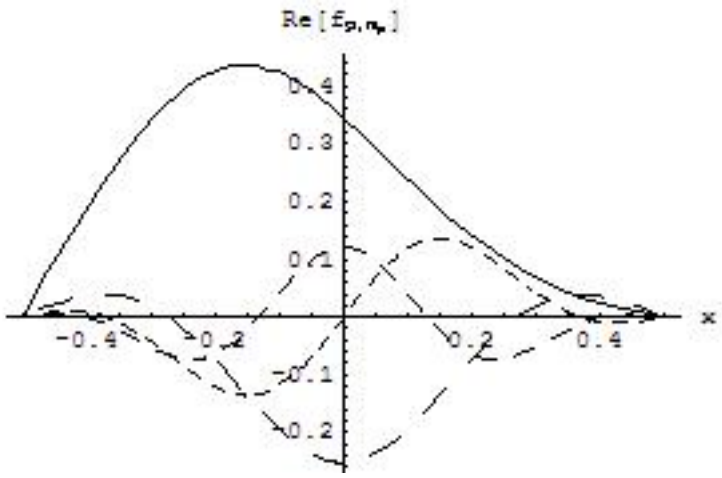

Figure 6.4: The real part of the transverse eigenfunction in a lead in the presence of a perpendicular magnetic field $\mathcal{B} = 15$. The width of the lead $w_p = 1$.

It is important to note that these lead eigenfunctions are not orthogonal to each other. However they do make a complete set so that we can use them to expand the

scattering wave function in the pth lead as,

$$\Psi^{p,p_0}_{E,n_{p_0}}(x_p, y_p) = \sum_{n_p}^{N} \tau^{p,p_0}_{n_p,n_{p_0}} e^{ik_{p,n_p}x_p} f_{p,n_p}(y_p). \tag{6.15}$$

The expansion coefficients $\tau^{p,p_0}_{n_p,n_{p_0}}$ are the interested scattering amplitudes which are used to calculate the transmission coefficients as we describe follows.

The flux in each outgoing lead can be calculated as [35],

$$J_p \sim \int dy_p \left[\Psi^*_{E,n_{p_0}}(x_p, y_p) \left(-i\frac{d}{dx_p} - A_x \right) \Psi_{E,n_{p_0}}(x_p, y_p) + \right.$$
$$\left. \Psi_{E,n_{p_0}}(x_p, y_p) \left(i\frac{d}{dx_p} - A_x \right) \Psi^*_{E,n_{p_0}}(x_p, y_p) \right]. \tag{6.16}$$

Since we have not normalized our eigenfunctions to unit flux, the flux in the pth lead is not given by $\sum_{n_p} \left| \tau^{p,p_0}_{n_p,n_{p_0}} \right|^2$. Once we solve for $\tau^{p,p_0}_{n_p,n_{p_0}}$'s using the RMT which we will describe later in this chapter, we can calculate the current going through each lead in the device according to the equation (6.16). Even though we use N number of subbands in the expansion of eq.(6.15) not all of them are current carrying. The evanescent waves do not contribute to the flux in the leads as they do not contribute to the asymptotic solution. One determines the value of N such that the calculation gives the desired precision as we described in the chapter (3). It was found that this number is always larger than the number of open channels at that energy. In the zero field case we calculated the number of open channels according to the equation, (3.9). This equation no longer holds in the presence of the magnetic field and we calculate the number of open channels by looking at the value of the wave vector, k_{p,n_p}. If the imaginary part of the wave vector equals to zero, it is a current carrying wave. Also note that in the magnetic field problem, the wave vector can also be complex and one should not conclude the nature of the wave by just looking at the real part of the wave vector. Now we use only the open channels to calculate the flux going through the lead according to the equation (6.16). Then the transmission coefficient from lead q to lead p equals to J_p/J_q.

In order to calculate the flux, J_p, we substitute the equation (6.15) in the equation

(6.16). One might conclude that, due to the non-orthogonality of the lead eigenfunctions, the cross terms will not cancel out and we will end up having a position dependent flux which would be puzzling. This problem does not arise however, since two lead eigenfunctions of the same energy would satisfy [35],

$$\int_{-\frac{w_p}{2}}^{\frac{w_p}{2}} dy_p f_{k_{p,\nu_p}}(y_p) f_{k_{p,\beta_p}}(y_p) \left(k_{p,\nu_p} + k_{p,\beta_p} + 2y_p\mathcal{B}\right) = 0, \tag{6.17}$$

even though the lead eigenfunctions do not obey the standard orthogonality relation. This relation (eq.6.17) will cancel out the cross terms in the flux calculation.

Now we need to develop a procedure for calculating the transmission amplitudes, $\tau^{p,p_0}_{n_p,n_{p_0}}$ where we combine the lead solutions and the interior region solutions. In the following section we discuss the interior region problem.

6.2.2 Interior Region Solution

Similar to the zero field problem, we need to expand the scattering wave function in terms of some basis functions relevant for the interior region. In the earlier zero field RMT, we started with the interior region Hamiltonian. There we found that the Hamiltonian is not Hermitian in the finite interior region and its eigenfunctions do not make a complete set. We defined the Bloch Hamiltonian of the system which is Hermitian in the finite interior region. We expanded the scattering wave function in the interior region in terms of the Bloch eigenfunctions. It turns out that the Bloch Hamiltonian term, $\mathcal{L}$ is the term which relates the flux through the soft boundaries. We follow the similar path for the magnetic field problem.

First we find the Bloch Hamiltonian corresponding to the magnetic-Hamiltonian (eq.6.3). According to the equations (6.7) and (6.8), the form of the Hamiltonian depends on the gauge, so the Bloch term also will be gauge dependent. We will first discuss the problem for an arbitrary gauge and then give the form of the Bloch operator for the symmetric and asymmetric gauges. In the presence of a magnetic

field, the Bloch operator takes the form,

$$\hat{\mathcal{H}}_B = \hat{\mathcal{H}} + \mathcal{L}_1 + \mathcal{L}_2, \tag{6.18}$$

where $\mathcal{L}_1$ is the magnetic field independent part and $\mathcal{L}_2$ is the magnetic field dependent part of the Bloch operator. Recall that the operator $\mathcal{L}_1$ takes the form,

$$\mathcal{L}_1 = \frac{1}{2}\sum_{s_p} \delta(x - s_p)\hat{\nabla} \cdot \hat{n}. \tag{6.19}$$

The operator $\mathcal{L}_2$ is the term that makes the magnetic field dependent Hamiltonian to be Hermitian. We will first consider the additional terms that come into the Hamiltonian due to the magnetic field,

$$\mathcal{H}_{\text{mag}} = i\mathcal{B}\mathcal{A}_x\frac{\partial}{\partial x} + i\mathcal{B}\mathcal{A}_y\frac{\partial}{\partial y} + \frac{\mathcal{B}^2}{2}\left(\mathcal{A}_x^2 + \mathcal{A}_y^2\right), \tag{6.20}$$

where we define the reduced vector potential $\mathcal{A}$ as $\mathcal{A} = (-y/2, x/2, 0)$ for the symmetric gauge and $\mathcal{A} = (-y, 0, 0)$ for the asymmetric gauge. The third term in the equation (6.20) is just a multiplicative term that is Hermitian independent of the gauge. We have to consider the Hermiticity of the first two terms. We will consider the first term,

$$\hat{h} = i\mathcal{B}\mathcal{A}_x\frac{\partial}{\partial x}. \tag{6.21}$$

We add a term $\mathcal{L}_2^x$ to $\hat{h}$ such that the operator $\hat{h} + \mathcal{L}_2^x$ is Hermitian. In order to have the Hermiticity, two eigenfunctions of the operator $\hat{h} + \mathcal{L}_2^x$ should satisfy,

$$\left(f, (\hat{h} + \mathcal{L}_2^x)g\right) = \left((\hat{h} + \mathcal{L}_2^x)f, g\right). \tag{6.22}$$

We are looking for the form of the operator $\mathcal{L}_2^x$. We will follow several mathematical steps as follows.

The Hermiticity of $\hat{h} + \mathcal{L}_2^x$ requires,

$$\left(f, \hat{h}g\right) + (f, \mathcal{L}_2^x g) = \left(\hat{h}f, g\right) + (\mathcal{L}_2^x f, g). \tag{6.23}$$

The first term in the left hand side of the equation (6.23) becomes,

$$\text{LHS}_1 = i\int dx\ \ dy\ f i\mathcal{B}\mathcal{A}_x\frac{\partial g}{\partial x}. \tag{6.24}$$

By doing integration by parts,

$$\begin{aligned} \text{LHS}_1 &= i\mathcal{B}\mathcal{A}_x fg\ |_{\text{boundaries}} - i\mathcal{B}\int dx\ dy\ g\mathcal{A}_x \frac{\partial f}{\partial x}, && (6.25)\\ &= i\mathcal{B}\mathcal{A}_x fg|_{\text{boundaries}} + \left(\hat{h}f, g\right). && (6.26) \end{aligned}$$

So the equation (6.22) becomes,

$$\begin{aligned} i\mathcal{B}\mathcal{A}_x fg|_{\text{boundaries}} + \left(\hat{h}f, g\right) + (f, \mathcal{L}_2^x g) &= \left(\hat{h}f, g\right) + (\mathcal{L}_2^x f, g) && (6.27)\\ i\mathcal{B}\mathcal{A}_x fg|_{\text{boundaries}} + (f, \mathcal{L}_2^x g) &= (\mathcal{L}_2^x f, g) && (6.28) \end{aligned}$$

From this we can get the condition that $\mathcal{L}_2^x$ should satisfy as,

$$\mathcal{L}_2^x - (\mathcal{L}_2^x)^+ = -\sum_{s_p} i\epsilon\mathcal{B}\delta(x - s_p)\mathcal{A}_x, \tag{6.29}$$

where ϵ is + for the upper integration boundaries and negative for the lower integration boundaries. This gives the magnetic-field Bloch operator term $\mathcal{L}_2^x$ as,

$$\mathcal{L}_2^x = -\sum_{s_p} \frac{i\epsilon\mathcal{B}}{2}\delta(x - s_p)\mathcal{A}_x. \tag{6.30}$$

Note that the Bloch operator has a different form when compared to the zero field Bloch term. In the zero field term the Bloch term equals to the boundary term, where as in the magnetic field problem, the Bloch operator term is the half of the boundary term.

Following the similar way, we can make the y dependent part of the Hermitian and we get the total magnetic Bloch term as,

$$\mathcal{L}_2 = -\sum_{s_p^x} \frac{i\epsilon\mathcal{B}}{2}\delta(x - s_p^x)\mathcal{A}_x - \sum_{s_p^y} \frac{i\epsilon\mathcal{B}}{2}\delta(y - s_p^y)\mathcal{A}_y, \tag{6.31}$$

where the first term runs over all the x boundaries and the second term runs over all the y boundaries. When solving for the interior region eigenfunctions, we use the symmetric gauge that $\mathcal{A} = (-y/2, x/2, 0)$. Then the magnetic Bloch term takes the form,

$$\mathcal{L}_2^{\text{sym}} = \sum_{s_p^x} \frac{i\epsilon\mathcal{B}}{4}\delta(x - s_p^x)y - \sum_{s_p^y} \frac{i\epsilon\mathcal{B}}{4}\delta(y - s_p^y)x. \tag{6.32}$$

When solving for the lead eigenfunctions, we use the asymmetric gauge that $\mathcal{A} = (-y, 0, 0)$. Then the magnetic Bloch term takes the form,

$$\mathcal{L}_2^{\text{asym}} = \sum_{s_p^x} \frac{i\epsilon\mathcal{B}}{2}\delta(x - s_p^x)y. \tag{6.33}$$

The two Bloch terms, $\mathcal{L}_1 + \mathcal{L}_2$ makes $\mathcal{H}_B$ (equations 6.7 and 6.8) Hermitian and we use its eigenfunctions ϕ_j to expand the scattering wave functions in the interior region as,

$$|\Psi_E\rangle = \sum_j C_j |\phi_j\rangle . \tag{6.34}$$

In the following section we explain how to relate the interior region solution (eq.6.34) and the lead solution (eq.6.15) to solve for the transmission coefficients, $\tau_{n_p,n_{p_0}}^{p,p_0}$.

6.2.3 R-Matrix Formulation

Knowing the lead eigenfunctions and the interior region Bloch eigenfunctions, we can formulate the R-matrix equation to solve for the unknown scattering amplitudes given in eq.(6.15). The scattering wave function is a solution to the equation,

$$\mathcal{H} \left|\Psi_{E,n_{p_0}}\right\rangle = E \left|\Psi_{E,n_{p_0}}\right\rangle , \tag{6.35}$$

where E is the energy of the incoming electron and the electron is injected from $n_{p_0}^{th}$ subband of the p_0^{th} lead.

In the previous chapter (eq.3.16), we have formulated an equation to write the scattering wave function of the qth lead as,

$$\left|\Psi_{E,n_{p_0}}^{q,p_0}(x_q, y_q)\right\rangle = \sum_j \frac{|\phi_j(x_q, y_q)\rangle \langle\phi_j(x_p, y_p)|}{E_j - E} \mathcal{L} \left|\Psi_{E,n_{p_0}}^{p,p_0}(x_p, y_p)\right\rangle , \tag{6.36}$$

where $\mathcal{L}$ is the Bloch operator. In the presence of a magnetic field the Bloch operator has two terms that $\mathcal{L} = \mathcal{L}_1 + \mathcal{L}_2$. This equation (6.36) is true only inside the interior region and we use that to write the scattering wave function on the soft boundaries where the scattering wave function can also be expanded in terms of the lead eigenfunctions. The notation and the procedure remains the same as in the zero-field

RMT, however extra care has to be taken since the transverse lead eigenfunctions, $f_{p,n_p}(y_p)$ are not orthogonal.

One more important thing to notice in equation (6.36) is that the Bloch eigenfunctions ϕ_j are the solutions to the Bloch Hamiltonian with the symmetric gauge (since we have chosen the symmetric gauge for the interior region). However the Bloch operator appear in the right hand side of the equation (6.36) is $\mathcal{L} = \mathcal{L}_1 + \mathcal{L}_2^{\text{asym}}$ as we have chosen the asymmetric gauge for each lead.

Now the scattering wave function in the interior region relates to the R-matrix as,

$$\left|\Psi^{q,p_0}_{E,n_{p_0}}(x_q, y_q)\right\rangle = \sum_p \mathcal{M}_E(q, n_q; p, n_p) \left|\chi_{q,n_q}(y_q)\right\rangle \left\langle\chi_{p,n_p}(y_p)\right| (\nabla + i\mathcal{B}y_p) \left|\Psi^{p,p_0}_{E,n_{p_0}}(x_p, y_p)\right\rangle, \tag{6.37}$$

where the $\mathcal{M}$ matrix is defined in the eq.(3.30). Now we consider this equation on the soft boundaries ($x_q = 0$) and project this equation on to the transverse state vector $\left|\chi_{q,n_q}\right\rangle$ as,

$$\left\langle\chi_{q,n_q}\right| \left|\Psi^{q,p_0}_{E,n_{p_0}}(x_q = 0, y_q)\right\rangle = \sum_p \mathcal{M}_E(q, n_q; p, n_p) \left\langle\chi_{p,n_p}(y_p)\right| (\nabla + i\mathcal{B}y_p) \left|\Psi^{p,p_0}_{E,n_{p_0}}(x_p, y_p)\right\rangle. \tag{6.38}$$

The matrix $\mathcal{M}$ is defined using the interior region eigenfunctions. We need to use equation (6.38) to relate the R-matrix (or $\mathcal{M}$ matrix) to the transmission coefficients which is defined in the leads. We explicitly write the scattering wave function on the boundary s_q using the equation (6.15) as,

$$\left|\Psi^{q,p_0}_{E,n_{p_0}}(x_q = 0, y_q)\right\rangle = \left|f_{q,n_q}(y_q)\right\rangle \delta_{q,p_0}\delta_{n_q,n_{p_0}} + \sum_{n_q=1}^{N_q} \tau^{q,p_0}_{n_q,n_{p_0}} \left|f_{q,n_q}(y_q)\right\rangle. \tag{6.39}$$

At the boundary s_q, the normal derivative of the scattering wave function is,

$$\nabla \left|\Psi^{q,p_0}_{E,n_{p_0}}(x_q = 0, y_q)\right\rangle = -ik_{p_0,n_{p_0}} \left|f_{q,n_q}(y_q)\right\rangle \delta_{q,p_0}\delta_{n_q,n_{p_0}} + \sum_{n_q=1}^{N_q} ik_{q,n_q}\tau^{q,p_0}_{n_q,n_{p_0}} \left|f_{q,n_q}(y_q)\right\rangle. \tag{6.40}$$

We would like to project all the wave functions on to the transverse state vector $\left|\chi_{q,n_q}(y_q)\right\rangle$. So we write the above two equations (6.39 and 6.40) in terms of $\left|\chi_{q,n_q}(y_q)\right\rangle$

as,

$$\left|\Psi^{q,p_0}_{E,n_{p_0}}(x_q=0,y_q)\right\rangle = \sum_{m_q=1}^{M_q} c^q_{n_q,m_q}\left|\chi_{q,m_q}(y_q)\right\rangle \delta_{q,p_0}\delta_{n_q,n_{p_0}} + \sum_{n_q=1}^{N_q}\sum_{m_q=1}^{M_q} c^q_{n_q,m_q}\left|\chi_{q,m_q}(y_q)\right\rangle \tau^{q,p_0}_{n_q,n_{p_0}} \tag{6.41}$$

and,

$$\nabla\left|\Psi^{q,p_0}_{E,n_{p_0}}(x_q=0,y_q)\right\rangle = -ik_{p_0,n_{p_0}}\sum_{m_q=1}^{M_q} c^q_{n_q,m_q}\left|\chi_{q,m_q}(y_q)\right\rangle \delta_{q,p_0}\delta_{n_q,n_{p_0}} + \sum_{n_q=1}^{N_q}\sum_{m_q=1}^{M_q} ik_{q,n_q} c^q_{n_q,m_q}\left|\chi_{q,m_q}(y_q)\right\rangle \tau^{q,p_0}_{n_q,n_{p_0}}. \tag{6.42}$$

The coefficients $c^q_{n_q,m_q}$ are calculated according to the procedure explained in section (6.2.1). The above two equations (6.41 and 6.42) can be projected on to $\left|\chi_{q,n_q}(y_q)\right\rangle$ as,

$$\left\langle\chi_{q,n_q}(y_q)\right|\left|\Psi^{q,p_0}_{E,n_{p_0}}(x_q=0,y_q)\right\rangle = c^q_{n_q,m_q}\delta_{q,p_0}\delta_{n_q,n_{p_0}} + \sum_{n_q=1}^{N_q} c^q_{n_q,m_q}\tau^{q,0}_{n_q,n_{p_0}}, \tag{6.43}$$

and,

$$\left\langle\chi_{q,n_q}(y_q)\right|\nabla\left|\Psi^{q,p_0}_{E,n_{p_0}}(x_q=0,y_q)\right\rangle = -ik_{p_0,n_{p_0}} c^q_{n_q,m_q}\delta_{q,0}\delta_{n_q,n_{p_0}} + \sum_{n_q=1}^{N_q} ik_{q,n_q} c^q_{n_q,m_q}\tau^{q,p_0}_{n_q,n_{p_0}}. \tag{6.44}$$

Now we substitute the equations (6.43 and 6.44) in the equation (6.38) which gives,

$$\begin{aligned} c^q_{n_q,m_q}\delta_{q,p_0}\delta_{n_q,n_{p_0}} \;+\; \sum_{n_q=1}^{N_q} c^q_{n_q,m_q}\tau^{q,p_0}_{n_q n_{p_0}} &= \sum_p\sum_{m_p}\mathcal{M}_E(q,n_q,p,n_p)\,[\\ &-ik_{p_0,n_{p_0}} c^p_{n_p,m_p}\delta_{p,p_0}\delta n_p,n_{p_0} + \sum_{n_p=1}^{N_p} ik_{p,n_p} c^p_{n_p,m_p}\tau^{p,p_0}_{n_p,n_{p_0}} + \\ &i\mathcal{B}(c^p_{n_p,m_p}\delta_{p,p_0}\delta_{n_p,n_{p_0}}\left\langle\chi_{p,m_p}(y_p)\right| y_p\left|\chi_{p,m_p}(y_p)\right\rangle + \\ &\sum_{n_p=1}^{N_p} c^p_{n_p,m_p}\left\langle\chi_{p,m_p}(y_p)\right| y_p\left|\chi_{p,m_p}(y_p)\right\rangle\tau^{p,p_0}_{n_p,n_{p_0}})\,]\,. \end{aligned} \tag{6.45}$$

This equation is comparable to the equation (3.29) in the zero-field RMT. Note the difference between the eq. (3.29) and the eq.(6.45). The extra complexity in the

magnetic-field RMT is due to the non-orthogonality of the lead eigenfunctions and the additional term in the Bloch operator $\mathcal{L}_2$. The equation (eq.6.45) gives a set of linear algebra equations that can be solved for the unknown scattering coefficients, $\tau^{q,p_0}_{n_q n_{p_0}}$. In the equation (6.45) everything is known except the matrix elements of the matrix, $\mathcal{M}$. We will calculate the $\mathcal{M}$ matrix elements using a variational basis set. In order to explain the procedure, we will calculate the scattering coefficients of a 4-terminal square junction.

6.3 Applications: 4-Terminal Square Junction.

6.3.1 Transmission Coefficients

In this section we calculate the transmission coefficients for the electrons injected into the device shown in the figure (6.2). In the bend resistance experiment, a current is injected from lead 4 to lead 1 which means that the electrons are injected from the lead 1. The schematic diagram of the device is the same as the one we discussed in the zero-field RMT (fig.3.6). This device has a symmetric geometry that all the leads are same in width. We define the coordinate system for this device as the same as the one we used for zero-field 4-terminal square junction problem.

In order to calculate the transmission coefficients of the electrons in this system, we need to simultaneously solve the set of equations given by eq.(6.45), which requires the matrix elements of $\mathcal{M}$. We calculate those matrix elements using a set of variational basis functions which is as same as the set of basis functions used in the plus junction with the zero field problem. So the field independent Bloch Hamiltonian is the same as the Hamiltonian we had in the section (3.4). The symmetric gauge is used when solving the interior region problem for which the field dependent Bloch Hamiltonian term takes the form,

$$\mathcal{L}_2 = -\frac{iy\mathcal{B}}{4}\delta(x+\frac{w_1}{2}) + \frac{iy\mathcal{B}}{4}\delta(x-\frac{w_1}{2}) + \frac{ix\mathcal{B}}{4}\delta(y+\frac{w_0}{2}) - \frac{ix\mathcal{B}}{4}\delta(y-\frac{w_0}{2}). \quad (6.46)$$

We solve the generalized eigenvalue problem to calculate the eigenvalues, E_j^B and the corresponding eigenvectors with the expansion coefficients which is defined as,

$$\left|\phi_{n,m}^B(x,y)\right\rangle = \sum_{a,b} d_{n,m,a,b}^B \left|\eta_a(x)\right\rangle \left|\zeta_b(y)\right\rangle . \tag{6.47}$$

We use the superscript to mention that there is an applied perpendicular magnetic field. Now the coefficients needed for the elements of $\mathcal{M}$ can be calculated according to the equation (3.30). We need the γ coefficients for calculating the elements of $\mathcal{M}$ matrix which is obtained according to,

$$\gamma_{n,m,q,n_q} = \sum_{a,b} d_{n,m,a,b}^B \left|\eta_a(x = x_q)\right\rangle \left\langle \chi_{q,n_q}(y_q) \left|\zeta_b(y)\right\rangle . \tag{6.48}$$

The coefficients $d_{n,m,a,b}^B$ are calculated by diagonalizing the magnetic Bloch Hamiltonian. Here x and y are the interior region coordinates and y_q is the lead coordinate. We have to convert the coordinates and do the integration. For instance, when we evaluate the γ values on the 2nd boundary of the plus junction problem, (fig3.6), $x \to w_1/2$ and $y \to y_2$ and then do the integration from $y_2 = -w_2/2$ to $y_0 = w_2/2$. We calculate the $\mathcal{M}$ matrix elements and then solve the linear algebra equations to find the transmission coefficients. In the interior region calculation, we use 10×10 basis functions to diagonalize the Bloch Hamiltonian. We use the same number of basis functions, 10 basis functions to expand the lead eigenfunctions. This makes sure that we have enough basis functions (for instance at energy = 60, we have only three open channels and 7 evanescent waves which is calculated in the appendix B). However we have not optimized the code to use the least required number of evanescent functions.

The graph (fig.6.5) shows the transmission coefficients of the electrons in the 4-terminal square junction device for different values of magnetic fields. The values of the magnetic fields are shown in the inset of each graph. The plotted values are the lead to lead transmission coefficients, $T_{qp_0} = \sum_{n_q,n_{p_0}} \mathcal{T}_{n_q,n_{p_0}}^{q,p_0}$. Here we have considered an electron injected from the lead 1 that $p_0 = 1$. As a check for the method, we make

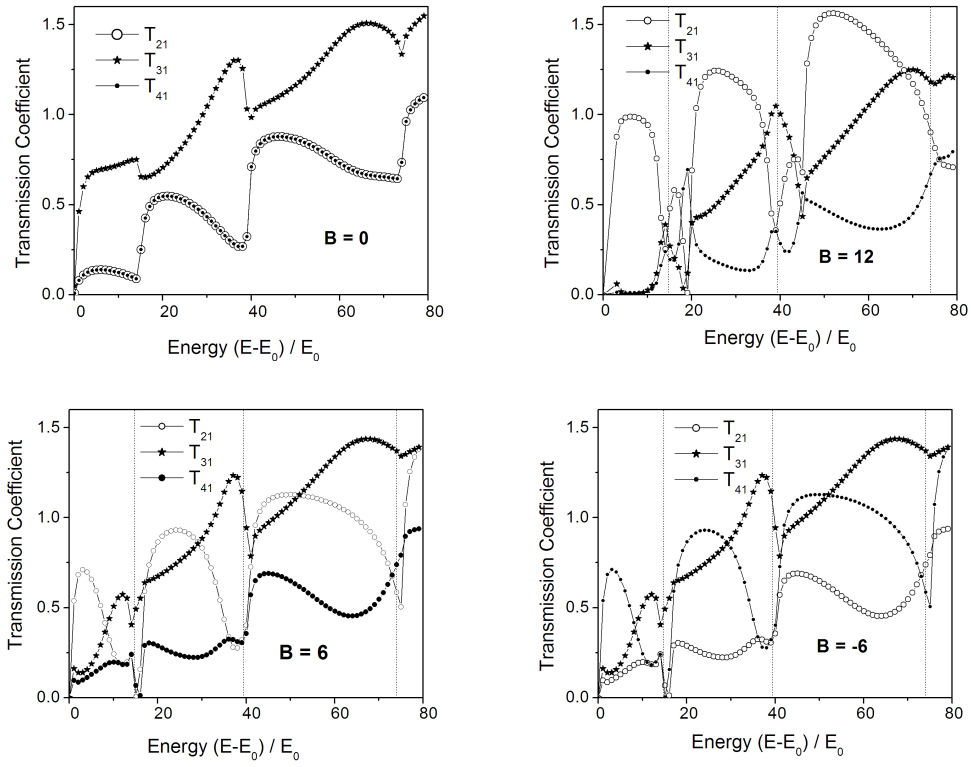

Figure 6.5: Transmission Coefficients for the electron injected to the 4-terminal square junction device shown in the (6.2). Electrons are injected from the lead 1. We have calculated the transmission coefficients for 4 different cases, $\mathcal{B} = 0$, $\mathcal{B} = 6$, $\mathcal{B} = -6$ and $\mathcal{B} = 12$. When there is no magnetic field, since the device is symmetric both T_{21} and T_{41} are equal and T_{31} is always larger than the sidearm transmissions. This zero field result correctly recovers the result we obtained with zero-field RMT. This figure also shows that when you increase the magnetic field, the transmission coefficient to the lead 2 increases and at some energies it is even higher than the forward transmission. Also the two plots relevant to $\mathcal{B} = 6$ and $\mathcal{B} = -6$ show that by changing the direction of the magnetic field, the transmission coefficients to the left and right leads interchange as one would expect.

$\mathcal{B} = 0$ and calculate the transmission coefficients. The transmission coefficients for the left and right directions, T_{14} and T_{21} lie top of each other. That is because of the symmetry when there is no magnetic field. The results show that the magnetic-field RMT correctly recovers the zero-field result. Note that the forward transmission, T_{31}

is always higher than the left and right transmission when there is no magnetic field. That means even though the current source wants the electrons to go from lead 1 to lead 4, electrons more likely go to lead 3 (forward lead). That is because the electrons move ballistically. If electrons were diffusive, electrons equally pile up in the lead 2 and 4. Now since the electrons motion is ballistic, more electrons accumulated in the forward lead, giving a negative voltage V_{23} which result in a negative bend resistance.

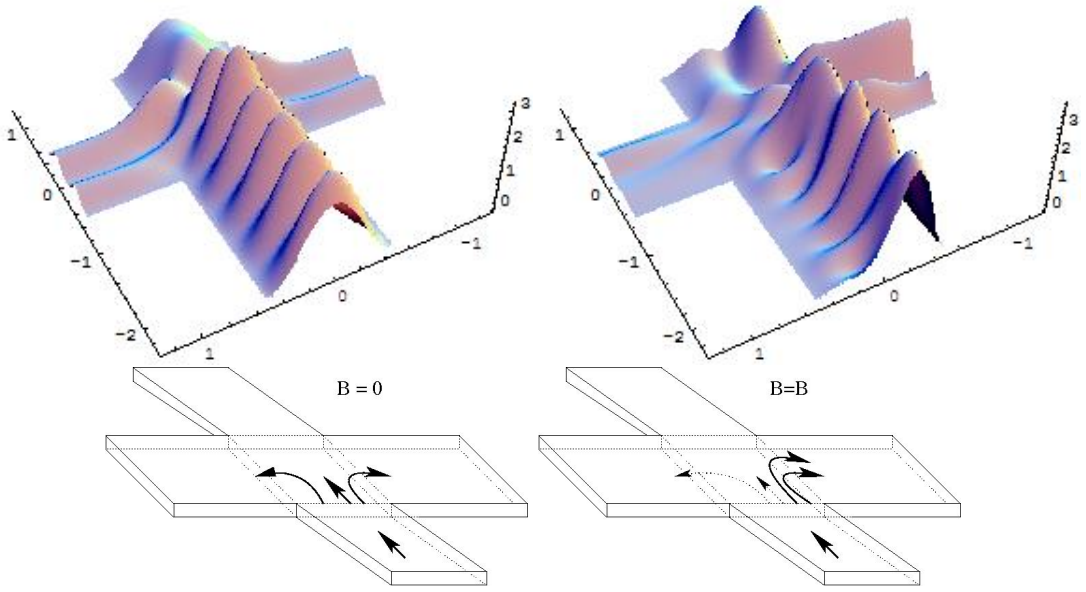

Figure 6.6: The probability density of a positively charged particle injected to the 4-terminal junction. The left figure shows the probability density of the particle when there is no magnetic field and the figure to the right is the probability density when the applied perpendicular magnetic field $\mathcal{B} = w_0^2/l_B^2 = 20$. Both the probabilities are calculated when the scattering energy, $E = 25$ in the dimensionless units as described in the text. Note that the sidearms have similar probabilities for the left figure, but not for the right figure.

As you increase the magnetic field, electrons experience the Lorentz force and tend to deflect to the lead 2. The transmission coefficient, T_{21} is higher than the transmission coefficient, T_{31} as we observe from the transmission coefficients at $\mathcal{B} = 6$

and $\mathcal{B} = 12$. Also the transmission coefficients at $\mathcal{B} = 6$ and $\mathcal{B} = -6$ shows that the direction of the electron path changes as you change the direction of the magnetic field which again proves the accuracy of the calculation.

Knowing the transmission amplitudes, we can calculate scattering wave function. We have plotted the probability density of a positively charged particle traveling in the 4-terminal junction at energy, $E = 25$. We show (fig.6.6) both the zero field scattering wave function and the wave function at $\mathcal{B} = 20$. We can see the symmetry of the scattering wave function when there is no magnetic field and how the electron deflects towards the side arm when there is a magnetic field perpendicular to the system.

6.3.2 Calculating the Magneto-Transport Properties

In the previous section we calculated the transmission coefficients of the 4-terminal device at different energies (fig.6.5). Now we use these transmission coefficients to calculate the transport properties according to the LB theory. The x axis of these graphs (fig.6.5) are the energy of the incoming electron. At zero temperature, as we have discussed in the chapter (1), only the transmission coefficient at the Fermi energy contributes to the transport properties. This will be different when we consider finite temperatures.

At zero temperature, we consider the transmission coefficients at the Fermi energy which is a point on the x-axis. That is, as the Fermi energy changes, the point we have to look at in the transmission coefficient graph will be different. An important question is what decides this point. Most of the parameters of the system depend on the Fermi energy, which is set by the concentration of electrons in the system. However the x-axis of this graph is a dimensionless quantity. In particular the energy is scaled by $E_0 = \hbar^2/m^* w_{p_0}^2$, where we have chosen w_{p_0} as the width of the input lead. So once we have a particular density of states, depending on the width of the input lead, the point we have to consider in the x axis of the above graphs will be different.

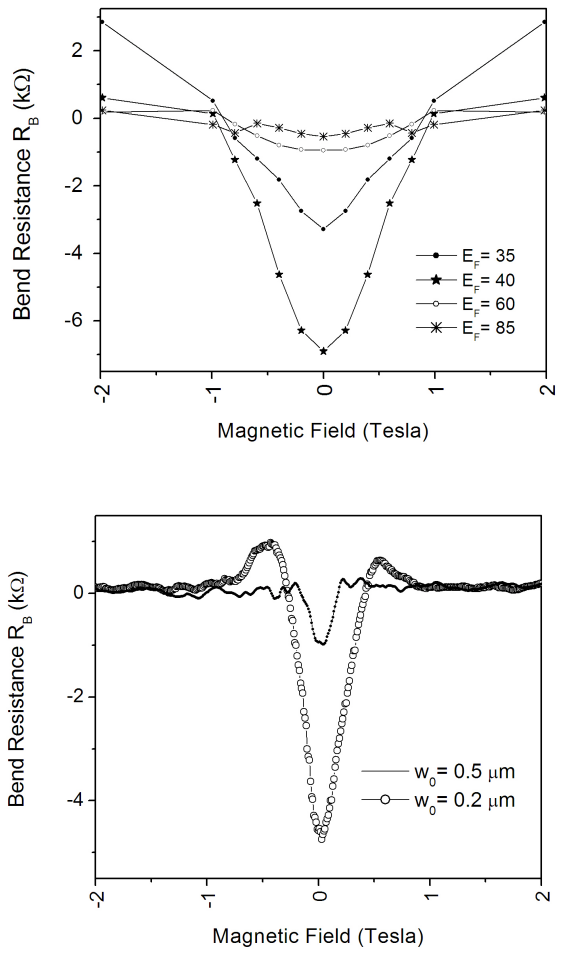

Figure 6.7: The upper plot is the bend resistance, R_B of a 4-terminal square junction device as calculated using the magnetic-field RMT and the LB formula. The lower plot is the experimental observation for R_B as a function of the magnetic field for a device with a geometry shown in the figure (6.3). Note that two geometries are different. In the theory, we have calculated R_B at different Fermi energies, which means that we have calculated the R_B at different sizes of the devices (see appendix B). The results have a qualitative agreement to conclude that the InSb device has a coherent electron behavior.

We have shown how to calculate this value in the appendix (B).

We first consider a device in which the width of the incoming lead equals to 0.1μm and the two-dimensional density of the sample equals $1.90\times10^{11}\text{cm}^{-2}$. For that device

the Fermi Energy, $E_F = 58.7$ in the dimensionless units (see appendix B). At this energy there are 3 open subbands. We calculate the R_B using the equation (1.34). For a comparison we calculate the R_B at different values of Fermi energies and the result is shown in figure (6.7). The lower plot is the experimental observation for R_B as a function of the magnetic field for a device with a geometry shown in the figure (6.3) [10]. The theoretical result qualitatively agrees with the experimental result. Note that two geometries are different. In the theory result, we have calculated R_B at different Fermi energies, which means that we have calculated R_B at different widths of the device. The Fermi energy decreases means the width decreases according to our units. In the appendix (B.1), we have tabulated the dimensionless Fermi energies for different widths of the sample with a carrier concentration, $1.90 \times 10^{11}\text{cm}^{-2}$. We discuss more about the result in the conclusion (6.6). In the next section we show how to calculate the bend resistance of a 4-terminal wedge junction device (fig.6.3).

6.4 Applications: 4-Terminal Wedge Junction Device

In the previous section, we calculated the transmission coefficients of electrons in a 4-terminal square junction device using the magnetic-field RMT. In this section we calculate the transmission coefficients of electrons in a 4-terminal wedge junction device (fig.6.3) which is more relevant to the experimental observation we compare our results with.

A schematic diagram of our four-terminal wedge-junction devices is shown in the figure (4.5). In the chapter (4), we calculated the transmission coefficients of electrons in such a device with no magnetic field (fig. 4.7). We kept the opening angle $2\theta = 43^0$ (which equals to the opening angle of the experimental device [10]), and studied the transmission coefficients for different values of w_D. According to this result, the transmission coefficients do not have much effect when we increase the width w_D

(fig.4.7). What happens there is when we increase the width of the lead, it injects electrons in number of open channels. However, those channels which are higher in subband index and lower in kinetic energy in the longitudinal direction tends to reflect back those higher subbands will not effect the transport. So we do not need to include the higher subband electrons in the calculation. The experimental device has a opening width $w_D = 4.0$, however we simulate the device with $w_D = 1.5$ since we need to include more channels for the convergence when the width of the leads are larger. Since the interior region of this device is quite complicated, we need to use the R-matrix connection formula to solve for the transmission coefficients of electrons in this device.

In the chapter (4) we discussed the R-matrix connection formula and applied it to calculate the transmission coefficients of electrons in a 4-terminal wedge junction device. Here we discuss the basic concepts of the R-matrix connection formula in the presence of a magnetic field. However, we do not develop the equations as we did in the zero field case.

In the zero-field R-matrix connection formula, we calculated the R-matrix elements (or $\mathcal{M}$ matrix elements) corresponding to each soft boundaries using each relevant interior regions. Then we applied the R-matrix equations (all possible combinations) to write the scattering wave function on each soft boundary. Then we applied the continuity of the scattering wave function and the derivative of the wave function.

The same procedure is applied for the magnetic field R-matrix connection formula, however the first derivative of the wave function is not continuous at the boundary. The physical condition is that the flux is continuous across the boundary. Since the Bloch operator is the flux operator through the surface, all the boundary conditions stay the same.

We do not present the calculation here since it follows the same procedure as the zero-field case. However, the set of equations is not the same since the R-matrix

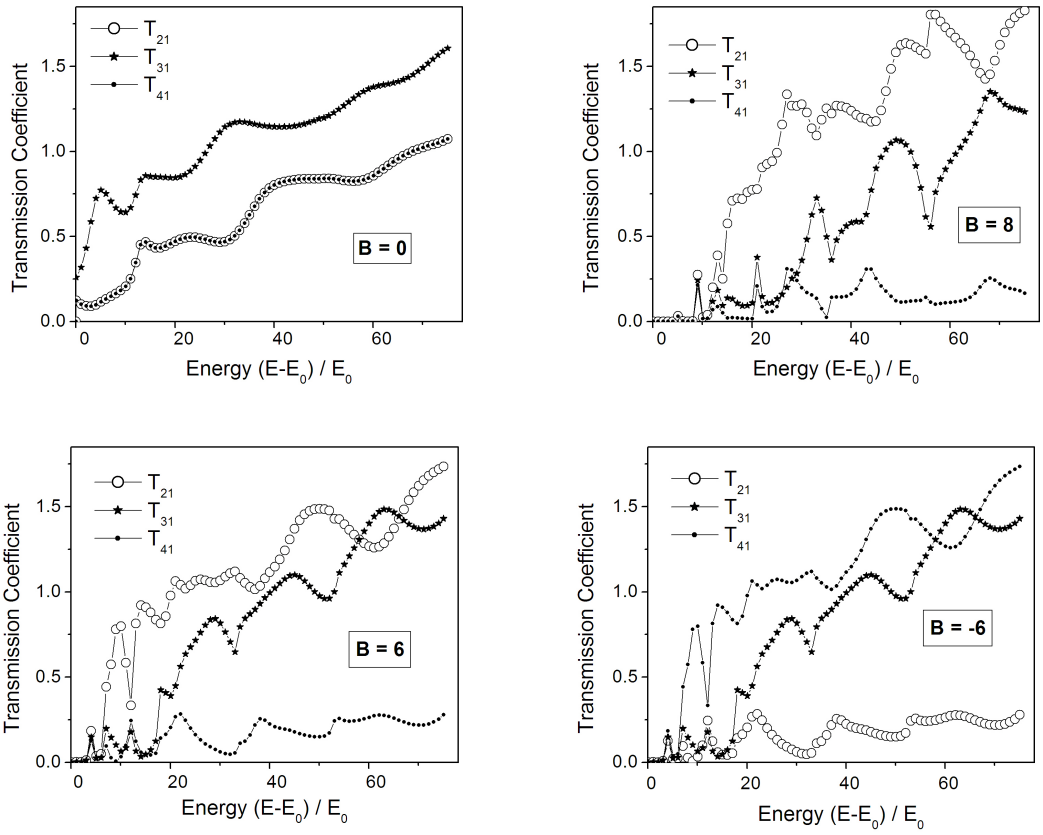

Figure 6.8: Transmission Coefficients for the electrons injected to the 4-terminal wedge junction device shown in the figure (6.3). The device is specified by $w_A = 1.0$, $w_D = 1.5$, and $2\theta_0 = 43^0$ according to the figure (4.5). Electrons are injected from the lead 1. We have calculated the transmission coefficients for 4 different cases, $\mathcal{B} = 0$, $\mathcal{B} = 6$, $\mathcal{B} = -6$ and $\mathcal{B} = 8$. Since the device is symmetric both T_{21} and T_{41} are equal and T_{31} is always larger than the sidearm transmissions when there is no magnetic field. This zero field result correctly recovers the result we obtained with zero-field RMT. This figure also shows that when you increase the magnetic field, the transmission coefficient to the right lead increases and at some energies it is even higher that the forward transmission. Also the two plots relevant to $\mathcal{B} = 6$ and $\mathcal{B} = -6$ show that by changing the direction of the magnetic field, the transmission coefficients to the left and right leads interchange as one would expect.

equation has additional parts. We show the resultant transmission coefficients in the figure (6.8). Using those transmission coefficients, we calculate the bend resistance

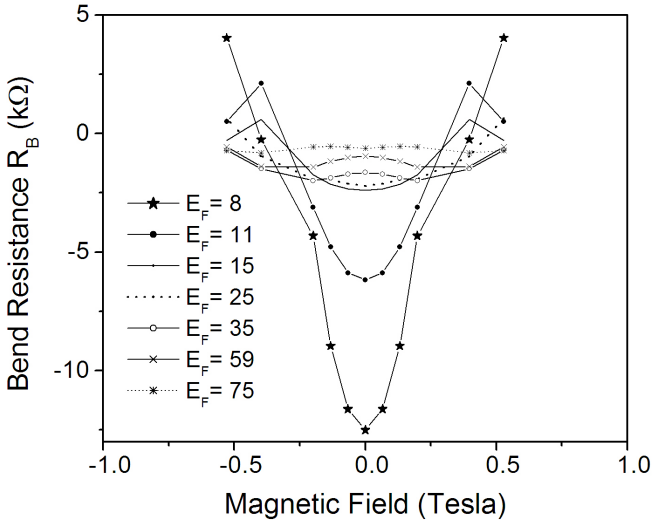

Figure 6.9: Bend resistance of a four-terminal wedge junction device (fig.4.5) as a function of the magnetic field, B. We have calculated the bend resistance at different values of Fermi energies which is for different values of device sizes (w_A). For a conversion of the Fermi energies to the device sizes at a given carrier concentration, see appendix (B).

of the system at zero temperature at different Fermi energies (fig.6.9). The appendix (B) shows the widths of the device corresponding to the Fermi energies considered in the bend resistance calculation (inset of the figure 6.9). We will discuss more about this result in the section (6.6).

6.5 Temperature Dependence of the Bend Resistance

As explained in the section (1.1.1), in order to calculate the finite temperature transport properties according to the LB formula, we need to consider the transmission coefficients of electrons which has energy close to the Fermi energy, according to the equation (1.13). We calculate the finite temperature bend resistance for the four-

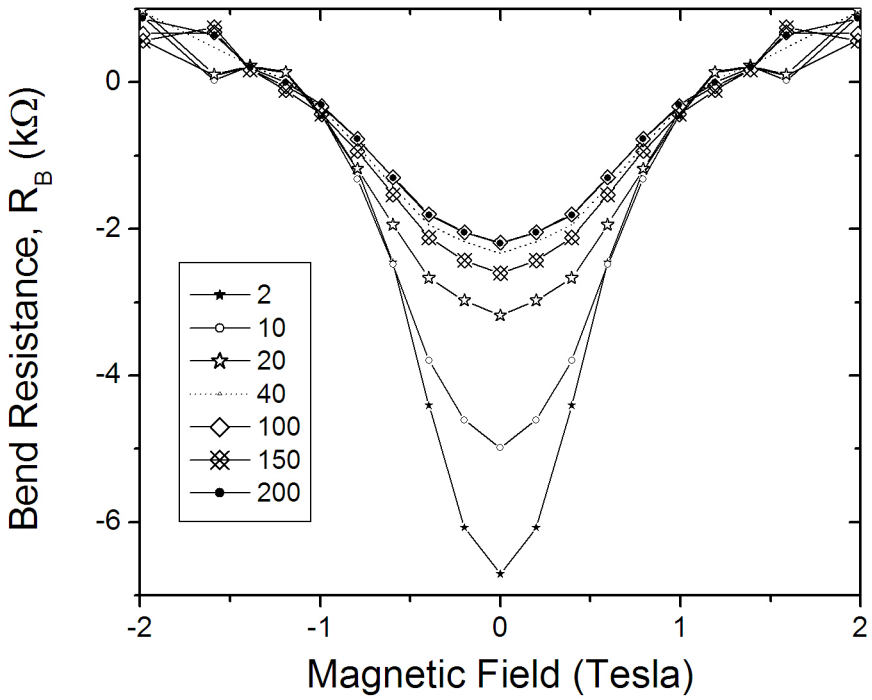

Figure 6.10: Bend resistance, R_B as a function of the magnetic field for the four terminal square junction device when the dimensionless Fermi energy equlas to 40. The different curves are for different temperature as shown in the inset. This graph shows that the bend resistance decreases as you decrease the temperature. However, that behavior breaks down after $T = 100K$. We discuss this in the text (see section 6.6).

terminal square junction device at the Fermi energy, $E_F = 40$ in dimensionless units. And the result is plotted in the figure (6.10).

6.6 Conclusion

In conclusion, we have calculated the bend resistance of a 4-terminal square junction devices and a 4-terminal wedge-junction device in a full quantum mechanical fashion. The results quantitatively agree with the experimental observation.

We particularly look at two experimental observations of the bend resistance, the dependence of the R_B, on the width of the device and on the temperature. According to this result, the variation of the bend resistance as a function of the magnetic field is not monotonic with the width of the sample. This is clear when we look at the transmission coefficients graphs (fig.6.7). The transmission coefficients have a considerable effect on the threshold energies. It is not just the width of the sample matters for the result, but the position of the Fermi energy with respect to the threshold energies. If the width of the sample is such that the Fermi energy lies close to a threshold energy, then the difference between T_{31} and T_{21} is large and we will get a large negative bend resistance. There are not enough experimental results to prove this hypothesis. Also the experiments [10] reported $R_B \sim 4k\Omega$ when the width of the sample equals to $0.2\mu m$. According to our results this high bend resistance can be seen for a narrower device. We could believe that the lithographic width is not the actual width of the device.

The graph (6.10) shows that as you increase the temperature, the bend resistance decreases. However when $T > 100K$ this behavior breaks down and the bend resistance start to increase. We believe that this breakdown is not real. At such a high temperature, our simple model cannot explain the system. We need to include the effects such as the lattice vibrations (phonons) in the model. The breakdown at higher temperature is not surprising since we have neglected all dephasing effects.

Chapter 7

Conclusion

We have developed a theoretical tool, R-matrix theory, which has also been used in atomic and molecular physics, and applied it to calculate the transmission coefficients in two-dimensional solid-state devices. Our approach is different from other R-matrix theories for devices in that we use variational basis functions [58] in the calculation. We have demonstrated that the variational R-matrix theory in device physics converges faster than the conventional R-matrix approach.

Our second major result is the development of the R-matrix connection formula. The R-matrix connection formula uses variational R-matrix theory to calculate the transmission coefficients of electrons in a device with a complicated geometry. Although we have developed the technique, our formula is not generic. However, it can be improved to obtain a generic formula which could be used for a device with an arbitrary geometry.

The variational R-matrix approach has several advantages comparing to other techniques for calculating the transmission coefficients of electrons in a two-dimensional device. As explained in chapter (2), the R-matrix theory separates the energy-dependent calculation from the energy-independent calculations so that the most time-consuming calculations must be done only once, even if we have to get results for a number of energies. Since the variational approach achieves faster convergence, we can get very accurate results using R-matrix theory. As we found in chapter (4),

R-matrix theory is flexible enough to adapt to devices with complicated geometries.

The transmission coefficients lead to transport properties according to Landauer theory (ch.1). We used the calculated transmission coefficients to design new devices and model existing experimental observations. Our major accomplishment was using RMT to design a device to obtain the cooling by deflecting the thermally excited electrons. Our calculation was not optimized, but rather was a proof of the principle that one can improve the cooling effect by different geometries.

Our fourth result was the extension of R-matrix theory to calculate transmission coefficients of electrons in the presence of a magnetic field. Using the transmission coefficients, we calculated the bend resistance of a 4-terminal square-junction device. With the R-matrix connection formula, we were able to calculate the bend resistance of a 4-terminal device with a more complicated geometry. Our results qualitatively agree with experimental observations but differ in detail. However, important experimental details such as the exact gate width (including depletion) and the exact carrier concentration are not precisely known. Given the relatively good agreement, we feel that we have evidence that the device is phase coherent. Future experimental data such as a quantum-Hall measurements of the device will help to count the number of subbands in the leads of the device. We can then deduce the exact effective width of the leads. We also have found that the bend resistance does not change monotonically with the width of the device. More experimental data is required to confirm this finding. Also we note that being able to develop R-matrix theory in the presence of a magnetic field shows that R-matrix theory can be adopted to any sort of potentials. The key issue is to find the relevant Bloch operator term.

Our work is based on the single-particle approximation. We can further develop the technique to calculate the transmission coefficients of electrons in a many-electron system. In fact, extension to the many electron systems is one of the greatest advantages of RMT in atomic physics. Such a many-electron theory will require not only a reformulation of some of the work in this thesis, but also of Landauer-Bütikker

theory. Landauer-Bütikker theory assumes that the scattering device is unchanged due to the electron transport, but in a many electron system, injecting electrons can excite the molecules in the scattering region or the electrons may be captured in the scattering region. This extension will be necessary to describe molecular devices.

Appendix A

Background of R-Matrix Theory

In this appendix we present the background of R-matrix theory in nuclear physics, atomic and molecular physics and the device physics. Please note that this appendix was obtained from the forthcoming paper on variational device R-matrix theory by Jayasekera, Morrison and Mullen [9].

A.1 R-Matrix Theory in Device Physics

In 1947, Wigner and Eisenbud introduced R-matrix theory as a rigorous way of calculating and thinking about nuclear reactions in general and the role of resonances (the compound-nucleus model) in particular. An excellent early account of the formulation of Wigner and Eisenbud [5], which we shall call **conventional R-matrix theory** (as distinct from the variational R-matrix theory we use), appears in the review by Lane and Thomas [42]. Bloch [**?**] made a major contribution to the implementation of R-matrix theory by introducing the "boundary condition operator" $\mathcal{L}_B$, which we shall call the **Bloch operator**. This operator, which is defined on the internal region A of position space, incorporates Neumann boundary conditions that, in conventional R-matrix theory, are imposed on the R-matrix surface $\mathcal{S}_o$ in order to discretize the spectrum in A. Unlike the system Hamiltonian $\mathcal{H}$, the operator $\mathcal{H}_B = \mathcal{H} + \mathcal{L}_B$, which we shall call the **Bloch Hamiltonian**, is Hermitian in A. Its eigenfunctions therefore

constitute a complete set which, in conventional R-matrix theory, constitutes a basis for expanding the system state vector Ψ_E in A. The (discrete) eigenvalues of $\mathcal{H}_B$, which are real, are the poles of the R-matrix, and the values of the eigenfunctions of $\mathcal{H}_B$ on $\mathcal{S}_o$ are proportional to the corresponding residues. Lane and Robson [43] derived explicit forms of the Bloch operator for single-channel and multi-channel scattering from a spherically symmetric potential energy, proved that $\mathcal{H}_B$ is Hermitian on A, and related the operator $\mathcal{H} + \mathcal{L}_B - E$ to the scattering (S) matrix.

Since the publication of these seminal papers, R-matrix theory (in many guises) has become a mainstay of collision physics. The review by Barrett et al. [45] offers a concise summary of the many modern versions of this theory and survey its practical application, emphasizing the calculation of nuclear reaction cross sections.

A.2 R-Matrix Theory in Atomic and Molecular Physics

R-matrix theory migrated to atomic and molecular physics in 1971 with its formulation by Burke et al. [46] for electron-atom scattering and its application by Burke and Robb [48] to low-energy scattering of electrons from hydrogen and helium atoms. Low-energy electron collisions pose special theoretical and practical challenges due to the importance of many-body effects (electron exchange and correlation) in the near-target region. The structure and approach of R-matrix theory are ideally suited to these challenges. In short order, Burke and collaborators brought their variant of conventional R-matrix theory, in which the internal region is spanned by eigenfunctions of the sum of the Bloch operator and a *model* Hamiltonian (see the review by Burke and Robb [48]) to a high level of sophistication (O'Malley et al. 1978 [50]), a line of research that continues to the present day [see, for example, Burke and Berrington [49], Trail et. al[51], and Zhou et.el [52] and references therein].

R-matrix theory made further inroads into atomic and molecular collision physics

with its generalization in 1975 by Sceneider [53] to electron-molecule collisions. The increased complexity of molecular as opposed to atomic targets exacerbate the difficulties posed by the internal-region in electron-atom scattering. But early applications of conventional R-matrix theory to electron-molecule systems (Burke et al. [47]; Morrison and Schneider [54]; Schneider and Hay [55]) showed that one could surmount many of these difficulties by adapting sophisticated, powerful, and exhaustively developed formulations (and the corresponding computer codes) of quantum chemistry to the solution of the many-body problem in the internal region. This capability, in tandem with the facility with which R-matrix theory treats resonances, has made the R-matrix method one of the dominant techniques for modern electron-molecule scattering studies (see, for example, Mazevet et. al [56, 57], Nesbet et. al [58] and references there in). [For a succinct summary of the theory, see the review by Lane [59]; for implementation techniques, see articles by Gillian et al. [60], Morgan [61] and Schneider[62]in the collection edited by Huo . A survey of the application of R-matrix theory in atomic and molecular physics along with reprints of many of the major papers appears in the book edited by Burke and Berrington [49].]

A.3 R-Matrix Theory in Device Physics

By formally demarcating regions of space in which interactions or other physical features of a system differ, R-matrix theory offers conceptual advantages over many more familiar formulations of collision physics. Moreover, because *the most computationally demanding parts of an R-matrix calculation do not depend on the scattering energy (and must, therefore, be performed only once)*, the R-matrix method offers significant practical advantages over many alternative theories. In light of these advantages, it is somewhat surprising that R-matrix theory has not been used more widely in device physics.

Adapting R-matrix theory to quantum devices poses three major challenges. First,

spherical coordinates, which are used in nearly all other applications of this theory, are unsuited to such devices, whose geometry typically consists of one or more conductors connected to one another and to external contacts (which serve as electron reservoirs) by leads. One must therefore reformulate the theory using several Cartesian coordinate systems: one for the internal region (the conductor) and one for each lead. (Together, the leads comprise the external region.) Second, the R-matrix surface in a quantum device, which separates the internal and external regions consists in part of impenetrable walls; the boundary conditions for the wave function on such walls differ from those on the "imaginary" walls that comprise the rest of the surface. Third, the external region consists of leads which themselves have impenetrable walls and which support bound states.

Smrčka [6] first applied R-matrix theory to a mesoscopic device by adapting the formalism of Wigner and Eisenbud [5] to one-dimensional electron transport in periodically modulated two-dimensional systems. Wulf et al. [7] later generalized Smrčka's formulation to systems in which electrons are confined to more than one dimension. As in most applications of R-matrix theory to device physics, Wulf et al. focused on *transmission resonances*, calculating scattering quantities for classically allowed electron transport in a tunneling barrier with a lateral periodic modulation. In related research, Onac et.al [8] and Racec and Wulf [63] extended their R-matrix theory of nonlinear quantum transport to systems exposed to an external magnetic field, and illustrated their theory by calculating current-voltage characteristics for vertical magnetotransport through a quantum dot which they modeled by neglecting Coulomb interactions and assuming a parabolic confining potential.

Indicative of the potential R-matrix theory offers to the device community is the diversity of its (few) previous applications. In addition to the above, Stone and Bruus citeStone used conventional R-matrix theory to calculate the amplitude of a Coulomb-blockade resonance in their study of chaotic classical dynamics in semiconductor quantum dots. These authors used a simplified *single-level approximation* to

R-matrix theory, which is obtained by neglecting all but one propagating mode in each lead [42]. In a quite different application, Alhassid and Attias [65], Alhassid [66], and Alhassid el al. [67] applied resonant R-matrix theory to the statistical theory of conductance peaks [68] in a study of the correlator for conductance-peak amplitudes of a chaotic or weakly disordered quantum dot in the Coulomb-blockade regime.
Of all prior applications of R-matrix theory to device physics, the one that is closest in spirit to ours is the study by Bohn [21] of ballistic electron propagation in deflective periodic arrays of T-shaped devices. Bohn used the eigenchannel R-matrix theory [41, 69] to calculate scattering properties and zero-temperature nonlinear current-voltage characteristics for these systems.

A.4 Choice of Basis for Variational R-Matrix Calculations

In variational R-matrix theory, the internal-region basis $\{\phi_j(x)\}_{j=1}^{\infty}$ is required only to be complete on A. The basis functions must be linearly independent on A and regular at all impermeable walls $\mathcal{S}_w$. Apart from these requirements, the basis functions are arbitrary. To maximize the computational advantages of variational R-matrix theory, it makes sense to choose basis functions that facilitate evaluation of the elements of the overlap matrix and of the matrix representation of the Bloch Hamiltonian. It also makes sense to define the basis so as to provide a systematic prescription for increasing the (finite) number of functions in any actual calculation while minimizing the risk of (numerical) linear dependence. Nevertheless, this context leaves a great deal of flexibility in choice of basis functions.

One way to such a define the variational is to choose functions that satisfy Neumann boundary conditions on a surface $\mathcal{S}_o'$ that lies outside the R-matrix surfac $\mathcal{S}_o$; that is, on a surface that lies in the external region. The resulting basis will not, of course, be orthonormal on A; but (crucially) the basis will be complete on A, and

its constituent basis functions do not satisfy any particular boundary conditions on $\mathcal{S}_o$. As described in [the Implementation section], we use such a basis in the present application to two-dimensional devices.

Functions of this type were introduced to the theory of nuclear collisions (Nagarajan et al. [70], Tobocman and Nagarajan [71]) as a way to calculate the S matrix using independent-particle wave functions (Slater determinants) defined in the shell model of the nucleus (for a review, see Barrett et al. [45]) For a simple spherical square-well Nagarajan et al. [70] demonstrated the viability and efficiency of this approach, which they called the boundary-condition constraint method. These authors used harmonic-oscillator basis functions in which the natural oscillator frequency was used as a parameter to minimize the number of basis functions required to attain a desired level of convergence. (This method does not fall under the theoretical umbrella of variational R-matrix theory, and does not invoke the Bloch operator to ensure Hermiticity in A.) This approach was further developed by Philpott and collaborators [72, 73, 74] in applications to problems in nuclear physics. Of special interest is the study by Philpott and George [73], who develop a criterion for optimizing a basis of this type.

Appendix B

Dimensionless Units to Physical Quantities

Through out this thesis, we calculated the transmission coefficients of the solid-state devices as a function of the energy of the incoming electron. Usually in numerical calculations, we use the dimensionless quantities. We measured the length in terms of a characteristic length of the system, energy in terms of a characteristic energy of the system and so on. Also we measured the strength of the magnetic field in terms of the dimensionless quantity, $\mathcal{B} = w_{p_0}^2/l_B^2$, where w_{p_0} is a characteristic length in the system and $l_B^2 = \hbar/eB$, the magnetic length of the system. We need to transform these dimensionless quantities back to the real units in order to calculate the physical quantities.

B.1 Lengths and Energies

We start with the two-dimensional density of electrons. We consider the system in the reciprocal space [18]. There is a total of N electrons in the system. At zero temperature, all the states are filled up to a Fermi energy. Mathematically we write

this as,

$$2 \cdot \frac{\pi k_F^2}{(2\pi/L)^2} = N, \tag{B.1}$$

where k_F is the wave vector of a free electron at the Fermi energy,

$$E_F = \hbar^2 k_F^2 / 2m^*. \tag{B.2}$$

Equation (B.1) gives the two-dimensional density of electrons as,

$$n = \frac{k_F^2}{2\pi}. \tag{B.3}$$

Combining the equations (B.2) and (B.3), we get,

$$E_F = \frac{\pi\hbar^2}{m^*} n. \tag{B.4}$$

We can use the equation (B.4) to calculate the Fermi Energy of the system knowing the effective mass and the density of electrons. We use the experimental value for the electron density and the effective mass of the electron is a known value for different materials. We are interested in InSb for which the effective mass of the electron is a function of the energy gap between the valence band and the conduction band. However, for simplicity we use a constant effective mass, $m^* = 0.0139\, m_0$ where m_0 is the free electron mass of the electron. Taking the electron density of the system, $n = n_0 \times 10^{11}\mathrm{cm}^{-2}$, we can calculate the Fermi energy of the system as,

$$E_F = 17.2 \times n_0 \quad \text{meV}. \tag{B.5}$$

For GaAs, the effective mass of electron $m^* = 0.067 m_0$ and we get the Fermi energy as,

$$E_F = 3.57 \times n_0 \quad \text{meV}. \tag{B.6}$$

Now we need to calculate this energy in terms of the dimensionless energy units.

We measure the lengths in terms of a convenient characteristic length in the system, which in a two-dimensional system we choose as the width of the incoming lead, w_{p_0}. We shall take this unit length as,

$$w_{p_0} = \mathsf{w}_{p_0} \times 10^{-6} \quad \text{m}. \tag{B.7}$$

Now the unit of energy will be,

$$\mathcal{E}_0 = \frac{\hbar^2}{m^* w_{p_0}^2}. \tag{B.8}$$

Please note that in the chapter (5), our energy units were different and we do the relevant unit conversion in the same chapter. By substituting the values in this equation we get the energy unit as,

$$\mathcal{E}_0 = \frac{0.0055}{\mathsf{w}_{p_0}^2} \quad \text{meV}. \tag{B.9}$$

Also we choose to measure all the energies from $\mathcal{E}_0$. With that, the dimensionless energy is defined as,

$$\epsilon = \frac{E - \mathcal{E}_0}{\mathcal{E}_0}. \tag{B.10}$$

We combine the equations (B.4), (B.8) and (B.10) and get the dimensionleass Fermi energy,

$$\epsilon_F = 1000 \times \pi \, n_0 \, \mathsf{w}_{p_0}^2 - 1. \tag{B.11}$$

Note that the dimensionless Fermi energy, and hence the number of occupied channels does not depend on the effective mass of the material. However, the spacing between levels is material dependent.

We will now consider a device in which the width of the incoming lead $w_{p_0} = 0.1\mu$m that the is $\mathsf{w}_{p_0} = 0.1$ and the carrier concentration $n = 1.90 \times 10^{11}\text{cm}^{-2}$ that $n_0 = 1.9$. The dimensionless Fermi energy will be,

$$\epsilon_F = 58.69. \tag{B.12}$$

According to the equation (3.12), we can find that there are 3 open channels at this energy.

In the section (6.3 and 6.4), we have calculated the bend resistance at arbitrary values of dimensionless energies. Using the equations (B.11), we convert the dimensionless energies to the corresponding size of the device and tabulate in the table (B.1).

Fermi Energy (Dimensionless)	Width (w_A) (in nm)
8	38
11	45
15	52
25	66
35	77
40	82
59	100
60	101
75	113
85	120

Table B.1: The dimensionless Fermi energy is converted into the size of the device. In fact, the values at different points in the x axis of the transmission coefficients graphs (fig.6.5 and fig. 6.8) is converted into the relevant device size. We considered a sample with a electron concentration $n = 1.90 \times 10^{11}\text{cm}^{-2}$.

B.2 Strength of the Magnetic Field

In the chapter (6), we choose to measure the strength of the magnetic fields in terms of the dimensionless quantity $\mathcal{B} = w_{p_0}^2/l_B^2$. Here we explain how to transform these energies into the real units. Our dimensionless unit is related to the ratio between the magnetic length of the system and the width of the incoming lead.

We will first calculate the magnetic length l_B of the system. Let us consider an applied magnetic field $B = B_0$ tesla and the magnetic length,

$$\begin{aligned} l_B^2 &= \frac{\hbar}{eB} \\ l_B &= \frac{2.56 \times 10^{-8}}{\sqrt{B_0}} \quad \text{m.} \end{aligned}$$

The magnetic length cannot be defined for $B = 0$ case. Now we will consider a device in which the lengths are measured in terms of $w_{p_0} = \mathsf{w}_{p_0} \times 10^{-6}\text{m}$,

$$\begin{aligned} \mathcal{B} &= \frac{w_{p_0}^2}{l_B^2} \\ &= \frac{\mathsf{w}_{p_0}^2 \times 10^{-12}}{B_0 \times (2.566)^2 \times 10^{-16}} \end{aligned}$$

For a sample with $\mathsf{w}_{p_0} = 0.1$, the strength of the magnetic field of 1 tesla equals to the dimensionless magnetic field strength,

$$\mathcal{B} = 15.12, \tag{B.13}$$

which says,

$$\mathcal{B} = 1 \rightarrow \frac{1}{15.12}\text{Tesla}. \tag{B.14}$$

We use the equation (B.14) to convert the dimensionless energy units into the real magnetic field strengths in the sections (6.3 and 6.4).

Appendix C

Bloch Eigenfunctions in a Wedge Geometry

In the chapters (4) and (6), we used the Bloch eigenfunctions of a wedge geometry. In this appendix, we explain how to find these Bloch eigenfunctions in a wedge geom-

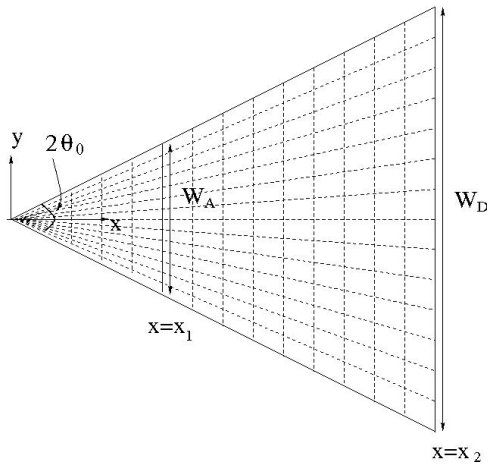

Figure C.1: A schematic diagram of a wedge geometry. In this appendix, we discuss how to calculate the Bloch eigenfunctions in the wedge geometry which is used in the chapters (4) and (6). The mesh in the figure shows a new coordinate system $(x, t = y/x)$. In the text we explain how to use both the (x, y) and (x, t) coordinate systems to calculate the Bloch eigenfunctions in this geometry.

etry (fig.C.1). One could write the Bloch Hamiltonian in the discretized real space with the physical boundary conditions and diagonalize the Hamiltonian to find the eigenfunctions and the eigenenergies. However, this is not computationally efficient. We would prefer to do most of the overlap integrals analytically. First we have to write the Bloch operator and find a set of basis functions that satisfy the physical hard wall boundary conditions. We will think about two sets of coordinates (x, y) and (x, t) as shown in the figure (C.1). There are two important points to make:

- The physical hard wall boundary conditions are easy to write in the $(x, t = \frac{y}{x})$ coordinates,

and,

- The Hamiltonian operator is easy to calculate in the (x, y) coordinates since Bloch term is always pointing outwards to the soft boundaries.

Because of that we choose to use a set of basis functions in (x, t) coordinates, write the Bloch Hamiltonian in the (x, y) coordinates and do the overlap integrals in (x, t) coordinates.

The Bloch Hamiltonian takes the form,

$$\mathcal{H}_B = -\frac{1}{2}\left(\nabla_x^2 + \nabla_y^2\right) + \frac{1}{2}\left(-\delta(x - x_1)\frac{d}{dx} + \delta(x - x_2)\frac{d}{dx}\right). \tag{C.1}$$

We choose a set of variational basis functions which satisfies the physical hard wall boundary conditions. The t dependent basis functions take the form,

$$\zeta_b(t) = \sqrt{\frac{2}{\mathsf{t}_0}} \tan \frac{b\pi\,(t + \mathsf{t}_0/2)}{2\,\mathsf{t}_0}, \tag{C.2}$$

where $\mathsf{t}_0 = \tan 2\theta_0$. These basis functions are similar to the infinite well eigenfunctions which satisfy the hard wall boundary conditions.

The x dependent basis functions take the form similar to the horizontal basis functions we used in the T-junction problem. Here we repeat the form of those functions.

$$\begin{aligned} |\eta_a^x(x)\rangle &= \sqrt{\frac{1}{\lambda_x}} \\ &= \sqrt{\frac{2}{\lambda_x}} \sin \frac{a\pi}{\lambda_x} x \quad \text{for} \quad a = 1, 3, \ldots \qquad \text{(C.3)} \\ &= \sqrt{\frac{2}{\lambda_x}} \cos \frac{a\pi}{\lambda_x} x \quad \text{for} \quad a = 2, 4, \ldots, \end{aligned}$$

(C.4)

Here we used $\lambda_x = \nu(x_2 - x_1)$ where we used $\nu = 1.3$.

Since the Hamiltonian is written in the (x, y) coordinates, we have to transform the basis functions to (x, y) coordinates, and then after defining the elements of the Bloch Hamiltonian, the integrals can be done using the (x, t) coordinates. Note that (x, t) is not a set of orthogonal coordinate system so that one cannot do the integration as $\int_{-\mathsf{to}/2}^{\mathsf{to}/2} \int_{x_1}^{x_2} dx\, dt$. We will find the integration element as follows.

The infinitesimal area ds is given by,

$$ds^2 = dx^2 + dy^2, \qquad \text{(C.5)}$$

where dx is the infinitesimal length in the x direction and dy is the infinitesimal length in the y direction. We can find dy as,

$$\begin{aligned} t &= \frac{y}{x} \qquad \text{(C.6)} \\ dy &= t dx + x dt \qquad \text{(C.7)} \end{aligned}$$

So,

$$ds^2 = dx^2 + dy^2 = dx^2 \, + t^2 \, dx^2 \, + \, x^2 \, dt^2 \, + \, 2 \, x \, t \, dx \, dt, \qquad \text{(C.8)}$$

which can be written in the matrix form as,

$$ds^2 = \begin{pmatrix} dx & dt \end{pmatrix} \begin{pmatrix} 1 + t^2 & xt \\ xt & x^2 \end{pmatrix} \begin{pmatrix} dx \\ dt \end{pmatrix}. \qquad \text{(C.9)}$$

We write this equation as,

$$ds^2 = \begin{pmatrix} dx & dt \end{pmatrix} g \begin{pmatrix} dx \\ dt \end{pmatrix}. \tag{C.10}$$

where,

$$g = det \begin{bmatrix} 1+t^2 & xt \\ xt & x^2 \end{bmatrix} \tag{C.11}$$

Then we get the infinitesimal area as,

$$ds = g^{1/2}\, dx\, dt, \tag{C.12}$$

which simplifies to,

$$dx\, dy = x\, dx\, dt. \tag{C.13}$$

Using the equation (C.13), we do all the overlap integrations in the (x, t) coordinates and calculate the Bloch Hamiltonian for the wedge geometry. Once we write down the Bloch Hamiltonian in the matrix form, we solve the generalized eigenvalue problem to find the coefficients $d_{n,m,a,b}$ as we explained in the section (2.3.1). And then we calculate the $\mathcal{M}$ matrix elements according to the equation (3.30).

Appendix D

R-Matrix Connection Formula for a 4-Terminal Wedge Junction Device

In the chapter (6), we discussed the transmission coefficients of electrons in a four-terminal wedge junction device. In this appendix, we show how to set up the algebra to calculate the transmission coefficients of a 4-terminal wedge junction device. We refer to the device in the figure (4.5) use the same notation as we used for the R-matrix connection formula for a diamond-shaped device. We write the R-matrix equation relating the scattering wave functions in different regions.

Using the interior region I, we relate the scattering wave function defined in the lead 1 and interior region C as,

$$f^1_{D1,n_{D1}} = \sum_{n'_{D1}} \mathsf{M}^I_{D1,n_{D1},D1,n'_{D1}} \left\langle \chi_{D1,n'_{D1}} \left| \mathcal{L}^I_{D1} \Psi^1_{E,n_{p_0}}(x = x_{D1}) \right\rangle + \right.$$
$$\sum_{n_{A1}} \mathsf{M}^I_{D1,n_{D1},A1,n_{A1}} \left\langle \chi_{A1,n_{A1}} \left| \mathcal{L}^I_{A1} \Psi^C_{E,n_{p_0}}(x = x_{A1}) \right\rangle \right., \qquad \text{(D.1)}$$

and,

$$f^{C}_{A1,n_{A1}} = \sum_{nD1} \mathsf{M}^{I}_{A1,n_{A1},D1,n_{D1}} \left\langle \chi_{D1,n_{D1}} \left| \mathcal{L}^{I}_{D1} \Psi^{1}_{E,n_{p_0}}(x = x_{D1}) \right\rangle + \right.$$
$$\sum_{n'_{A1}} \mathsf{M}^{I}_{A1,n_{A1},A1,n'_{A1}} \left\langle \chi_{A1,n'_{A1}} \left| \mathcal{L}^{I}_{A1} \Psi^{C}_{E,n_{p_0}}(x = x_{A1}) \right\rangle \right. . \tag{D.2}$$

Using the interior region I, we relate the scattering wave function defined in the lead 2 and interior region C as,

$$f^{2}_{D2,n_{D2}} = \sum_{n'_{D2}} \mathsf{M}^{II}_{D2,n_{D2},D2,n'_{D2}} \left\langle \chi_{D2,n'_{D2}} \left| \mathcal{L}^{II}_{D2} \Psi^{2}_{E,n_0}(x = x_{D2}) \right\rangle + \right.$$
$$\sum_{n_{A2}} \mathsf{M}^{II}_{D2,n_{D2},A2,n_{A2}} \left\langle \chi_{A2,n_{A2}} \left| \mathcal{L}^{II}_{A2} \Psi^{C}_{E,n_0}(x = x_{A2}) \right\rangle \right. , \tag{D.3}$$

and,

$$f^{C}_{A2,n_{A2}} = \sum_{nD2} \mathsf{M}^{II}_{A2,n_{A2},D2,n_{D2}} \left\langle \chi_{D2,n_{D2}} \left| \mathcal{L}^{II}_{D2} \Psi^{2}_{E,n_0}(x = x_{D2}) \right\rangle + \right.$$
$$\sum_{n'_{A2}} \mathsf{M}^{II}_{A2,n_{A2},A2,n'_{A2}} \left\langle \chi_{A2,n'_{A2}} \left| \mathcal{L}^{II}_{A2} \Psi^{C}_{E,n_0}(x = x_{A2}) \right\rangle \right. . \tag{D.4}$$

Using the interior region III, we relate the scattering wave function defined in the lead 3 and interior region C as,

$$f^{3}_{D3,n_{D3}} = \sum_{n'_{D3}} \mathsf{M}^{III}_{D3,n_{D3},D3,n'_{D3}} \left\langle \chi_{D3,n'_{D3}} \left| \mathcal{L}^{III}_{D3} \Psi^{3}_{E,n_{p_0}}(x = x_{D3}) \right\rangle + \right.$$
$$\sum_{n_{A3}} \mathsf{M}^{III}_{A2,n_{A3},D3,n_{D3}} \left\langle \chi_{D3,n_{D3}} \left| \mathcal{L}^{III}_{D3} \Psi^{C}_{E,n_{p_0}}(x = x_{D3}) \right\rangle \right. , \tag{D.5}$$

and,

$$f^{C}_{A3,n_{A3}} = \sum_{nD3} \mathsf{M}^{III}_{A3,n_{A3},D3,n_{D3}} \left\langle \chi_{D3,n_{D3}} \left| \mathcal{L}^{III}_{D3} \Psi^{3}_{E,n_{p_0}}(x = x_{D3}) \right\rangle + \right.$$
$$\sum_{n'_{A3}} \mathsf{M}^{III}_{A3,n_{A3},A3,n'_{A3}} \left\langle \chi_{A3,n'_{A3}} \left| \mathcal{L}^{III}_{A3} \Psi^{C}_{E,n_{p_0}}(x = x_{A3}) \right\rangle \right. . \tag{D.6}$$

Using the interior region IV, we relate the scattering wave function defined in the lead 4 and interior region C as,

$$f^4_{D4,n_{D4}} = \sum_{n'_{D4}} \mathsf{M}^{IV}_{D4,n_{D4},D4,n'_{D4}} \left\langle \chi_{D4,n'_{D4}} \left| \mathcal{L}^{IV}_{D4} \Psi^4_{E,n_{p_0}}(x = x_{D4}) \right\rangle + \right.$$
$$\sum_{n_{A4}} \mathsf{M}^{IV}_{D4,n_{D4},A4,n_{A4}} \left\langle \chi_{A4,n_{A4}} \left| \mathcal{L}^{IV}_{A4} \Psi^C_{E,n_{p_0}}(x = x_{A4}) \right\rangle \right., \tag{D.7}$$

and,

$$f^C_{A4,n_{A4}} = \sum_{nD4} \mathsf{M}^{I}_{A4,n_{A4},D4,n_{D4}} \left\langle \chi_{D4,n_{D4}} \left| \mathcal{L}^{IV}_{D4} \Psi^4_{E,n_{p_0}}(x = x_{D4}) \right\rangle + \right.$$
$$\sum_{n'_{A4}} \mathsf{M}^{IV}_{A4,n_{A4},A4,n'_{A4}} \left\langle \chi_{A4,n'_{A4}} \left| \mathcal{L}^{IV}_{A4} \Psi^C_{E,n_{p_0}}(x = x_{A4}) \right\rangle \right. \tag{D.8}$$

Now using the interior region C, we can use 4 equations corresponding to the 4-interior regions as,

$$\begin{aligned}
f^I_{A1,n_{A1}} &= \sum_{n'_{A1}} \mathsf{M}^{C}_{A1,n_{A1},A1,n'_{A1}} \left\langle \chi_{A1,n_{A1}} \left| \mathcal{L}^{C}_{A1} \Psi^I_{E,n_{p_0}}(x = x_{A1}) \right\rangle \right. \\
&+ \sum_{n_{A2}} \mathsf{M}^{C}_{A1,n_{A1},A2,n_{A2}} \left\langle \chi_{A2,n_{A2}} \left| \mathcal{L}^{C}_{A2} \Psi^{II}_{E,n_{p_0}}(x = x_{A2}) \right\rangle \right. \\
&+ \sum_{n_{A3}} \mathsf{M}^{C}_{A1,n_{A1},A3,n_{A3}} \left\langle \chi_{A3,n_{A3}} \left| \mathcal{L}^{C}_{A3} \Psi^{III}_{E,n_{p_0}}(x = x_{A3}) \right\rangle \right. \\
&+ \sum_{n_{A4}} \mathsf{M}^{C}_{A1,n_{A1},A4,n_{A4}} \left\langle \chi_{A4,n_{A4}} \left| \mathcal{L}^{C}_{A4} \Psi^{IV}_{E,n_{p_0}}(x = x_{A4}) \right\rangle \right.,
\end{aligned} \tag{D.9}$$

$$\begin{aligned}
f^{II}_{A2,n_{A2}} &= \sum_{n_{A1}} \mathsf{M}^{C}_{A2,n_{A2},A1,n_{A1}} \left\langle \chi_{A1,n_{A1}} \left| \mathcal{L}^{C}_{A1} \Psi^I_{E,n_{p_0}}(x = x_{A1}) \right\rangle \right. \\
&+ \sum_{n'_{A2}} \mathsf{M}^{C}_{A2,n_{A2},A2,n'_{A2}} \left\langle \chi_{A2,n'_{A2}} \left| \mathcal{L}^{C}_{A2} \Psi^{II}_{E,n_{p_0}}(x = x_{A2}) \right\rangle \right. \\
&+ \sum_{n_{A3}} \mathsf{M}^{C}_{A2,n_{A2},A3,n_{A3}} \left\langle \chi_{A3,n_{A3}} \left| \mathcal{L}^{C}_{A3} \Psi^{III}_{E,n_{p_0}}(x = x_{A3}) \right\rangle \right. \\
&+ \sum_{n_{A4}} \mathsf{M}^{C}_{A2,n_{A2},A4,n_{A4}} \left\langle \chi_{A4,n_{A4}} \left| \mathcal{L}^{C}_{A4} \Psi^{IV}_{E,n_{p_0}}(x = x_{A4}) \right\rangle \right.,
\end{aligned} \tag{D.10}$$

$$
\begin{aligned}
f^{III}_{A3,n_{A3}} &= \sum_{n_{A1}} \mathsf{M}^{C}_{A3,n_{A3},A1,n_{A1}} \left\langle \chi_{A1,n_{A1}} \middle| \mathcal{L}^{C}_{A1} \Psi^{I}_{E,n_{p_0}}(x = x_{A1}) \right\rangle \\
&+ \sum_{n_{A2}} \mathsf{M}^{C}_{A3,n_{A3},A2,n_{A2}} \left\langle \chi_{A2,n_{A2}} \middle| \mathcal{L}^{C}_{A2} \Psi^{II}_{E,n_{p_0}}(x = x_{A2}) \right\rangle \\
&+ \sum_{n'_{A3}} \mathsf{M}^{C}_{A3,n_{A3},A3,n'_{A3}} \left\langle \chi_{A3,n'_{A3}} \middle| \mathcal{L}^{C}_{A3} \Psi^{III}_{E,n_{p_0}}(x = x_{A3}) \right\rangle \\
&+ \sum_{n_{A4}} \mathsf{M}^{C}_{A3,n_{A3},A4,n_{A4}} \left\langle \chi_{A4,n_{A4}} \middle| \mathcal{L}^{C}_{A4} \Psi^{IV}_{E,n_{p_0}}(x = x_{A4}) \right\rangle, \qquad \text{(D.11)}
\end{aligned}
$$

and,

$$
\begin{aligned}
f^{IV}_{A4,n_{A4}} &= \sum_{n_{A1}} \mathsf{M}^{C}_{A4,n_{A4},A1,n_{A1}} \left\langle \chi_{A1,n_{A1}} \middle| \mathcal{L}^{C}_{A1} \Psi^{I}_{E,n_{p_0}}(x = x_{A1}) \right\rangle \\
&+ \sum_{n_{A2}} \mathsf{M}^{C}_{A4,n_{A4},A2,n_{A2}} \left\langle \chi_{D2,n_{D2}} \middle| \mathcal{L}^{C}_{D2} \Psi^{II}_{E,n_{p_0}}(x = x_{D2}) \right\rangle \\
&+ \sum_{n_{A3}} \mathsf{M}^{C}_{A4,n_{A4},A3,n_{A3}} \left\langle \chi_{A3,n_{A3}} \middle| \mathcal{L}^{C}_{A3} \Psi^{III}_{E,n_{p_0}}(x = x_{A3}) \right\rangle \\
&+ \sum_{n'_{A4}} \mathsf{M}^{C}_{A4,n_{A4},A4,n'_{A4}} \left\langle \chi_{A4,n'_{A4}} \middle| \mathcal{L}^{C}_{A4} \Psi^{IV}_{E,n_{p_0}}(x = x_{A4}) \right\rangle. \qquad \text{(D.12)}
\end{aligned}
$$

The scattering wave function should satisfy 4 sets of boundary conditions, the continuity of the wave function and its derivative across each internal boundaries, A_1, A_2, A_3 and A_4. We mathematically write the boundary conditions for the continuity of the wave function as,

$$f^{I}_{A1,n_{A1}} = f^{C}_{A1,n_{A1}}, \qquad \text{(D.13)}$$

$$f^{II}_{A2,n_{A2}} = f^{C}_{A2,n_{A2}}, \qquad \text{(D.14)}$$

$$f^{III}_{A3,n_{A3}} = f^{C}_{A3,n_{A3}}, \qquad \text{(D.15)}$$

and,

$$f^{I}_{A4,n_{A4}} = f^{C}_{A4,n_{A4}}. \qquad \text{(D.16)}$$

In writing the continuity of the derivative of the scattering wave function new sets of symbols, $\mathsf{A}_{A_j,n_{Aj}}$. The boundary conditions become,

$$\left\langle \chi_{A1,n_{A1}}(y_{A1}) \middle| \mathcal{L}^{I}_{A1} \Psi^{C}_{E,n_{p_0}}(x = x_{A1}) \right\rangle = - \left\langle \chi_{A1,n_{A1}}(y_{A1}) \middle| \mathcal{L}^{C}_{A1} \Psi^{I}_{E,n_{p_0}}(x = x_{A1}) \right\rangle = \mathsf{A}_{A1,nA1}, \qquad \text{(D.17)}$$

$$\langle \chi_{A2,n_{A2}}(y_{A2}) \left| \mathcal{L}^{II}_{A2} \Psi^{C}_{E,n_{p_0}}(x = x_{A2}) \right\rangle = - \langle \chi_{A2,n_{A2}}(y_{A2}) \left| \mathcal{L}^{C}_{A2} \Psi^{II}_{E,n_{p_0}}(x = x_{A2}) \right\rangle = \mathsf{A}_{A2,nA2}, \tag{D.18}$$

$$\langle \chi_{A3,n_{A3}}(y_{A3}) \left| \mathcal{L}^{III}_{A3} \Psi^{C}_{E,n_{p_0}}(x = x_{A3}) \right\rangle = - \langle \chi_{A3,n_{A3}}(y_{A3}) \left| \mathcal{L}^{C}_{A3} \Psi^{III}_{E,n_{p_0}}(x = x_{A3}) \right\rangle = \mathsf{A}_{A3,nA3}, \tag{D.19}$$

and,

$$\langle \chi_{A4,n_{A4}}(y_{A4}) \left| \mathcal{L}^{IV}_{A4} \Psi^{C}_{E,n_{p_0}}(x = x_{A4}) \right\rangle = - \langle \chi_{A4,n_{A4}}(y_{A4}) \left| \mathcal{L}^{C}_{A4} \Psi^{IV}_{E,n_{p_0}}(x = x_{A4}) \right\rangle = \mathsf{A}_{A4,nA4}. \tag{D.20}$$

With the new notation the equations (D.1), (D.3, (D.5) and (D.7) reduce to,

$$f^{1}_{D1,n_{D1}} = \sum_{n'_{D1}} \mathsf{M}^{I}_{D1,n_{D1},A1,n'_{D1}} \left\langle \chi_{D1,n'_{D1}} \left| \mathcal{L}^{I}_{D1} \Psi^{1}_{E,n_{p_0}}(x = x_{D1}) \right\rangle \sum_{n_{A1}} \mathsf{M}^{I}_{A1,n_{A1},A1,n_{A1}}(-\mathsf{A}_{A1,n_{A1}}), \tag{D.21}$$

$$f^{2}_{D2,n_{D2}} = \sum_{n'_{D2}} \mathsf{M}^{II}_{D2,n_{D2},D2,n'_{D2}} \left\langle \chi_{D2,n'_{D2}} \left| \mathcal{L}^{II}_{D2} \Psi^{2}_{E,n_{p_0}}(x = x_{D2}) \right\rangle \sum_{n_{A2}} \mathsf{M}^{II}_{D2,n_{D2},A2,n_{A2}}(-\mathsf{A}_{A2,n_{A2}}), \tag{D.22}$$

$$f^{3}_{D3,n_{D3}} = \sum_{n'_{D3}} \mathsf{M}^{III}_{D3,n_{D3},A3,n'_{D3}} \left\langle \chi_{D3,n'_{D3}} \left| \mathcal{L}^{III}_{D3} \Psi^{3}_{E,n_{p_0}}(x = x_{D3}) \right\rangle \sum_{n_{A3}} \mathsf{M}^{III}_{D3,n_{D3},A3,n_{A3}}(-\mathsf{A}_{A3,n_{A3}}), \tag{D.23}$$

and,

$$f^{4}_{D4,n_{D4}} = \sum_{n'_{D4}} \mathsf{M}^{IV}_{D4,n_{D4},D4,n'_{D4}} \left\langle \chi_{D4,n'_{D4}} \left| \mathcal{L}^{IV}_{D4} \Psi^{4}_{E,n_{p_0}}(x = x_{D4}) \right\rangle \sum_{n_{A4}} \mathsf{M}^{IV}_{D4,n_{D4},A4,n_{A4}}(-\mathsf{A}_{A4,n_{A4}}). \tag{D.24}$$

Applying the boundary conditions to the equations (D.2) and (D.9) gives,

$$\begin{aligned} \sum_{n_{D1}} \mathsf{M}^{I}_{A1,nA1,D1,nD1} \langle \chi_{D1,n_{D1}} \left| \mathcal{L}^{I}_{D1} \Psi^{1}_{E,n_{p_0}}(x = x_{D1}) \right\rangle + \sum_{n'_{A1}} \mathsf{M}^{I}_{A1,n_{A1},A1,n'_{A1}} \mathsf{A}_{A1,n_{A1}} = \\ \sum_{n'_{A1}} \mathsf{M}^{C}_{A1,n_{A1},A1,n'_{A1}} \mathsf{A}_{A1,n_{A1}} + \sum_{n_{A2}} \mathsf{M}^{C}_{A1,n_{A1},A2,n_{A2}} \mathsf{A}_{A2,n_{A2}} + \\ \sum_{n_{A3}} \mathsf{M}^{C}_{A1,n_{A1},A3,n_{A3}} \mathsf{A}_{A3,n_{A3}} \sum_{n_{A4}} \mathsf{M}^{C}_{A1,n_{A1},A4,n_{A4}} \mathsf{A}_{A4,n_{A4}}. \end{aligned} \tag{D.25}$$

Similarly we get another three sets of equations as,

$$\sum_{n_{D2}} \mathsf{M}^{II}_{A2,nA2,D2,nD2} \langle \chi_{D2,n_{D2}} \left| \mathcal{L}^{II}_{D2} \Psi^{2}_{E,n_{p_0}}(x = x_{D2}) \right\rangle + \sum_{n'_{A2}} \mathsf{M}^{II}_{A2,n_{A2},A2,n'_{A2}} \mathsf{A}_{A2,n_{A2}} = \sum_{n'_{A3}} \mathsf{M}^{C}_{A2,n_{A2},A1,n'_{A1}} \mathsf{A}_{A1,n_{A1}} + \sum_{n'_{A2}} \mathsf{M}^{C}_{A2,n_{A2},A2,n'_{A2}} \mathsf{A}_{A2,n'_{A2}} + \sum_{n_{A3}} \mathsf{M}^{C}_{A2,n_{A2},A3,n_{A3}} \mathsf{A}_{A3,n_{A3}} \sum_{n_{A4}} \mathsf{M}^{C}_{A2,n_{A2},A4,n_{A4}} \mathsf{A}_{A4,n_{A4}}, \quad \text{(D.26)}$$

$$\sum_{n_{D3}} \mathsf{M}^{III}_{A3,nA3,D3,nD3} \langle \chi_{D3,n_{D3}} \left| \mathcal{L}^{III}_{D1} \Psi^{3}_{E,n_{p_0}}(x = x_{D3}) \right\rangle + \sum_{n'_{A3}} \mathsf{M}^{I}_{A3,n_{A3},A3,n'_{A3}} \mathsf{A}_{A3,n_{A3}} = \sum_{n_{A1}} \mathsf{M}^{C}_{A3,n_{A3},A3,n_{A3}} \mathsf{A}_{A3,n_{A3}} + \sum_{n_{A2}} \mathsf{M}^{C}_{A3,n_{A3},A2,n_{A2}} \mathsf{A}_{A2,n_{A2}} + \sum_{n'_{A3}} \mathsf{M}^{C}_{A3,n_{A3},A3,n'_{A3}} \mathsf{A}_{A3,n'_{A3}} \sum_{n_{A4}} \mathsf{M}^{C}_{A3,n_{A3},A4,n_{A4}} \mathsf{A}_{A4,n_{A4}}, \quad \text{(D.27)}$$

and,

$$\sum_{n_{D4}} \mathsf{M}^{IV}_{A4,nA4,D4,nD4} \langle \chi_{D4,n_{D4}} \left| \mathcal{L}^{IV}_{D4} \Psi^{4}_{E,n_0}(x = x_{D4}) \right\rangle + \sum_{n'_{A1}} \mathsf{M}^{I}_{A1,n_{A1},A1,n'_{A1}} \mathsf{A}_{A1,n_{A1}} = \sum_{n_{A1}} \mathsf{M}^{C}_{A4,n_{A4},A1,n_{A1}} \mathsf{A}_{A1,n_{A1}} + \sum_{n_{A2}} \mathsf{M}^{C}_{A4,n_{A4},A2,n_{A2}} \mathsf{A}_{A2,n_{A2}} + \sum_{n_{A3}} \mathsf{M}^{C}_{A4,n_{A4},A3,n_{A3}} \mathsf{A}_{A3,n_{A3}} \sum_{n'_{A4}} \mathsf{M}^{C}_{A4,n_{A4},A4,n'_{A4}} \mathsf{A}_{A4,n'_{A4}}. \quad \text{(D.28)}$$

Now we have 8 sets of equations, (D.21, D.22, D.23, D.24, D.25, D.26, D.27, D.28). These equations can be further reduced using the equation (3.27). Now we have 8 sets equations which can be solved for 8 sets of unknowns, $\tau^{p,p_0}_{n_{p_0},n_0}$ and $\mathsf{A}_{Aj,n_{Aj}}$

Bibliography

[1] K. v. Klirzing, G. Dorda and M. Pepper, *Phys. Rev. Lett.*, **45**, 494 (1980).

[2] T. Uzuki, M. Saito, M. Takatsu, R. A. Kiehl, and N. Yokoyama, *Phys. Rev. B.*, **52**, 8244 (1995).

[3] Supriyo Datta, *Superlattices and microsturctures.*, **28**, 253 (2000).

[4] S. Sanvito, C.J. Lambert, J. H. Jefferson, A. M. Bratkovsky, *Phys. Rev. B*, **59**, 11936 (1999).

[5] E. P. Wigner and I. Eisenbud, *Phy. Rev.*, **72**, 29 (1947).

[6] L.Smrčka, *Superlattices and microsturctures.*, **8**, 221 (1990).

[7] U. Wulf, J. Kucera, P. N. Racec, and E. Sigmund., *Phys. Rev. B.*, **58**, 16209 (1998).

[8] E. Onac, J. Kučera, and U. Wulf., *Phys. Rev. B*, **63**, 085319 (2001).

[9] T. Jayasekera, M. A. Morrison, K. Mullen, to be published.

[10] Niti Goel, S. J. Chung, M. B. Santos, K. Suzuki, S. Miyashita, Y. Hirayama, *Physica E.*, **21**, 761, (2004).

[11] N. Goel, Ph.D. Thesis, University of Oklahoma, (2004).

[12] R.Landauer *IBM J. Res. Develop*, A. Douglas Stone, A. Szafer, *IBM. J. Res. Develop.*, **32**, 384 (1988).

[13] M.Butikker, *Phy. Rev. Lett.*, **57**, 1761 (1986).

[14] Y. Imry, Introduction to Mesoscopic Physics, *Oxford University Press* (2002).

[15] J. H. Davies, The Physics of Low-Dimensional Semiconductors, *Cambridge University Press* (1997).

[16] A. Jeffery, R. E. Elmquist, J. Q. Shields, L. H. Lee, M. E. Cage, S. H. Shields and R. F. Dziuba, *Metrologia.*, **35**, 73 (1998).

[17] Supriyo Datta, *Electronic Transport Properties in Mesoscopic Systems*, Cambridge Unversity Press (1995).

[18] N. W. Ashcroft and N. D. Mermin, Solid State Physics, *W. B. Saunders Co.* (1976).

[19] C. W. J. Beenakker, H. van Houten, *Solid State Physics*, **44** 1 (1991).

[20] C. Bloch, *Nucl. Phys*, **4**, 503, (1957).

[21] John L. Bohn, *Phy. Rev. B.*, **56**, 4132 (1997).

[22] K. C. Kulander, J. C. Light, *J. Chem. Phys.*, **73**, 4337 (1980).

[23] P. E. Richmond, *Phys. Educ*, **1**, 145 (1966).

[24] L. G. C. Rego, and G. Kirczenow, *Appl. Phys. Lett.*, **75**, 2262 (1999).

[25] Junren Shi and X. C. Xie, *Phys. Rev. Lett.*, **88**, 086401 (2002).

[26] K. Burnett, M. Edwards, *J. Res. Natl. Inst. Stand. Tech.*, **101**, 4 (1996).

[27] R. Hilsch, *The Rev. of Sci. Instr.*, **18**, 108 (1947).

[28] J. J. Van Deemter, *Appl. Sci. Res.*, **1**, 174 (1952).

[29] Y. Hirayama, T. Saku, S. Tarucha, Y. Horikoshi, *Appl. Phys. Lett*, **58**, 2672 (1991).

[30] S. Tarucha, T. Saku, Y. Hirayama, and Y. Horikoshi, *Phys. Rev. B*, **45**, 13465 (1992).

[31] C. H. Yang, M. J. Yang, K. A. Cheng and J. C. Culbertson, *Phys. Rev. B*, **66**, 115306 (2002).

[32] C. J. B. Ford, M. Bütikker, C. M. Knoedler and J. M. Hong, *Phys. Rev. B*, **62**, 2724 (1989).

[33] H. Akera and T. Ando, *Phy. Rev. B*, **41**, 11967 (1990).

[34] F.M. Peeters, *Phy. Rev. Lett*, **61**, 589 (1987).

[35] R. L. Schult, H. W. Wyld, and D. G. Ravenhall, *Phys. Rev. B.*, **41**, 12760 (1990).

[36] T. Ando and H. Tamura, *Phys. Rev. B*, **46**, 2332 (1992).

[37] A.M. Song, **x**, 1-19, *Encyclopedia of Nanoscience and Nanotechnology, ed. H.S. Nalwa.*

[38] K.W.H. Stevens, *J. Phys. C: Solid State Physics*, **20**, 5791 (1987).

[39] K.L. Shepard, M.L. Roukes, B.P. Van der Gaag, *Phys. Rev. B*, **46**, 9648 (1992).

[40] Claude Cohen-Tannoudji, Bernard Diu and Franck Laloë, Quantum Mechanics, John Wiley and Sons. (1977).

[41] E.P. Wigner, Resonanaces reactions and anomalous scattering, *Phys. Rev.*, **70**, 794, (1946).

[42] A. M. Lane and R.G. Thomas, *Rev. Mod. Phys.*, **30**, 257 (1958).

[43] A. M. Lane and D. Robson, *Phys. Rev*, **151**, 774 (1966).

[44] A. M. Lane and D. Robson, *Phys. Rev*, **178**, 1715 (1969).

[45] R. F. Barrett, B. A. Robson and W. Tobocman, *Rev. Mod. Phys.*, **55**, 156 (1983).

[46] P. G. Burke, A. Hibbert, and W. D. Robb., *J. Phys*, **4**, 153 (1971).

[47] P. G. Burke, I. Mackey, and I. Shimamura, *J. Phys. B*, **10**, 2497 (1977).

[48] P. Burke and W. D. Robb, *Adv. At. Mol. Phys.*, **11**, 114 (1975).

[49] P. G. Burke and K. A. Berrington, *IOP*, London (1993).

[50] T. F. O'Malley, P. G. Burke, and K. A. Berrington., *J. Phys. B*, **12**, 953 (1979).

[51] W. K. Trail, M. A. Morrison, H.L.Zhou, B. L.Whitten, K. Bartschat, K. B. Macadam, T. L. Goforth and D. W. Norcross, *Phys. Rev. A*, **49**, 3620 (1994).

[52] H. L. Zhou, B. L. Whitten, W. K. Trail, M. A. Morrison, K. B. Macadam, K. Barschat, and D. W. Norcross, *Phys. Rev. A*, **52**, 1152 (1995).

[53] B. I. Schneider., In W.M. Huo and F. A. Gianturco, *Computational Methods for Electron-Molcule Collisions*, Chapter 8, pages 213-226, Plenum, NewYork (1995).

[54] M. A. Morrison and B. I. Schneider, *Phys. Rev. A* **16**, 1003 (1977).

[55] B. I. Schneider and P. J. Hay, *Phys. Rev. A.*, **13**, 2049 (1976).

[56] S. Mazevet, M. A. Morrison, O. Boydstun and R. K. Nesbet, *Phys. Rev. A* **59**, 477 (1999).

[57] S. Mazevet, M. A. Morrison and R. K. Nesbet, *J. Phys. B*, **31**, 4437 (1998).

[58] R. K. Nesbet, S. Mazevet, and M. A. Morrison., *Phys. Rev. A.*, **64**, 034702 (2001).

[59] N. F. Lane., *Rev. Mod. Phys.*, **52**, 29, 1980.

[60] C. J. Gillian, J. Tennyson, and P. G. Burke, In W. M. Huo and F. A. Gianturco, editors, *Computational Methods for Electron-Molecule Collisions*, chapter 10, pages 239-254, Plenum, NewYork (1995).

[61] L. A. Morgan, In W. M. Huo and F. A. Gianturco, editors, *Computational Methods for Electron-Molecule Collisions*, chapter 8, pages 239-254, Plenum, NewYork (1995).

[62] B. I. Schneider, In W. M. Huo and F. A. Gianturco, editors, *Computational Methods for Electron-Molecule Collisions*, chapter 8, pages 239-254, Plenum, NewYork (1995).

[63] E. R. Racec and U. Wulf., *Phys. Rev. B*, **64**, 115318 (2001).

[64] A. D. Stone and H. Bruus, *Physica E.*, **189**, 43 (1993).

[65] Y. Alhassid and H. Attias., *Phys. Rev. B*, **54**, 2696 (1996).

[66] Y. Alhassid, *Phys. Rev. B*, **58**, R13383 (1998).

[67] Y. Alhassid, J. N. Hormuzdiar, and N. D. Whelan., *Phys. Rev. B*, **58**, 4866 (1998).

[68] Y. Alhssid, *Rev. Mod. Phys.*, **72**, 895 (2000).

[69] M. Aymar, M. Aymar and E. Luc-Koenig., *Rev. Mod. Phys.*, **68**, 1015 (1996).

[70] M. A. Nagarajan, S. K. Shah, and W. Tobocman, *Phys. Rev.*, **14**, B63 (1965).

[71] W. Tobocman and M. A. Nagarajan, *Phys. Rev.*, **138**, B1351 (1965).

[72] R. J. Philpott, *Nucl Phys A*, **266**, 109 (2001).

[73] R. J. Philpott and J. George, *Nucl Phys A.*, **294**, 6 (1974).

[74] R. J. Philpott, D. Mukhopadhyay, and J. E. Purcell., *Nucl Phys A.*, **294**, 164 (1974).